UNIVERSITY OF CALIFORNIA,
IRVINE

Local Crystallographic Orientation Correlation Measurements Connecting the Processing and
Properties of Face-Centered Cubic Metals

DISSERTATION

submitted in partial satisfaction of the requirements
for the degree of

DOCTOR OF PHILOSOPHY

in Mechanical and Aerospace Engineering

by

David Boyd Bober

Dissertation Committee:
Timothy J. Rupert, Chair
Lorenzo Valdevit
Mukul Kumar

2017

Table of Contents

List of Figures

List of Tables

Acknowledgments

I would like to thank Timothy Rupert and Mukul Kumar for their support and guidance. In addition, Lorenzo Valdevit, James Earthman and Farghalli Mohamed have also been generous to serve on my qualifying exam or defense committees. I am grateful to Amirhossein Khalajhedayati for his contributions to the research presented in Chapter 2, specifically preparing several of the materials and transmission electron microscope samples. Likewise, I thank Jonathan Lind and Rupalee Mulay for their contributions to Chapter 3, assisting with portions of the sample preparation and analysis. Thank you also to Joe McKeown, Mark Wall, Mary LeBlanc, and the many others who offered their expert advice or assistance.

Curriculum Vitae

David Boyd Bober

2009   B.S. in Engineering, Swarthmore College
2013   M.S. in Mechanical and Aerospace Engineering, University of California, Irvine
2017   Ph.D. in Mechanical and Aerospace Engineering, University of California, Irvine

FIELD OF STUDY

Materials Science

RELATED PUBLICATIONS

Bober DB, Lind J, Mulay RP, Rupert TJ, Kumar M., "The Formation and Characterization of Large Twin Related Domains", submitted (2016)

Bober DB, Khalajhedayati A, Kumar M, Rupert TJ., "Grain boundary character distributions in nanocrystalline metals produced by different processing routes," *Metallurgical and Materials Transactions A*, (2016) 47 (3), 1389-1403.

Bober DB, Kumar M, Rupert TJ., "Nanocrystalline grain boundary engineering: Increasing Σ3 boundary fraction in pure Ni using collective deformation physics," *Acta Materialia*, (2015) 86:43.

Abstract of the Dissertation

Local Crystallographic Orientation Correlation Measurements Connecting the Processing and Properties of Face-Centered Cubic Metals

By

David Boyd Bober

Doctor of Philosophy in Mechanical and Aerospace Engineering

University of California, Irvine, 2017

Professor Timothy J. Rupert, Chair

One of the important characteristics of crystalline microstructures is how the crystal orientation changes in space, often abruptly to form grain boundaries. Quantifying crystalline microstructure can be accomplished in many ways, ranging from measurements of grain size, to long range network analyses. For example, studies of how the density of grain boundaries affects strength have led to the discovery of both the Hall-Petch relation and its breakdown in nanocrystalline metals. In another case, measurements of grain boundary character have been central to the success of grain boundary engineering in improving corrosion resistance. Where the first field focuses on the quantity of grain boundaries, the second emphasizes their qualities. This sort of analytical division can be very productive because it defines focused research problems, but it also prescribes limits around the possible findings. This thesis bridges some of these inevitable gaps by applying more expansive local orientation correlation metrics to situations where they were not, or could not, be used in the past.

Starting with the analytically simplest case, we measured the types of grain boundaries found in nanocrystalline metals prepared by different processing routines. This is of special

interest because the extreme density of grain boundaries in nanocrystalline metals exaggerates the importance of their character. Despite its importance, practical limits on microscopy previously prevented most prior research from analyzing boundary character. The development of the grain boundary character distributions have been examined to provide insight into the mechanisms responsible for their formation. Next, we use longer range metrics to unravel how the complicated topology of grain boundary engineered microstructures is formed. Studying the grain boundary network topology of these materials helps to rationalize their processing and clarify several prior studies that relied on two-point metrics. Similar grain boundary engineered materials will then be used to explore how boundary type affects grain size strengthening. The result is a new measure of how much twin boundaries contribute to yield strength, which is important to understanding the strength of advanced materials with high twin fractions. The next chapter describes a thermomechanical method for grain boundary engineering nanocrystalline metals, where conventional techniques cannot be applied. Grain boundary network measurements of these materials are then applied to understand the mechanisms at work, revealing new information about the response of nanocrystalline metals to cyclic deformation. This has value for developing new processing methods and understanding changes that may occur during service. In each section, new insights are gained by applying different local orientation correlations than have been typical in prior inquiries.

Chapter 1 – Introduction

In introducing the topic of local orientation correlations and their impact on material properties, this first chapter starts at the simplest metrics and proceeds to the more complex ones. This order parallels the progress of the field through time, especially as it has been influenced by new experimental techniques. The first section deals with grain size relationships, which are accessible with simple optical microscopes. This section has particular bearing on several later chapters, including the motivations for studying nanocrystalline materials in Chapters 2, 5 and 6. It also provides the context for chapter 4's extensive discussion of the Hall-Petch effect. Next, global orientation measurements will be discussed, an understanding of which is needed for parts of Chapters 2, 4 and 5. After introducing the tools for local orientation measurement, the remainder of this chapter explains different approaches for analyzing local orientation data. This includes aggregate grain boundary statistics, such as are employed in every subsequent chapter. It also includes longer ranger cluster measures, such as have an important role in Chapters 4 and 6.

Grain Size Relationships

The study of single-phase polycrystalline microstructure has historically relied heavily on optical metallography. With proper preparation, small variations in a polished metal's surface energy can be used to generate optical contrast and reveal microstructural features like grain boundaries (GB) and dislocation density [1]. These images are especially useful for measuring grain size, which is essentially an orientation correlation length. At length scales below the grain size, two orientation measurements will likely be similar, and at longer distances they will tend to be different [2]. The exact crystal orientations do not need to be known to measure the grain

size, only whether or not the orientation is substantially similar to or different from nearby ones. It is not a coincidence that this is precisely the kind of orientation information available from optical metallography. Indeed, the technology to actually map precise local orientations did not come about until relatively recently [3]. Grain-size based studies like the pioneering work of Hall [4] and Petch [5] emerged from this context, not to mention many other foundational works.

The Hall-Petch Effect

In the early 1950's, Hall [4] and Petch [5] independently observed a connection between grain size and the mechanical properties of metals. For Hall [4], it was the observation that the yield strength of steel increased with the inverse root of grain size. Petch [5] measured an analogous trend for fracture strength. Hall proposed that the phenomena could be described by the now-familiar inverse-square relationship that has since become known as the Hall-Petch relationship. In that work, he gave the form as:

$$\sigma_{LYP} - \sigma' \propto 1/d^{1/2} \qquad\qquad \text{Equation 1.1}$$

where, σ_{LYP} is the lower yield point and d is the grain size [4]. For the physical interpretation of σ', Hall said that, "σ' is the yield stress for a single crystal," [4] and said further that its value agreed with the single crystal experiments of Holden and Hollomon [6]. From that context, he would have meant the polyslip behavior. In subsequent years, observations of Hall-Petch type behavior have been extended from iron to a range of pure metals and alloys. The nomenclature has changed slightly to reflect this, with the equation now more typically given in the equivalent form,

$$\sigma_y = \sigma' + kd^{-1/2} , \qquad\qquad \text{Equation 1.2}$$

2

where σ_y is no longer restricted to a lower yield point, often being interpreted more generally as flow strength [7]. The proportionality constant is usually explicitly included and interpreted as the relative strength contribution of the grain boundaries, taking on material dependent values [8].

Hall-Petch Mechanisms

Probably the most commonly cited physical explanation for the Hall-Petch effect is the original idea proposed by Hall, who said,

> It is known that if a dislocation in a matrix approaches a region, such as a grain-boundary film, which has a higher yield stress than the matrix itself, then this region constitutes an effective potential barrier for the passage of the dislocation. In other words, the dislocation will experience a repulsion near the grain boundary interface, and dislocations will pile up along the glide plane behind the grain boundary film, until the stress concentrations around the tip of the slip band cause the film to yield. [4]

The core of this idea is that grain boundaries hinder dislocations, which accumulate and cause stress concentrations. It has subsequently been learned that the hard grain boundary films imagined by Hall do not exist outside very special circumstances [9, 10]. Instead, the modern version of Hall's theory holds that the grain boundaries themselves resist dislocation transmission. This resistance is thought to be proportional to the misalignment between the meeting slip systems and the magnitude of the burger's vector of the residual grain boundary dislocation that is created by transmission [11, 12]. The idea that the dislocations would be arranged in a planar pile-up allowed Hall [4] to introduced the inverse-root scaling by applying the work of Eshelby, Frank and Nabarro [13], who had two years prior published the equilibrium stress field and dislocation positions of this configuration.

The reliance on a planar dislocation pile-up arrangement has led to criticism of this theory. Li and Chou [14] have noted that the length of these pile-ups has not been correlated

3

with grain size, nor are they likely to form in materials where cross-slip to other planes is relatively easy. Instead, Li and Chou [14] proposed a different explanation in which grain boundaries serve as nucleation sites for dislocations. The idea is that a greater grain boundary area will provide more dislocation sources and lead to a higher dislocation content at a given strain. Since strength is known to depend on the square root of dislocation density [15], the familiar Hall-Petch scaling holds.

Another alternate explanation of the Hall-Petch effect has been offered by Ashby [16], who proposed that strain gradients imposed by compatibility requirements between grains increase the dislocation density. These strain gradients become larger as grain size decreases, and so does the number of geometrically necessary dislocation needed to support them [16]. This link between grain size and dislocation density leads back to the usual Hall-Petch scaling relation [16]. Interestingly, grain boundary structure is unimportant in this model. Instead, slip incompatibility is central. More details on each model, other competing ones, and the related constants for a range of materials can be found in a recent review by Cordero [8].

Hall-Petch Breakdown and Nanocrystalline Deformation

The same conceptual thread, woven from grain size and strength measurements, can be traced directly to the current interest in nanocrystalline materials [17]. While the transmission electron microscope has replaced the optical one, the focus remains on finding grain size and strength correlations [18, 19]. The novelty in nanocrystalline metals is that the traditional Hall-Petch scaling and mechanisms no longer apply [20]. As grain size is reduced below about 100 nm, the inverse-root relationship fails, with increased grain refinement leading to smaller increases in strength [20]. In fact, predictions from molecular dynamics simulations indicate the trend even reverses for grain sizes below ~10 nm, with smaller grains actually producing softer

materials [21]. This so-called inverse Hall-Petch effect has also been observed experimentally [20, 22-25]. The reasons for the transition are a changing balance between competing deformation mechanisms [18]. When conventional grain size metals are deformed at room temperature strain is carried exclusively by dislocations. Under these circumstances, grain boundaries influence deformation but they are not carriers of it. At the nanoscale, grain boundaries can mediate deformation more directly by sliding and shear coupled migration or serving as dislocation sources and sinks [21, 26] [27]. There is strong evidence that applied shear stresses can drive rapid, diffusionless motion of nanocrystalline grain boundaries via shear-coupling [28, 29]. Grain boundary sliding can also permit grains to slide past their neighbors, with accommodation provided by atomic shuffling [27]. It has even been proposed that this leads to large grain rotations [30]. At the same time, typical dislocation based mechanisms become difficult to operate. Below about 100 nm, there simply is not the space inside grains to activate conventional sources, form pile-ups or dislocation tangles [19]. This has the remarkable consequence that dislocation storage does not occur [31]. Instead, dislocations are likely to be emitted from the boundaries, cross the grain and be absorbed at the opposite side, without ever encountering another dislocation [26].

Crystallographic Texture

While optical metallography is well suited to spatial correlations like grain size, it cannot measure crystal orientation. The reverse of this trade-off is traditional x-ray crystallography, which can measure crystal orientation, but with little spatial information. The relative volumes of each orientation present in a sample can be determined based on the intensity of the diffracted x-ray signal. The result is the so-called orientation distribution function (ODF), which is often represented by pole figures. These diagrams show the projection of a sphere, marking its

intersection with each lattice plane normal of a given type. They can be used to track the evolution of a material during processing, with especially fruitful results for understanding deformation and recrystallization [32].

Another motivation for collecting these ODFs is to help connect polycrystalline deformation to the better understood single crystal case. Ideally, the plasticity principals developed for single crystals could be extended to predict the behavior of polycrystals [33]. Sach's [34] made this leap by assuming that each grain experiences the same stress. However, grains deform anisotropically and an equal stress assumption leads to strain compatibility violations, meaning voids and overlaps would form at grain boundaries. Taylor [35] took the opposite course, assuming all grains undergo the same strain, which has the corresponding problem of creating stress incompatibility at the boundaries. In doing so Taylor [35] also provided the result that 5 independent slip systems are needed to accommodate an arbitrary deformation, and that the relative stress to activate them can be captured analytically by the so-called Taylor factor. While the Sachs and Taylor models provide upper and lower bounds for the influence of crystallographic texture, a more accurate approach is to use a self-consistent method, where grains are considered to be embedded in a matrix whose properties represent the average of the polycrystalline aggregate [36]. More recently, computer code has been developed that can compute each of these models for any texture [37] . Like all ODF based analysis, the idea is to approximate a microstructure based on aggregate orientation statistics, without considering actual neighbor-neighbor interactions.

Local Orientation Measurement

The capabilities of optical metallography and X-ray diffraction began to merge with the invention of electron backscatter diffraction (EBSD), which allows crystal orientation to be

determined on a local scale [3]. Advances in both hardware and software made it possible to collect and index diffraction patterns far faster and at far better spatial resolution than before [38]. That meant the spatial correlation of orientations could be considered in ways not previously possible [39]. Where an optical micrograph might only show a boundary, local orientation information can tell what sort of boundary it is. Of course, the two orientations being compared need not cross a grain boundary. Nor is there any reason why only two orientations can be compared simultaneously. The next several pages describe the measurement and analysis of local orientation data as it will be applied in the chapters that follow. There are other methods in addition to the ones discussed, including 3D techniques [40], but they will not be applied in this thesis.

Electron Backscatter Diffraction

In electron backscatter diffraction, a specimen is loaded into a scanning electron microscope at an oblique angle to the beam, typically 70 degrees. When primary beam electrons strike this surface, some fraction of them undergo high angle elastic and inelastic scattering, emerging from the incident surface. Of those, some will have been also been scattered coherently from atomic planes near the surface. These electrons carry information about the crystal structure and orientation, creating Kikuchi diffraction patterns when they strike a two-dimensional detector [41]. Given this process, EBSD is fundamentally a surface technique, with no information available from beyond a few nanometers depth [42]. This places strict limits on the surface quality, as any residual polishing strains, oxides or contamination will adversely affect the results. In modern systems, a phosphor screen is imaged by a digital camera, which relays the diffraction pattern to a computer where the Hough transform is used to automatically determine the crystal orientation [38].

Capturing and indexing a Kikuchi pattern can now be accomplished in a few milliseconds, meaning that the electron beam can be scanned very quickly to measure millions of local orientations over areas ranging from the micrometer to the millimeter scale. Even larger mapping areas are possible with stage translation, meaning the only real limitation is chamber size. The resolution is principally limited by two factors, the electron probe size and the backscatter interaction volume. A field emission gun provides the best probe, with resolutions of ~20 nm being possible [43]. This is much larger than the probe size, <1nm, because of the volume of material penetrated by the probe that generates detectable high angle scattering [43]. This is exacerbated by the high incident angle, which enlarges both the probes projected area and the area from which backscattered electron can escape [43].

A leap forward in resolution was recently made by a change to the sample geometry and configuration. The new technique, called either transmission Kikuchi diffraction or transmission EBSD (t-EBSD), replaces the obliquely oriented sample with a thin foil placed nearly normal to the beam [44, 45]. The sample is placed very close to the final electron lens, and the Kikuchi pattern is generated by the electrons exiting the foil's lower side. This greatly limits the interaction volume and prevents the probe spreading that occurs in typical EBSD, with the result that resolution of ~2 nm is possible [45]. Otherwise, the hardware, software and analysis procedures remain identical to EBSD. The chief challenge is to prepare foils with the optimal thickness, typically below 100 nm [42].

Grain Interior Measures

Once orientation mapping has been completed, the correlations between nearby orientations can be examined. The difference in orientation is given by the rotation that transforms one orientation into the other, termed the misorientation. If the magnitude of this

misorientation is small, typically below 2-5 degrees, then the two points can be considered to lie in the same grain. After identifying all the points that belong to each grain, termed grain reconstruction, then several correlations can be applied to characterize the local orientation distribution. This can provide a semi-quantitative analysis of the local plastic deformation, which is summarized by Brewer et al. in Chapter 18 of *Electron Backscatter Diffraction in Materials Science* [43] and also Wright et al. [46]. The methods include Kernel Average Misorientation (KAM), Grain Average Misorientation (GAM), Grain Orientation Spread (GOS), and Local Average Misorientation (LAM). They are primarily distinguished by which points are selected for the misorientation calculation. In practice, GOS and GAM are well suited to giving a grain-scale representation of deformation, while KAM and LAM would be better suited to subgrain scales [43]. Likewise, estimates of the geometrically necessary dislocation (GND) content can be made [47], although the lack of out-of-plane orientation gradient information makes the correspondence to actual GND density somewhat tenuous.

Grain Boundary Description

The grain reconstruction process also provides the location of each grain boundary and the orientations on both sides. To systematically describe grain boundaries can be daunting, given that they have five degrees of freedom. Considering only their crystallography, two grains are related through a misorientation. Taking the form of an arbitrary rotation of the crystal basis, this requires three degrees of freedom to describe. One intuitive system is to use Euler vectors, with the misorientation given as a vector in one crystal basis, around which a given rotation will produce the second crystal basis. As an example, the familiar annealing twin in a face-centered cubic metal (FCC) can be described as a 60 degree rotation about the <111> crystal axis. In practice, other systems are often used, such as Euler angles, rotation matrices, or quaternions.

There is also the matter of how the two grains are geometrically connected. Assuming they meet at a plane, at least locally, then a grain boundary plane can be defined. These are typically given in the usual miller notation, bringing the total number of degrees of freedom up to 5. This plane is at least as important as the misorientation. For example, the highly ordered and low energy structure of an annealing twin would disappear if the boundary plane were nearly anything other than a {111} plane; even the symmetric {112} boundary plane has an energy more than 10 times higher [48].

To take a set of grain boundary data and draw inferences from the full 5 degree of freedom description is no easy task, and so simplifying frameworks have been developed. The coincident site lattice (CSL) system provides a way to describe any grain boundary by a single number, although there is a severe cost in information content [49]. The CSL system is based on the idea that at a given misorientation, two superimposed crystal lattices will have periodically overlapping sites, which form the basis of the CSL unit cell. The CSL number is calculated by dividing the volume of the CSL unit cell by that of the real crystal unit cell. The smaller the CSL number, the more coincident sites the superimposed lattices share. This value is denoted by Σ and called the CSL number. For example, the FCC annealing twin is a $\Sigma 3$. Low angle boundaries are given the CSL number of $\Sigma 1$.

Experimentally, some tolerance must be used to decide which CSL number best describes a boundary. One common criterion is that given by Brandon [50], which has the form,

$$\alpha = 15/\sqrt{\Sigma}$$

where α is the threshold misorientation angle given in degrees. This tolerance is applied to the misorientation angle between the ideal CSL configuration and the actual grain boundary, forming a sort of double-misorientation. To arrive at the correct result, all of the symmetrically

10

equivalent representations must be considered. The Brandon criterion has the effect of tightening the tolerance angle as the CSL number increases. Other, more restrictive criteria have also been suggested [51] and can be especially important in special contexts, such as then when the false identification of a twins needs to be limited [52, 53]. A critique of the CSL framework is that it neglects the actual grain boundary plane. As mentioned, this has can have a dramatic effect on boundary energy, and also mobility [54]. Of course, some version of this problem is unavoidable for measurements based on 2D EBSD data. One improvement is to check if the grain boundary trace, which is accessible in 2D, is consistent with a particular plane [55]. Still, this fundamental issue of 2D data would be hard to justify except for the practical successes that have resulted[56, 57].

The Σ3 Twin Boundary

One of the most important low CSL boundary types is the Σ3, which can have very low energy [58] and can be introduced to improve material properties [57, 59]. They commonly form during annealing treatments of low stacking fault FCC metals, especially during recrystallization. Phenomenologically, their areal density is known to increase with low stacking fault energy, low prior grain size and high prior cold work [60]. Four groups of models have been proposed for the origin of these so-called annealing twins, growth accidents [61-63], stacking fault packets [63, 64], grain encounters [65], and grain boundary dissociation [66-68]. The growth accident model focuses on how atoms are added to {111} facets of a migrating boundary. Typically, the atoms joining the growing grain would be expected to sit at the lowest possible energy sites, extending the FCC structure. However, there is also a statistical chance that they fall into slightly higher energy stacking fault sites. If a critical sized island of atoms is added in the incorrect stacking position, then a twin can be nucleated [62]. The probability of

this occurring has been given by Gleiter [62]. It has also been envisioned that stacking fault packets can accumulates at a grain boundary, and can then glide through the grain and create a twin [64]. In Mahajan et al.'s [63] version of this theory, the stacking faults are created by growth accidents on a moving {111} step. Both the growth accident and stacking fault packet model may also be applied to twins that form during atomic deposition processes like electrodeposition or physical vapor deposition. The grain encounter model postulates that twins form when growing grains of the proper misorientation impinge upon one another [65]. This model cannot explain the frequency of annealing twinning [69]. Grain boundary decomposition holds that twins form to lower the overall grain boundary energy [66-68]. An example of this would be a Σ11 boundary replaced by Σ3 and Σ33 boundaries [68]. The low energy of twins drives the process and therefore stacking fault energy is of primary importance [68]. This theory is problematic for explaining lamellar twins because a reverse pathway is not energetically favorable [70]. In the case of recrystallization, it also fails to explain the dependence of twin density on prior strain and grain size [60]. It is perhaps most applicable to the case for which it was originally proposed, which is corner twins formed during grain growth [66]. Twins may also form during deformation via special dislocation mechanisms [71], but this type of twinning will not be discussed to any significant extent.

When a twin forms, there are four possible orientations for the new crystallite. Gottstein [72] has shown that the first twin from a recrystallized nucleus is most likely to be along the primary or conjugate slip plane. The rules governing further twinning are less clear [72]. Miura et al. [73] have observed that the twinning plane tends to be parallel to the moving growth front, a selection method that also implies a growth accident formation. It has also been established that multiple twinning tends to terminate when the boundary plane is of 30°-40° <111> character

[72, 74]. Gottstein [72] argues that this is because this plane is very mobile, and can grow rapidly without further twinning. Berger et al. [75] explains the preference for this plane as being the consequence of its low energy. These selection criteria of are of particular interest to the recrystallization community because it is believed that twinning is the only mechanism to introduce orientations substantially different than those present in the deformed matrix, see for example Gottstein [72] or Wilbrandt [76].

Grain Boundary Character Distribution

To link bulk material properties to grain boundary type requires some way of accounting for the fact that real microstructures contain huge numbers of individual boundaries connected to form a network. The grain boundary character distribution (GBCD) is an attempt to describe these grain boundary networks by applying sweeping simplifications, much like the CSL system does for individual grain boundaries [77]. In terms of complexity, it is the simplest bridge from individual boundary categorization to microstructural metric. The GBCD compares the relative frequency of various CSL type boundaries, often presented as a histogram. GBCD can be computed using either the length or number fraction of each boundary type, the choice being context dependent [78]. Typically, only a small subset of CSL boundaries are considered individually, with others lumped together under the term random high angle grain boundary (RHAGB, or sometimes HAGB.) Additionally, the grain boundary plane can be considered to construct the 5-parameter grain boundary character distribution [79]. The motivation is to highlight boundaries with 'special' properties, although exactly what that means, and which boundaries are 'special' is debated [80]. Being based on the CSL system, the GBCD is subject to the same critiques. Additionally, GBCD ignores how boundaries are actually arranged in the microstructure and does not convey any information on their connectivity [81].

Grain Boundary Network Analysis

There is a tension between simple scalar metrics like GBCD, and more complex ones that assess network connectivity. On one hand, measurements of special boundary fraction have proven very useful to designing improved materials [57], while it has also long been recognized that they miss important details [82]. As a result, several microstructural metrics have been developed; these can themselves be categorized by the number of material points whose properties they correlate [83]. Grain boundary character distribution, is the simplest of the so-called two-point correlations and has been the foundation of most grain boundary engineering studies. While more information rich than the typical GBCD, the 5-parameter GBCD is still a two point correlation and carries the same limited information about longer length scales.

The long range behavior of networks has been modeled with percolation theory, the goal of which is to statistically infer network connectivity from two-point correlations. This requires making assumptions about how the boundaries are assembled into a network. Considering randomly assembled networks, the fraction of weak boundaries necessary to provide a percolating path can be estimated for 2D and 3D networks [84, 85]. Other percolation thresholds have been calculated for more realistic topologies, including features like triple junction constraints [86, 87]. One long standing concern of this approach is the impact of microstructural correlations, which can change percolation behavior [85, 87, 88]. Alternatively, the connectivity of grain boundary networks can be assessed more directly with three-point correlations, namely triple junction distributions [85]. Triple junction distributions build on the early observation that cracks propagating along weak boundaries may be arrested by a junction with two strong boundaries [57]. By categorizing junctions based how many strong boundaries they join, an equation for the probability for crack arrest was proposed [85]. This formulation was

subsequently modified to reconsider which triple junctions cracks actually encounter [89]. Experimental results indicated that the longer range information accessed by triple junction analysis provides a better metric for property prediction than does GBCD [81].

There are also several higher order grain boundary correlations, mostly concerned with characterizing the linear and areal dimensions of microstructural clusters, usually given by a radius of gyration and cluster mass [81, 90]. In early works, these clusters were composed of grains connected by a selected boundary type [90]. Gertsman et al. [85] proposed that boundary clusters should be analyzed instead of grain clusters because boundary connectivity more directly controls the properties of interest to grain boundary engineering. Following this, Schuh et al. [81] proposed a set of metrics tailored to boundary clusters. Grain-based clusters received renewed attention with the idea that large $\Sigma 3$-based clusters exist in grain boundary engineered materials and can provides a great deal of information about the grain boundary network [91]. Gertsman and Henager [91] observed that every grain within such a cluster is related by a $\Sigma 3^n$ relationship. They also noted that the cluster perimeter is made up of entirely random boundaries [91]. Reed and Kumar [92] subsequently developed a theoretical framework for analyzing such clusters. Those authors also coined such clusters 'twin related domains' (TRDs) [92]. There are several appealing aspects of TRD analysis, not least of which being that a scalar measure of connectivity is immediately presented by TRD size. Experiments have also linked TRD length scale to fracture morphologies, suggesting that they can be used to understand the property improvements imparted by grain boundary engineering [93]. Cayron [52] has recently offered several new metrics for TRD structure, including several for quantifying the orientation content of TRDs. Lind et al. [53] have also recently provided 3D measurements of the TRDs in

conventional and grain boundary engineered materials. They analyzed the effects of cluster definition criteria and also differences in network topology [53].

Metric Selection

The 1987 study in which Adams et al. [2] introduced the orientation coherence function (OCF) provides an interesting case study of how the choice of grain boundary metric can influence the conclusions reached. The OCF compares the orientations at points separated by arbitrary vectors. The distribution of misorientations corresponding to subsets of the spatial vectors can then be used to quantify the microstructure. Adams et al. [2] observed that the misorientations increased sharply for vectors longer than a characteristic distance, which was of course the grain size. Those authors also saw that certain misorientations were more common at intermediate distances [2]. Analyzing those peaks in the distribution, they concluded that many were due to twinning [2]. The range of distances separating these points provides a sort of length scale for twinning. Several other minor peaks in the misorientation distribution were also observed for intermediate distances, although they were not identified. Reanalyzing Adams et al.'s data, it was found that several of these orientation correlations were $\Sigma 9$ relationships.

Consider what a different non-nearest neighbor metric, the twin related domain, might have revealed about the same data. Much like the OCF, TRDs measure the long range spatial correlation of misorientations. TRD size would have provided a twinning length scale somewhat analogous to that from the OCF. Whereas the OCF is equally concerned with any misorientation, TRDs are limited to considering the $\Sigma 3^n$ family. So, a TRD approach would have identified the $\Sigma 9$ relationships immediately, while the OCF method needs to be followed by an extensive search through CSL space to arrive at this conclusion. By the same token, a TRD approach is blind to non-$\Sigma 3^n$ correlations, which the OCF is not. This would be a detriment for

studying recrystallization twinning, where the orientation to the matrix affects twin variant selection [72]. The fact that different orientation correlation metrics can lead to very different conclusions is part of the motivation for this work.

Connections to Grain Boundary Engineering

The study of grain boundary microstructure has coevolved with the field of grain boundary engineering. The goal of grain boundary engineering is to improve the properties of materials by introducing boundaries that have favorable characteristics. To accomplish this, it is necessary to quantify the grain boundary network in a way that can be correlated with material properties. For example, Watanabe introduced GBCD specifically as a tool for GB engineering [77]. Likewise, triple junction distributions, percolation models and cluster analysis were either developed for or adapted to grain boundaries networks because of interests in grain boundary engineering [81, 85, 91, 92]. The preceding section's focus on twinning is a consequence of this strong link with grain boundary engineering. In one of the earliest examples of grain boundary engineering, Palumbo [57] observed a dramatic increase in the resistance to stress corrosion cracking resistance of a nickel alloy could be accomplished if the twin fraction was increased. This was followed by other studies that found improvements in fatigue, ductility, creep and superplasticity, among other properties [94].

These twin boundaries are usually introduced by thermomechanical processing, with a modest deformation (5-20%) followed by a heat treatment [95]. This can be iterated to produce an asymptotic rise in twin fraction [89]. Depending on the level of deformation and heat treatment temperature, the process has been categorized as strain-annealing or strain-recrystallization [96]. That said, these labels may be misnomers because the operative mechanism are still debated. Randle and co-workers have postulated an abnormal grain growth

17

mechanism[97] and the so-called 'twin regeneration' model [96], although Reed [92] showed this requires specific preexisting orientations that are difficult to reconcile with the data. Others have explained the prevalent twinning as a recrystallization process [98], either as typical annealing twins [99], or as a boundary decomposition process [100].

Conclusion

In each of the following chapters, the local orientation correlations just described will be applied to gain new information about the connections between either processing and microstructure, or microstructure and properties. In Chapter 2, some of the first ever GBCD statistics will be reported for nanocrystalline metals, along with how they are affected by processing methods. The opportunity for this work existed because the tools to make these measurements were only recently invented [44]. In Chapter 3, the recently invented conceptual framework of TRDs allowed the chance to build an improved understanding of how grain boundary engineering leads to characteristic microstructures. Chapter 4 explores how the strength of these materials can be understood in a way that is sensitive to the grain boundary network. The approach will be to integrate aggregate boundary statistics into the usual Hall-Petch equation. The last two chapters return to the grain boundary networks of nanocrystalline materials, like in Chapter 2, but now with the goal of manipulating them. In addition to employing different materials and methodologies, Chapter 5 will focus on aggregate measures, while Chapter 6 adds TRD statistics.

Chapter 2 - Grain Boundary Character Distributions in Nanocrystalline Metals Produced by Different Processing Routes

Abstract

Nanocrystalline materials are defined by their fine grain size, but details of the grain boundary character distribution should also be important. Grain boundary character distributions are reported for ball milled, sputter deposited, and electrodeposited Ni and Ni-based alloys, all with average grain sizes of ~20 nm, to study the influence of processing route. The two deposited materials had nearly identical grain boundary character distributions, both marked by a $\Sigma 3$ length percentage of 23-25%. In contrast, the ball milled material had only 3% $\Sigma 3$-type grain boundaries and a large fraction of low angle boundaries (16%), with the remainder being predominantly random high angle (73%). These grain boundary character measurements are connected to the physical events that control their respective processing routes. Consequences for material properties are also discussed with a focus on nanocrystalline corrosion. As a whole, the results presented here show that grain boundary character distribution, which has often been overlooked in nanocrystalline metals, can vary significantly and influence material properties in profound ways.

Introduction

High strength, wear resistance, and fatigue tolerance make nanocrystalline metals attractive structural materials [101]. For example, pure nanostructured Ti is being tested as a replacement for less biocompatible Ti-6Al-4V in medical implants [102]. Other current or near-term applications include more environmentally benign industrial hard coatings, [103] and alternatives to depleted uranium munitions [104]. To facilitate these advances, processing scientists have developed many techniques to synthesize nanocrystalline metals in a variety of forms and compositions. Bulk parts can be manufactured by the top-down refining of a coarse grained alloy into a nanocrystalline one by severe plastic deformation (SPD) [105]. Severely deformed powders produced by ball milling can be consolidated into bulk forms, or bulk sections may be made directly through accumulative roll bonding (ARB), equal channel angular pressing (ECAP) or high pressure torsion [106-108]. A variety of physical, chemical, and electrochemical deposition techniques can be used to produce nanocrystalline coatings and even thin sheets [109-111].

The current understanding of nanocrystalline metals has been primarily built around average grain size, *d*, driven by the past success of the Hall-Petch relation [17]. At fine grain sizes where the Hall-Petch relationship breaks down, it has been replaced by new scaling rules that again relate strength to grain size [18]. The transition from one scaling rule to another occurs at critical grain sizes where the dominant deformation mechanisms change. The first grain size threshold is 100 nm, below which dislocations nucleate at grain boundaries, sweeping through entire grains without interacting with each other and forming tangles [26]. At even smaller grain sizes, around 10 nm, grain boundary sliding and rotation supplant dislocations as carriers of plasticity, eventually leading to an inverse Hall-Petch slope [21, 26]. Similar grain

size-based relationships have been applied to other mechanical properties, like wear and fatigue resistance, and functional properties, like magnetic coercivity and permeability [112-114].

The common theme to the deformation mechanisms above is that grain boundary sites become increasingly important, yet characterization of nanostructured materials rarely focuses on the boundary itself. Expanding the characterization of nanocrystalline microstructures to include more grain boundary information may help address unanswered questions about structure-property relations and also open the door for control of such features in the future. Work on conventional, coarse-grained metals has demonstrated that grain boundary networks can control a wide range of properties, from fracture to corrosion [115, 116]. In ultrafine grained (UFG) metals, or those metals with grain size larger than 100 nm but smaller than 1000 nm, the fraction of high angle boundaries has been implicated as a possible key to enhancing ductility [117]. Such effects are expected to be exaggerated at nanoscale grain sizes, where a large fraction of atoms resides in the grain boundary region. Indeed, some of the only nanocrystalline work to explicitly consider grain boundary type has been investigations into the unexpected ductility of nanotwinned copper, which is now thought to be a consequence of those special boundaries' ability to provide both soft and hard directions for dislocation motion within a single grain [118, 119]. Barmak et al. have also shown that the choice of whether or not to consider twins as grain boundaries can strongly influence the calculation of grain boundary electron scattering coefficients in nanocrystalline copper [120].

Since different nanocrystalline processing methods are controlled by a variety of physical mechanisms, there is reason to expect that these techniques will produce materials with different grain boundary networks. As a first example, consider the grain boundaries in a ball milled material, which are formed by using very large plastic strains to refine a coarse grained material

into a nanocrystalline one [121]. When applied to FCC metals, large deformations subdivide grains though the accumulation of dislocations that form into low energy dislocation structures (LEDS) [122, 123]. Continued deformation causes the misorientation across LEDS to increase, forming low angle boundaries, and eventually high angle ones [124]. Twin fragmentation is a complimentary mechanism which has been proposed for nanoscale refinement [125], where deformation twins form within existing grains and the narrow twins are then subdivided by LEDS. Several works on ball milling [126-128] cite another theory proposed by Hellstern et al. [129], who suggested that continued deformation drives nanocrystalline grain rotation, transforming low angle boundaries into high angle ones. The extent to which these competing mechanisms may operate is sure to affect the grain boundary network.

On the other hand, materials produced by deposition methods must be understood within a different framework. For both physical vapor deposition and electrodeposition, films form as atoms bond to the growth surface. This commonality causes similar structural development, even though one process is purely physical and the other is electrochemical. As new atoms deposit, they briefly undergo surface diffusion before being confined within the bulk. In nanocrystalline growth, adatoms are restricted to small rearrangements and cluster with only their immediate neighbors. Clusters grow outward until contacting adjacent grains, with grain size determined by the relative rates of nucleation and growth. As a result, the microstructure is determined by the kinetics of growth-surface phenomena [130]. In the absence of deformation or recrystallization, grain orientation is fixed at nucleation, i.e., before a grain has formed boundaries with most of its neighbors [130]. The implication is, that for non-epitaxial growth, random nucleation orientations will produce a random (Mackenzie) distribution of boundary misorientations [131]. For real films, a {111} fiber texture often develops to minimize the

surface energy of atom clusters. In this case, the Mackenzie distribution can be modified to account for texture [132]. For columnar growth (granular-epitaxy), a misorientation distribution favoring low angle boundaries would be expected along the growth normal.

In this study, we present the grain boundary character distributions (GBCDs) of nanocrystalline Ni and Ni-based alloys produced by ball milling, sputter deposition, and electrodeposition. Our results show that these processes can produce very different boundary character distributions, with several samples of identical grain size used to highlight the structural diversity that exists independent of grain size. In addition, several process variables, such as ball milling duration, post-sputter annealing and electrodeposition reverse pulse current, are examined to help gauge the range of possible grain boundary character distributions for each method and explore what generalizations can be drawn. Grain boundary character distributions are assessed with transmission Kikuchi diffraction (TKD) and the results are connected to the structure–determining physical growth mechanisms associated with each material's processing method. The connections drawn between grain boundary character distribution and synthesis mechanism allow the results to have significance beyond the specific materials used. Along this theme, our results are used to explore previous studies on the corrosion of nanocrystalline Ni and Cu. We find that processing history, as a possible proxy variable for the grain boundary character distribution, can be a good predictor of nanocrystalline corrosion resistance.

Methods

Nanocrystalline Ni-based alloys were chosen for this study because they can be synthesized by multiple techniques. Samples were produced with ball milling, sputter deposition, and electrodeposition, all having an average grain size near ~20 nm. A constant grain size was targeted to help isolate the effect of processing on grain boundary character

23

distribution. Ball milling was performed with a SPEX 8000M high energy mill, using a hardened steel vial and balls, and a ball to powder ratio of 10:1. A process control agent of 1 weight % steric acid was added to moderate cold welding, which can otherwise cause excessive powder agglomeration. Preliminary processing experiments showed that the material approached a steady state grain size after ~4 h of milling. Subsequent samples were milled for either 4 h or 10 h. The milling operation was carried out under an Ar atmosphere to avoid O and N contamination. Magnetron sputtering was used to deposit Ni films, 260±9 nm thick, onto Si wafers. A 99.999% pure Ni target was used, which, coupled with vacuum processing, yields very pure nanocrystalline films. A power of 350 W and argon pressure of 0.5 mTorr produced a deposition rate of 1.2 Å/s. The substrates were rotated parallel to the target to maximize uniformity. Deposition occurred near room temperature to obtain the desired grain size. Pulsed electrodeposition of Ni-W was performed following the work of Detor and Schuh, which allowed a precisely tunable grain size [133]. Increasing reverse pulse current density preferentially removes tungsten from the growth surface, lowering its concentration in the final film and increasing grain size [133]. Reverse pulse currents of either 100 mA/cm^2 or 150 mA/cm^2 were used to deposit Ni-W films onto pure Cu substrates, with respective W contents of 12 at.% and 6.2 at.%.

A dual beam FEI Quanta3D scanning electron/focused ion beam (SEM/FIB) microscope was used for secondary electron imaging and to measure chemical composition using energy-dispersive X-ray spectroscopy (EDS). SEM/FIB was also used to prepare TEM specimens using the in situ lift-out method. Ball milled particles were embedded in epoxy and mechanically polished before FIB milling. Electrodeposited samples were FIB cut perpendicular to the growth direction, producing a cross section view of the microstructure. Low angle Ar ion milling

(Fischione 1010) at 2-3 kV and 5 mA was used to prepare plan view TEM foils from the sputtered samples, which were released from their silicon substrates with XeF_2 etching. All samples were briefly cleaned in a 10 W oxygen plasma prior to orientation mapping to mitigate carbon contamination (South Bay Technologies PC2000).

A long-standing impediment to more clearly understanding nanocrystalline grain boundary phenomena was the limited spatial resolution of electron backscatter diffraction (EBSD), which revolutionized the study of grain boundary networks in coarse grained alloys. Research into grain boundary populations was generally limited to grain sizes greater than 100 nm [134], although this boundary could be pushed using laborious transmission electron microscope (TEM) methods [135]. With the advent of precession electron diffraction (PED) and transmission Kikuchi diffraction (TKD), orientation mapping is now possible with ~2 nm resolution [44, 136]. Grain orientations were measured here with TKD, following Keller and Geiss [44], and Trimby [45]. The same SEM was operated at 30 kV and 11 nA, with diffraction patterns collected on an Oxford Instruments Nordlys F+ EBSD detector. The thin sample was held at a working distance of 3.5 mm and tilted 20° from horizontal, so that the upper side faced away from the EBSD detector. A 1 mm aperture was used, along with the microscopes high current analytical mode. Step sizes of 2-10 nm were used based on the grain size of the materials as individually specified in the Results and Discussion. Scan times were kept short to mitigate drift, generally around 5-10 minutes for the smallest grain sizes where it posed the largest problem. The smallest maps contained only 2,500 points, but a sufficient number of maps were collected that each specimen had a total of 64,000 to 178,000 points scanned. The total areas scanned for each material are individually specified in the discussion. In analyzing the TKD data, a minimum threshold of 2 degrees was selected for grain reconstruction. Each map was

also processed with a standard dilation method that ensured unindexed pixels at grain boundaries were assigned an orientation. In doing this, a minimum grain size of 4 pixels was imposed to mitigate incorrectly indexed pixels. Examples of both the unprocessed maps and reconstructed maps will be presented to show the effect of this methodology. TKD measurements were supplemented by bright field TEM and selected area electron diffraction, which provided an overview of grain size, morphology and texture (Phillips/FEI CM20 and CM300).

The hardness of mounted and polished ball milled particles was measured with an Agilent G200 nanoindenter. The indents were performed at a constant strain rate of 0.05 s^{-1} with a 10 s hold and a Berkovich tip. Shallow indentations (0.1 µm to 0.5 µm) were used to avoid the possibility of substrate effects, since the particles' average minor axis diameter was ~10 um. This depth range exhibited the well-known indentation size effect, with shallower indents yielding greater hardness [137]. A consistent 0.4 µm indentation depth was selected for ease of comparison, although the trends reported were also observed across the full range of depths.

Results and Discussion

To begin, we investigated the grain size of sputtered, electrodeposited and ball milled samples using bright field TEM. The ball milled sample that was milled for 10 h is discussed here. Presented in Figure 2.1(a-c), these TEM images show nanocrystalline grains of equiaxed shape and with a narrow size distribution. The average grain size appears similar across each image, which are shown at equal magnification. All three materials show strong diffraction contrast between neighboring grains. Selected area diffraction patterns were also collected, with the continuous diffraction rings in Figure 2.1(d-f) indicating a wide range of orientations are present in all samples, confirming that they each have many high angle boundaries. Together with the equiaxed grains and strong diffraction contrast, this diffraction pattern implies that the

ball milled material is not a cellular or low angle structure, as is sometimes observed in less deformed ECAP specimens [106]. In the ball milled material, weak diffraction contrast within grains is due to small misorientations caused by the extensive deformation history. The W atoms dissolved in the electrodeposited sample swells the Ni lattice, which is manifested in the smaller ring diameters in Figure 2.1(e) [133]. Overall, the TEM images and diffraction patterns show relatively similar microstructures, although a few key differences in composition and deformation history are also apparent. The similarity is reinforced by quantitative analysis of the grain size using TKD. It was found that the ball milled, electrodeposited, and sputtered samples had mean grain sizes of 23 nm, 22 nm and 20 nm, respectively. All three materials have a narrow grain size distribution, which is shown by the cumulative distribution functions in Figure 2.2.
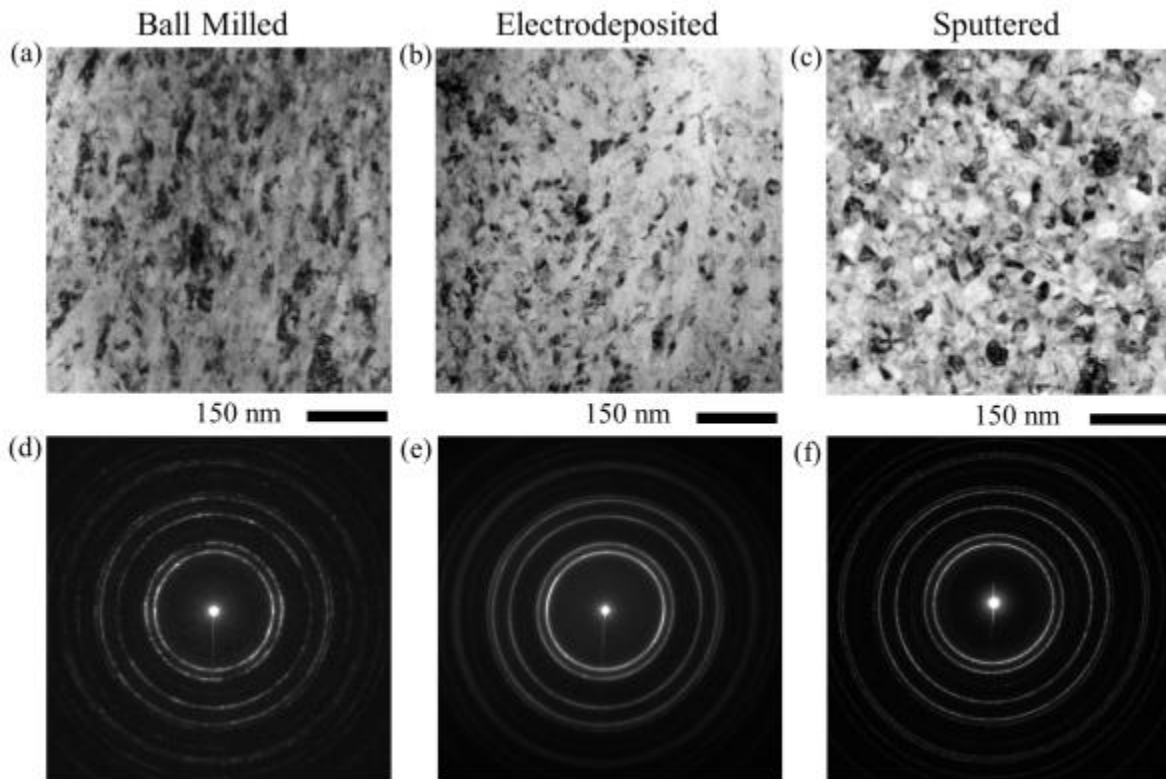
Figure 2.1: Bright field TEM images of (a) ball milled, (b) electrodeposited, and (c) sputtered Ni and Ni alloys, with accompanying selected area diffraction patterns shown

below in (d-f). Overall, the three materials have many similar characteristics, such as equiaxed grains averaging ~20nm.
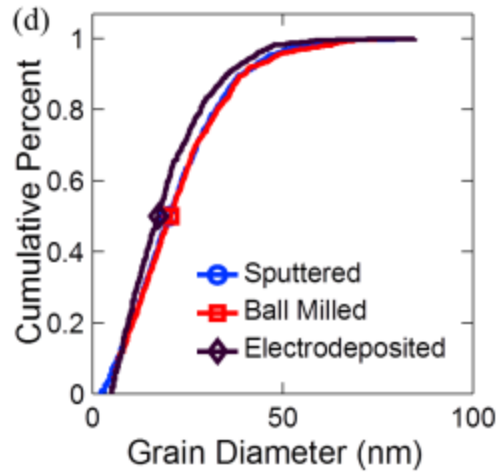
Figure 2.2: The cumulative grain size distributions for each material confirm their similar grain sizes and distributions, all having mean grain sizes in the range of 20-23 nm.

To measure how grain boundary character distribution depends on the processing technique used, orientation maps were collected with TKD. Examples of these maps for each material are shown in Figure 2.3(a-c), with no post-processing having been performed. Each map was collected with a 2 nm step size, with a total of 142,000, 64,000 and 75,000 points being scanned for the ball milled, electrodeposited and sputtered materials, respectively. The colors in Figure 2.3 (a-c) correspond to different orientations, as labeled on the inverse pole figure legend. The black areas are points that could not be indexed, typically because the probe spanned a grain boundary and two Kikuchi patterns were convolved. Coincident site lattice (CSL) theory, which groups grain boundaries according their ideal number of shared lattice sites, was used to categorize boundaries by applying the Brandon criterion [49, 50]. The low angle ($\Sigma 1$), twin ($\Sigma 3$), twin-related ($\Sigma 9$ and 27) and other low-CSL ($\Sigma 1$-29) grain boundary fractions were chosen for inclusion in the GBCD because they are the easiest to relate to processing history and material

properties. The post-processed TKD maps showing reconstructed grain boundaries are shown in Figure 2.3(d-f). The areas of these maps match those presented above in Figure 2.3(a-c). Blue lines represent low angle boundaries (2-15˚), while red is used for Σ3s and black for all others (>15°). The gray scale contrast corresponds to the Kikuchi pattern quality.
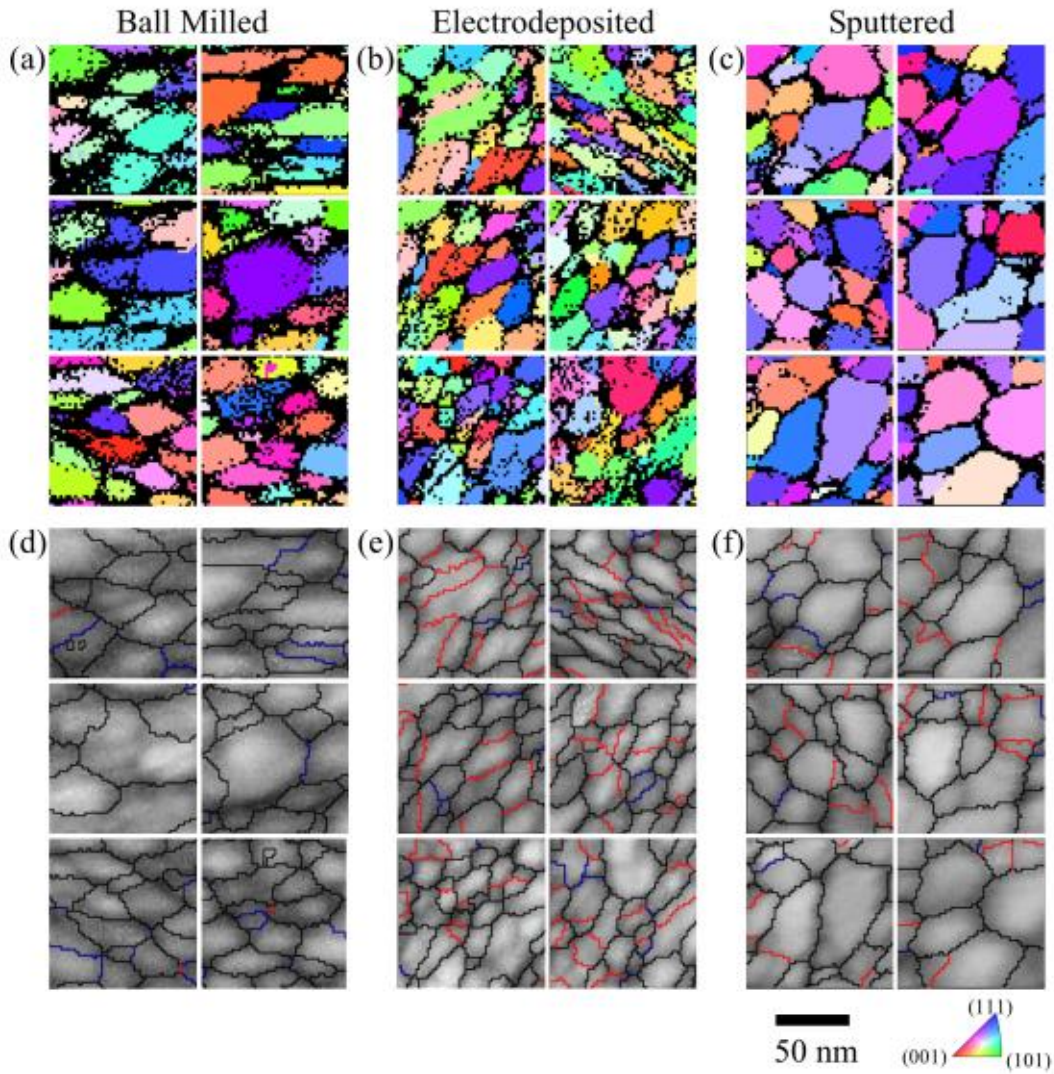
Figure 2.3: Grain orientation maps for the (a) ball milled, (b) electrodeposited, and (c) sputtered materials. Reconstructed grain boundaries are shown for the same areas in (d-f). Red lines are Σ3 boundaries, blue are Σ1s and all other boundaries are shown in black. The grey scale contrast is the Kikuchi pattern quality.

The GBCDs for each material were calculated from the boundary length fraction in the TKD maps. They are shown in Figure 2.4, whose most striking feature is how similar the sputtered and electrodeposited GBCDs are, while the ball milled GBCD is noticeably different. For example, the ball milled sample has a much larger percentage of $\Sigma 1$ boundaries (16%) than the two deposited materials (7-8%). In contrast, the two deposited samples have much higher $\Sigma 3$ percentages (24-25%), as compared to the ball milled material (3%). This $\Sigma 3$ fraction reflects twin-type boundaries of both coherent and incoherent varieties. The higher $\Sigma 9,27$ and $\Sigma 1$-29 boundary fractions in the deposited materials are a direct consequence of the high $\Sigma 3$ fraction, because $\Sigma 3$ interactions produce more $\Sigma 3^n$ boundaries and boost the overall $\Sigma 1$-29 fraction [138]. These observations can be understood by focusing on each processing route in turn.
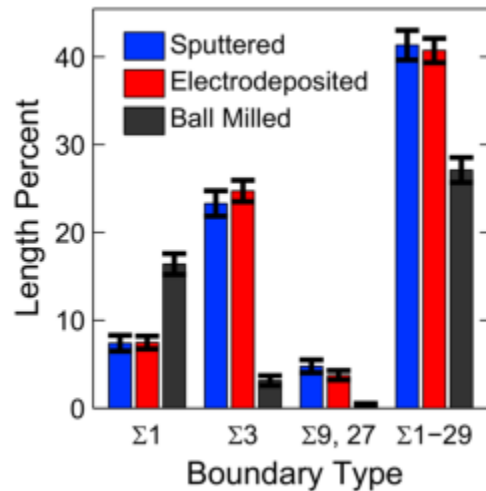
Figure 2.4: Grain boundary character distributions for sputtered, electrodeposited, and ball milled samples with a constant grain size. The length percentages of several CSL-type boundaries are shown.

Ball Milled Ni

The fraction of $\Sigma 1$ boundaries in the ball milled material is notably large compared to the materials produced by deposition. To understand this observation, it is useful to consider ultrafine grained (UFG) materials produced by ECAP and accumulative roll bonding. Like ball milling, these methods use severe plastic deformation to refine the grain size, although they

cannot achieve grain sizes (d) below about 100 nm [108, 139]. For ECAP materials, the $\Sigma 1$ percentage typically reaches a minimum plateau of 20-40% for plastic strains greater than about 6 [135, 140, 141]. A similar result has been found for accumulative roll bonded Ni, where the generation of high angle boundaries slows considerably as strains reach about 6, although no true plateau was reached in the work of Zhang et al. [108] From this perspective, the 16% $\Sigma 1$ percentage found after 10 h of ball milling is only slightly low. The fact that the $\Sigma 1$ content at d ~ 20 nm is comparable to that commonly measured at $d > 100$ nm suggests that no new mechanism for creating random high angle grain boundaries (RHAGB) becomes operative during nanocrystalline grain refinement (100 to 20 nm). This opposes the notion that grain rotation provides an added mechanism to increase RHAGB fraction during the severe plastic deformation of nanocrystalline materials [129]. Instead, it supports the continuity of grain refinement mechanisms crossing the UFG and nanocrystalline scales, as proposed by Hughes and Hansen [142]. Hughes and Hansen looked at the boundary network morphology caused by sliding contact and observed universal scaling features which suggested a continuity of subdivision mechanism until at least 10 nm. Similarly, the ball milled material's $\Sigma 3$ percentage (3%) is also in the range reported for UFG Ni produced by SPD (3-5%) [140, 141]. Consequently, the total percentage of random high angle grain boundaries (RHAGB) in the ball milled material was 73%, which is in the (upper) range observed for SPD UFG metals [135, 140, 141]. This is consistent with more qualitative selected area electron diffraction measurements in other ball milled metals, where continuous selected area diffraction rings indicate a random high angle grain boundary structure [127]. Nanocrystalline grain refinement by the LEDS mechanisms would explain why the ball milled GBCD is so similar to that observed in UFG nickel, where grain subdivision by LEDS is well established [123].

The orientation distribution can also help explain how the ball milled GBCD developed. Each dot within the stereographic projection in Figure 2.5(e) (bottom right) corresponds to the orientation of a pixel from the TKD scan. Their inhomogeneous distribution indicates that some orientations are more likely than others. Without even considering the specific texture, the presence of preferred orientations in Figure 2.5(e) already gives an indication of how the deformation proceeded. The non-random texture suggests that dislocation plasticity was more significant than grain boundary sliding or grain rotation, because the former mechanism promotes texture development while the latter two disrupt it. However, the exact balance between them is difficult to determine, although estimates for simple deformation geometries have been made using synchrotron data, forward texture modeling, and analysis of grain shape [143]. The LEDS and twin fragmentation mechanisms are both based on dislocation plasticity and are consistent with finding a preferred texture. Examining the specific texture for more insight is complicated by the nature of ball milling, and to a lesser extent, sample preparation. In Figure 2.5(e), the {110} fiber is roughly oriented along the 'y' direction, but unfortunately the FIB extraction of TEM foils from polished powder particles leaves this direction without a physical meaning. Ball milling does not have a well-defined deformation geometry, so relating a specimen axis to strain history is impossible.
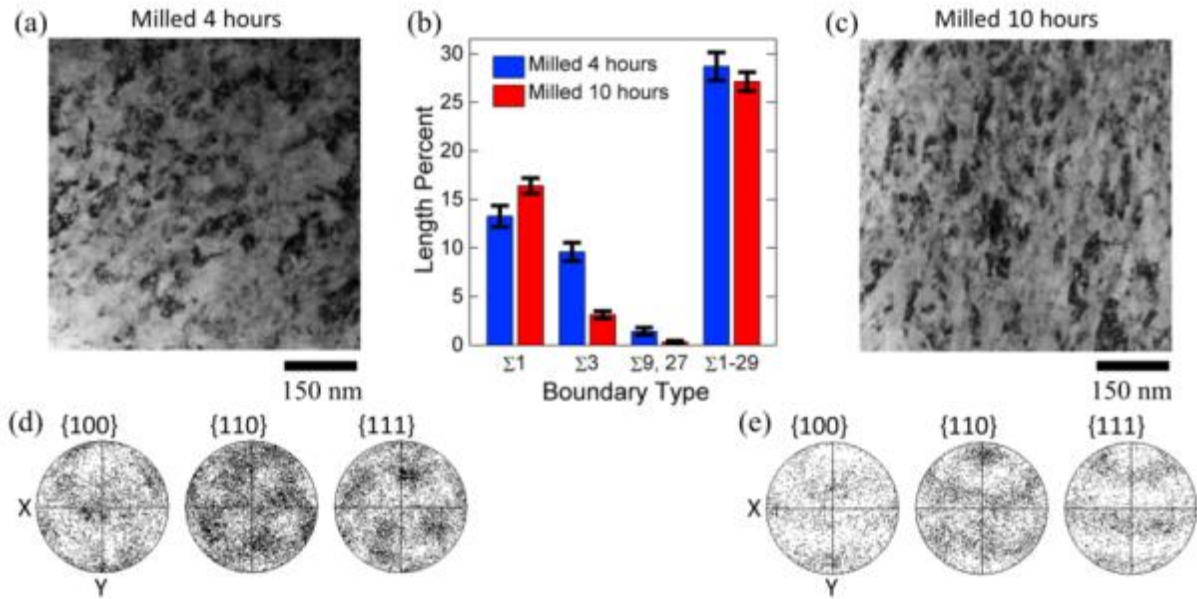
Figure 2.5: Bright field TEM images and TKD pole figures for samples ball milled for (a, d) 4 h and (c, e) 10 h, along with their GBCDs (b).

A second ball milled sample was created to provide a snapshot of the microstructure at an earlier stage of its evolution. This second sample was only milled the 4 h needed to approach the minimum grain size. Bright field TEM images after milling 4 h and 10 h look quite similar, as shown in Figure 2.5(a) and (c), respectively. Examples of the TKD maps for this material are shown in Figure 2.6(a) and (b). They were collected at a step size of 3 nm, with a total of 178,000 points scanned. TKD measurements confirmed that the mean grain size only decreased by a small amount during the additional 6 h of milling, from 27 nm at 4 h to 23 nm at 10 h. Comparing the GBCD produced at short (4 h) and long (10 h) milling times reveals several differences which are plotted in Figure 2.5(b) (top center), where the length percentages of CSL categorized boundaries are plotted. At longer milling times, the $\Sigma3$ fraction is lower than at short times. This finding is in keeping with grain refinement by dislocation subdivision or LEDS, which promotes a gradual increase in boundary misorientation and does not especially favor the development of $\Sigma3$ boundaries [124]. On the other hand, the $\Sigma1$ fraction increased slightly with

milling, which is unexpected as other SPD materials often experience a reduction in the $\Sigma 1$ fraction as dislocations accumulate to produce RHAGBs [135].

Figure 2.6: Grain orientation maps (a) and reconstructed grain boundaries (b) for the 4 h ball milled material. Red lines are $\Sigma 3$ boundaries, blue are $\Sigma 1$s and all other boundaries are shown in black. The grey scale contrast is the Kikuchi pattern quality.

The effect of milling time is also evident from the powder morphology, as shown in the SEM micrographs in Figure 2.7. These secondary electron images show the size, shape and surface texture of the individual powder particles. After 4 h of milling the particles had a platelet-like morphology (Figure 2.7(a)), while after 10 h each particle appears to be composed of many small fragments cold welded together (Figure 2.7(b)). Note that Figure 2.7(a) appears at a slightly higher magnification than Figure 2.7(b). Also observed by Xun et al. [144], this change in particle shape is thought to be due to a shift in the balance between cold welding and fracture. The new morphology implies a new deformation geometry for subsequent impact events and is probably responsible for the development of different textures after 4 h and 10 h of milling, see Figure 2.5(d) and (e). Again, it is impossible to relate the texture to a well-defined deformation axis.
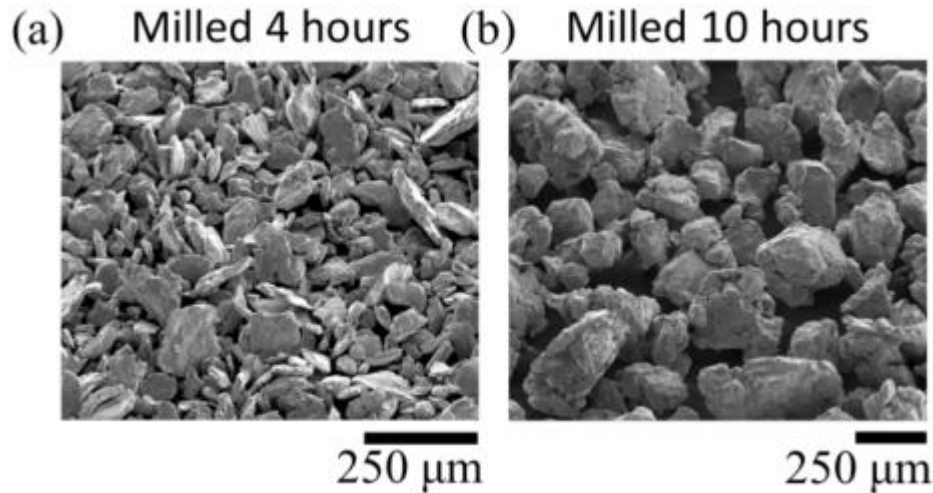
Figure 2.7: SEM images showing a change from (a) platelet shaped particles after 4 h of milling to (b) larger equiaxed particles after 10 h.

Two other notable changes that occurred with increasing milling time were an increase in Fe contamination from the hardened steel milling media and an increase in hardness. The Fe content rose from 5 at.% at 4 h to 18 at.% after 10 h milling, as measured with EDS. This type of contamination is common in ball milling, with similar high concentrations reported elsewhere [145]. Accompanying this change in composition, hardness also rose from 8.2 GPa to 9.1 GPa. Applying the solid solution strengthening model that Rupert et al. [146] have proposed for nanocrystalline metals, the change in Fe concentration would be expected to increase hardness by ~700 MPa. Grain boundary strengthening can also be expected to contribute, since the average grain size fell slightly during extended milling [4, 5]. Varied results have been reported on the relationship between hardness and grain size for nanocrystalline Ni [147-149]. Interpolation within each of these reports would predict an increase in hardness ranging from 140 to 1900 MPa, for a change from 27 to 23 nm grain size [147-149]. Summing the solid solution and grain boundary strengthening effects leads to an expected increase in hardness of 840 to 2600MPa. One possible reason why the observed hardening (900 MPa) is at the lower end of the expected range is that not all grain boundaries contribute equally to grain size strengthening; low

angle boundaries are less effective strengtheners [150]. The studies interpolated to predict grain

size strengthening [147-149] are based on deposited materials, which our GBCD results indicate

tend to have more high angle boundaries than the ball milled materials. This could lead to an

overestimate for the predicted grain size strengthening effect in the ball milled sample because

its grain boundary network has less strong obstacles to plasticity.

However, the ball milled material's RHAGB fraction is still quite high [135, 140, 141].

Based on UFG studies, this will promote ductility because RHAGB's are more susceptible to

grain boundary sliding [117, 151]. Molecular dynamics simulations indicate that this

enhancement might be even greater in nanocrystalline materials, given the increased grain

boundary area [152]. However, the high RHAGB fraction is also likely to leave the

microstructure more vulnerable to coarsening because RHAGBs are more prone to thermal

migration than are low energy boundaries. This concern has particular relevance to ball milled

powders, which must be consolidated at high temperatures if fully-dense bulk materials are

desired.

Electrodeposited Ni-W and Sputter Deposited Ni

Having tried to place the ball milled GBCD in the context of SPD and literature on

comparable materials, the same will be attempted for the two deposited materials. First, it is

instructive to recall the similarities in GBCD between the sputtered and electrodeposited

samples, which both had high $\Sigma 3$ fractions. For a different perspective on the types of grain

boundaries present, the frequency of their misorientation angles can also be plotted, as shown in

Figure 2.8. Because deposited grains should have no knowledge of their in-plane neighbors until

they coalesce, at which point their orientations are fixed, the grain boundary misorientation

distribution (correlated) should be equivalent to the misorientation distribution for any set of

randomly selected orientation pairs (uncorrelated). In contrast to this ideal case, the real correlated misorientation distribution deviates strongly from the randomly selected, uncorrelated, one around a misorientation of 60 degrees. This implies that a growth mechanism must exist that promotes this particular misorientation, which matches the $\Sigma 3$ type boundary. In fact, similar results are almost universally observed for other FCC materials that exhibit annealing or growth twins. As atoms deposit on {111} planes, some fraction occupy higher energy sites corresponding to stacking faults [153, 154]. Limited diffusion and high deposition rate can act to trap them in these locations, with subsequent layers growing the twin thickness [153, 154]. While these twins are low energy boundaries, they result from the incorporation of high energy planar defects and are intimately tied to the same non-equilibrium processes that create the nanocrystalline structure. Such an explanation accounts for both the high $\Sigma 3$ fraction and the misorientation peak at 60 degrees.
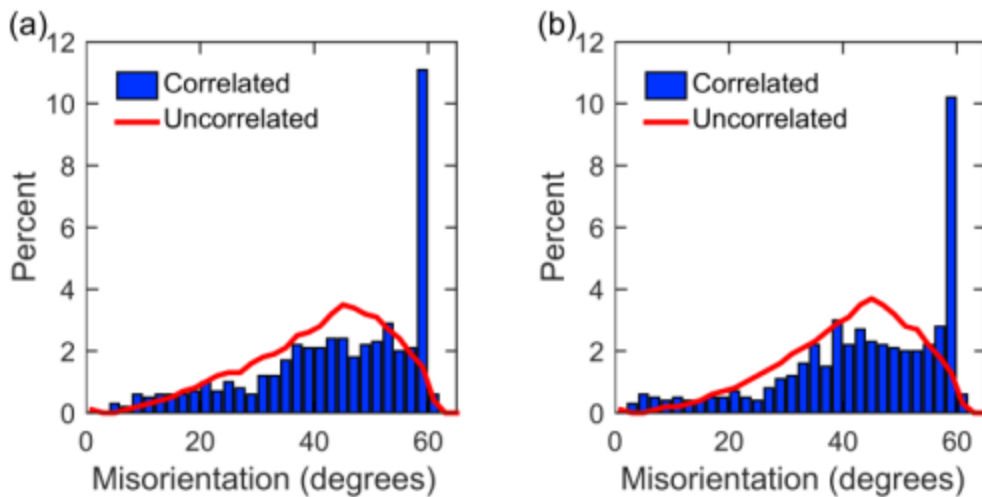
Figure 2.8: Misorientation angle distributions for (a) sputtered and (b) electrodeposited Ni, both of ~20 nm grain size. The correlated data set measures the misorientation along real boundaries, and the uncorrelated is between random grains.

The high fractions of $\Sigma 9$ and $\Sigma 27$ boundaries result from the crystallographic network constraints imposed by the many $\Sigma 3$ boundaries [138]. This stems from the triple junction

boundary combination rule, which requires the boundary misorientations meeting at a junction sum to zero. In other words, proceeding through each rotation once must result in the starting orientation. As more $\Sigma 3^n$ boundaries enter the microstructure, they are more likely to terminate at other $\Sigma 3^n$s, which requires the third boundary at the junction to also be a $\Sigma 3^n$ [138]. This analysis rationalizes the similar GBCD of the electrodeposited and sputtered films in terms of shared growth mechanisms, which might be somewhat surprising because of their different compositions. Given that W addition lowers the stacking fault energy of Ni [155], it would have been reasonable to expect more growth twins in the Ni-W. The fact that this is not the case emphasizes the importance of kinetics in driving structural development during nanocrystalline deposition [154].

The high excess energy of grain boundaries and their high volume fraction in nanocrystalline materials provides a powerful driver for grain growth. The situation is only exacerbated by the often non-equilibrium character of nanocrystalline grain boundaries, with notable examples including high energy interface planes and high grain boundary dislocation densities [106, 156, 157]. In the case of electrodeposited copper, room temperature grain coarsening has even been observed [158]. Despite being so common, it is unclear how grain growth affects nanocrystalline grain boundary character distribution. To investigate this question, a sputtered Ni sample was annealed at 524 K (250 °C) for 1 h. This temperature was selected because past experience with this material showed that annealing above about 374 K (100 °C) would cause a few grains to grow rapidly, consuming the surrounding nanocrystalline ones. Examples of the TKD maps collected for this material are shown in Figure 2.9(a) and (b). They were collected at a step size of 10 nm, with a total of 90,000 points scanned. Figure 2.10 presents TEM images and TKD data from as-deposited and annealed sputtered Ni films. Many

38

classical annealing twins are observed inside the larger grains which were not present in the original materials, as shown in Figure 2.10(a) and (c). They can be recognized as the narrow bands within grains having straight edges along {111} planes and alternating contrast. Their presence caused the annealed grain boundary network to show a much higher twin length percentage (37%) and consequently higher total special percentage, as shown in Figure 2.10(b). The overall effect is a GBCD indicative of lower energy density. These changes can be explained with conventional theories of annealing twin formation. Annealing twins are believed to form from nucleation accidents occurring on the {111} oriented steps of migrating grain boundaries, which subsequently propagate into the parent grain [62, 63]. Gleiter's model for annealing twins predicts the observed increase in twinning with increasing grain size [62]. Liu et al. [159] recently checked this model across grain sizes spanning the nanocrystalline and UFG regimes, finding good agreement. Gleiter's model also predicts significant twinning for both Cu and Ni, despite their different stacking fault energies [62]. The high number of twins may have also been enabled by the low temperature at which grain growth occurred. At these temperatures, growth accidents are less likely to be eliminated by diffusion [63]. The necessary boundary migration is still possible because of the strong driving force provided by the excess nanocrystalline grain boundary energy. This type of GBCD modification through annealing twins is also consistent with the unchanged fiber texture evident in Figure 2.10(d) and (e).
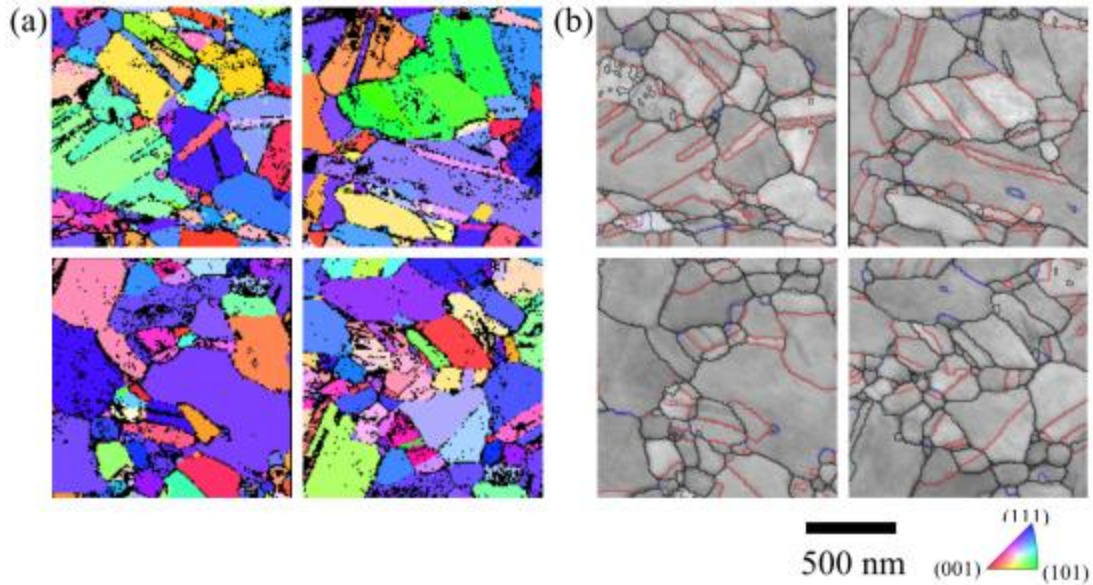
Figure 2.9: Grain orientation maps (a) and reconstructed grain boundaries (b) for the annealed sputtered material. Red lines are Σ3 boundaries, blue are Σ1s and all other boundaries are shown in black. The grey scale contrast is the Kikuchi pattern quality.
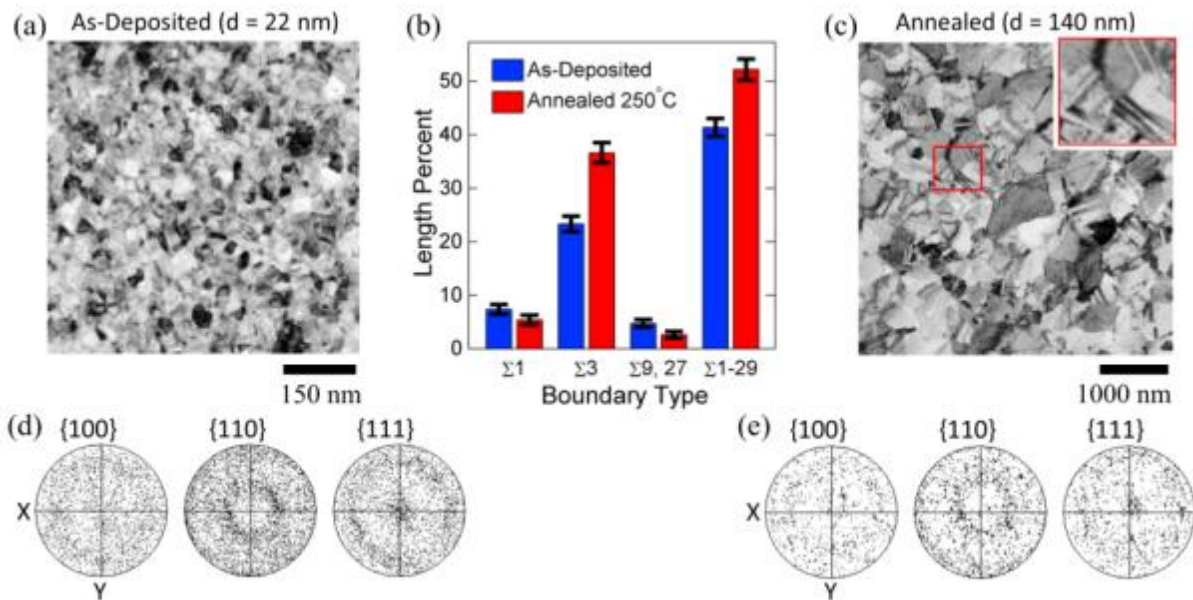
Figure 2.10: Bright field TEM images and TKD pole figures for sputtered samples having (a, d) 22 nm and (c, e) 140 nm grain sizes along with their GBCDs (b). The 140 nm grain size sample in parts (c) and (e) was annealed from the as-deposited state shown in (a) and (d). Inset in (c) shows multiple growth twins.

40

To further explore nanocrystalline deposition and the range of possible grain boundary character distribution, a second electrodeposited material was created with a larger grain size of 117 nm. Examples of the TKD maps for this material are shown in Figure 2.11(a) and (b). They were collected at a step size of 5 nm, with a total of 151,000 points scanned. The random texture remained unchanged across both samples (Figure 2.12(d) and (e)). The larger grained material contains more growth twins, as shown in the TEM images in Figure 2.12(a,c). They are again recognizable as narrow bands with alternating contrast that traverse grains. The effect of these twins is to dramatically increase the $\Sigma 3$ fraction to 51%, roughly double that of the 20 nm sample (25%), as shown in Figure 2.12(b). This change in $\Sigma 3$ fraction has a surprising dependence of W content, with more twins found at lower W content. The addition of W lowers the alloy's stacking fault energy [155], which would be expected to promote twinning. That the opposite is observed suggests that the origin of these $\Sigma 3$'s is likely to be related to the growth kinetics. The increase in $\Sigma 3$ fraction with deposited grain size is somewhat analogous to the behavior observed under annealing, although in this case the boundary between a growing and shrinking grain is replaced by the growth front. With increasing reverse pulse current, the rate of twin nucleation on the growth front remained high, even while the rate of grain nucleation dropped.
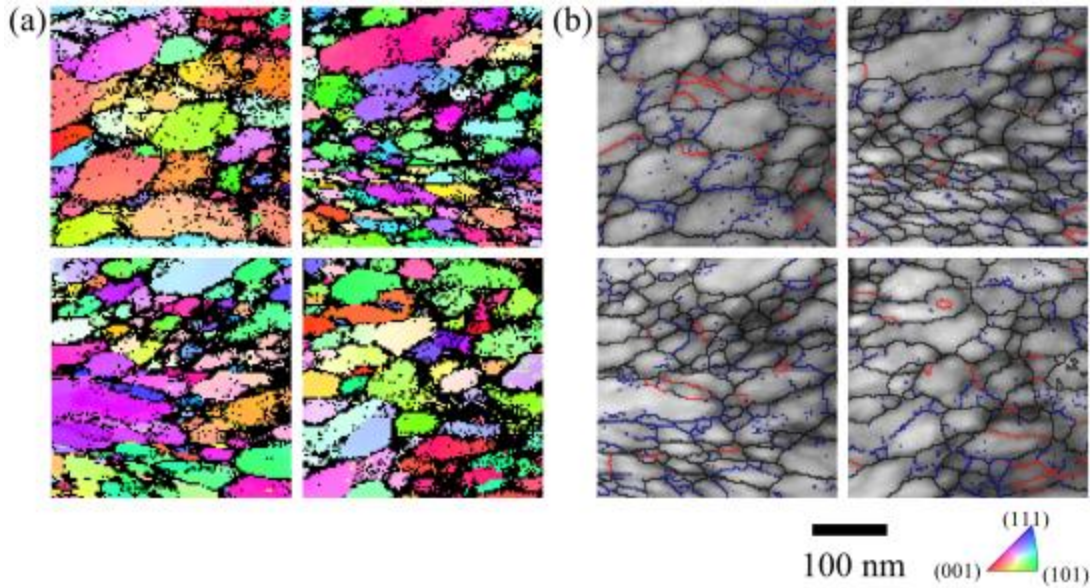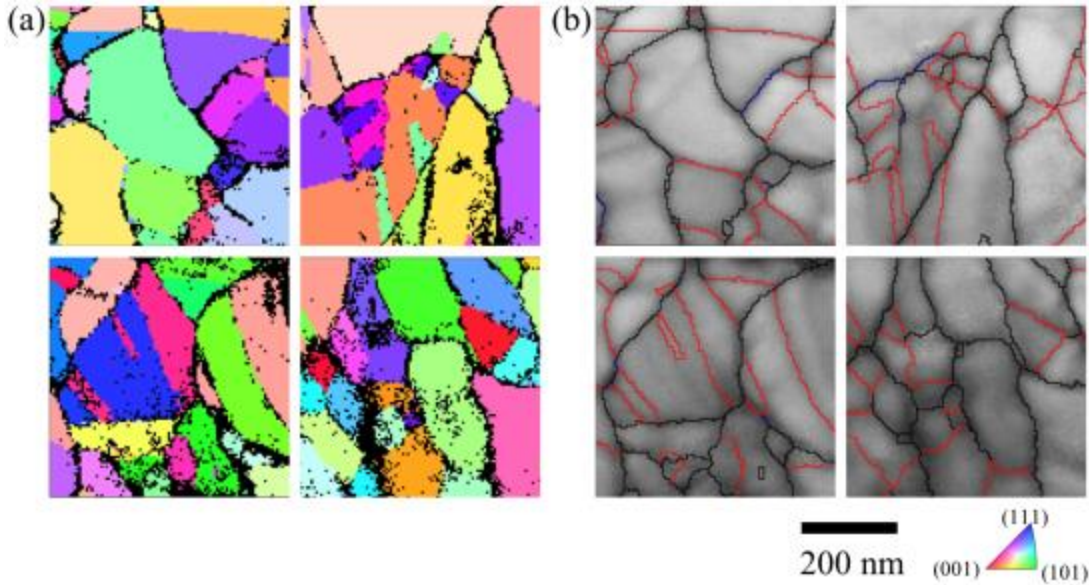
Figure 2.11: Grain orientation maps (a) and reconstructed grain boundaries (b) for the annealed sputtered material. Red lines are Σ3 boundaries, blue are Σ1s and all other boundaries are shown in black. The grey scale contrast is the Kikuchi pattern quality.
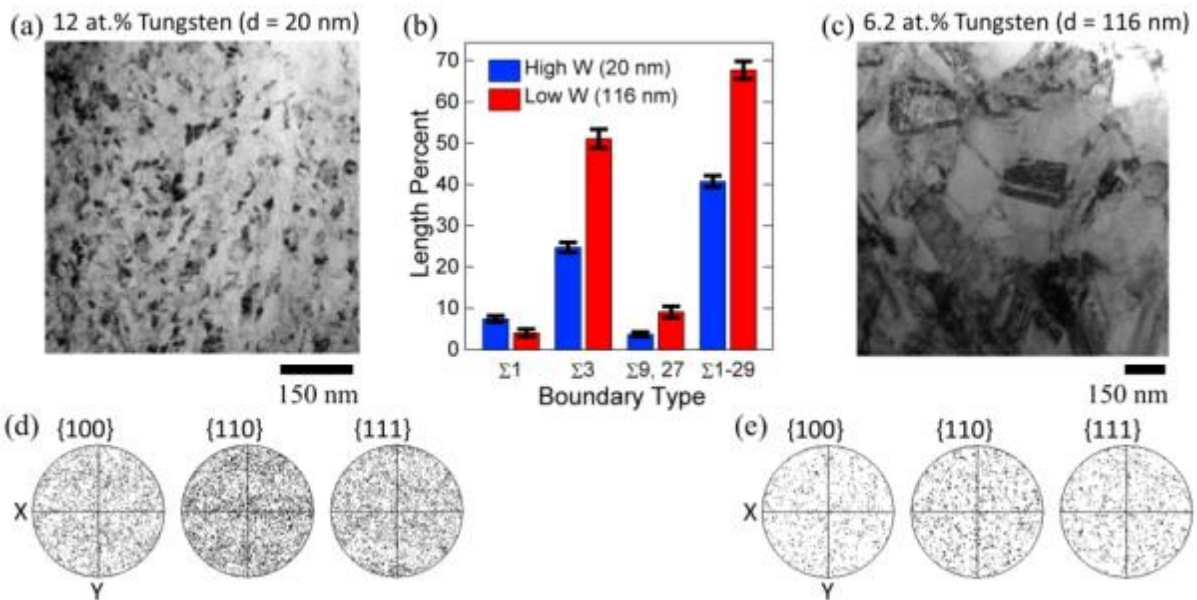
Figure 2.12: Bright field TEM images and TKD pole figures for electrodeposited samples with (a, d) 20 nm and (c, e) 115 nm grain sizes, along with their GBCDs (b). The grain size was controlled via the W content using reverse pulse plating.

GBCD and Corrosion

The high special fraction (67.7%) observed in the 117 nm grain size electrodeposited sample should have consequences for material properties. For example, a material with this special fraction is likely to inhibit intergranular corrosion [160]. This implies that the corrosion resistance of the 117 nm grain size sample is likely to surpass that of the ~20 nm grain size sample, if only GBCD is considered. Similarly, the 117 nm sample is also likely to be more corrosion resistant than coarse gained Ni, which tends to have a low special boundary fraction, unless processed in specialized ways [115]. In fact, prior literature shows just such a result; nanocrystalline Ni can exceed the corrosion resistance of coarse grained Ni [161]. Without considering boundary character, this may have seemed counterintuitive because nanocrystalline Ni has a high density of grain boundaries, which are generally more susceptible to corrosion than grain interiors [56]. This apparent anomaly led Roy et al. [134] to investigate the GBCD of nanocrystalline Ni with EBSD, where they were able to create orientation maps that captured only the larger grains present in the microstructure and saw increased twinning. From this, Roy et al. [134] concluded that a high special fraction was likely responsible for nanocrystalline Ni's corrosion resistance, a conclusion which is bolstered by the higher resolution data presented here. A similar finding was also recently reported by Zhao et al. [162] for nanotwinned copper, in which higher levels of twinning promoted corrosion resistance. In a columnar microstructure, it was found that having many twins parallel to the growth face reduced corrosion, although changes in {111} texture strength were also believed to contribute [162].

While our data supports the conclusions of Roy et al. [134], it also points to the fact that high special boundary fractions are not universal in nanocrystalline metals and therefore increased corrosion resistance should not always be expected. In fact, even among studies on nanocrystalline Ni, conflicting grain size-corrosion relationships have been observed in both

NaCl and H_2SO_4 electrolytes [163-167]. These results have been plotted in Figure 2.13, with the corrosion currents for each study normalized by the minimum corrosion current reported, to allow for easy comparison. Note that the grain size is plotted logarithmically to accommodate the large range. Examining the trends in Figure 2.13, it is clear that even for a single electrolyte, no consistent correlation with grain size exists. This could be due to any number of additional variables, including composition, texture, residual stress, and, of course, grain boundary network. These confounding factors make it difficult to determine the role of the grain boundary network, but Figure 2.13 motivates the search for a case where this might be more tractable. Data on the corrosion of nanocrystalline Ni produced by SPD would provide a helpful point of comparison because of the different GBCD expected, but this information is unavailable.
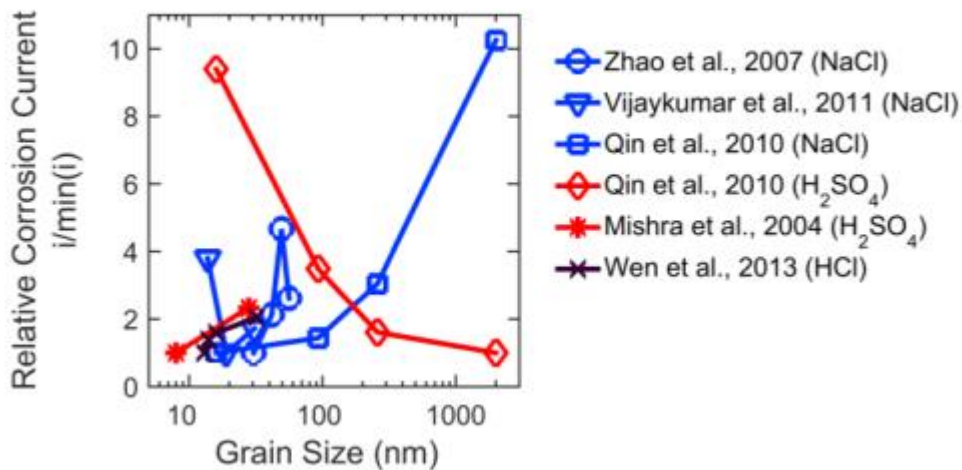
Figure 2.13: The normalized corrosion currents reported for electrodeposited Ni in several electrolytes and spanning the nanocrystalline and ultrafine grained regimes. The data for NaCl (blue lines) and H2SO4 (red lines) both show self-conflicting trends. All data shown is from prior literature [163-167].

For an example where the role of grain boundaries and processing route is clearer, it is instructive to consider the case of nanocrystalline Cu. While so far we have focused on Ni and its alloys, Cu is another FCC metal in which the same microstructural formation mechanisms,

44

such as grain refinement by LEDS and twinning by growth accidents, operate. The similarity between mechanisms provides some confidence that nanocrystalline Cu will show similar trends in GBCD as were observed in Ni. To recap, that would mean that severely deformed nanocrystalline copper is likely to have a preponderance of RHAGBs, while the deposited materials should be characterized by a high special fraction. This is turn should manifest as a difference in corrosion behavior, namely that deposited nanocrystalline Cu should be more corrosion resistant than Cu prepared by SPD. Fortunately, many corrosion studies of Cu exist that let this hypothesis be explored. For a uniform comparison, only those studies which used neutral or acidic chloride electrolytes (NaCl, HCl, Hanks solution) will be compared, because the corrosion of a metal is highly dependent on the corrosive media [162, 168-172]. Also to aid comparison, the nanocrystalline corrosion currents reported have been rescaled as the fractional difference from the coarse grained corrosion currents reported in each work. The intent is to minimize the effect of experimental differences, such as electrolyte concentration. The resulting relative corrosion rates are plotted in Figure 2.14 with data grouped by process type, either deposition or severe plastic deformation [162, 168-172]. It is obvious that the deposited materials are, as a group, more corrosion resistant that the plastically deformed ones.
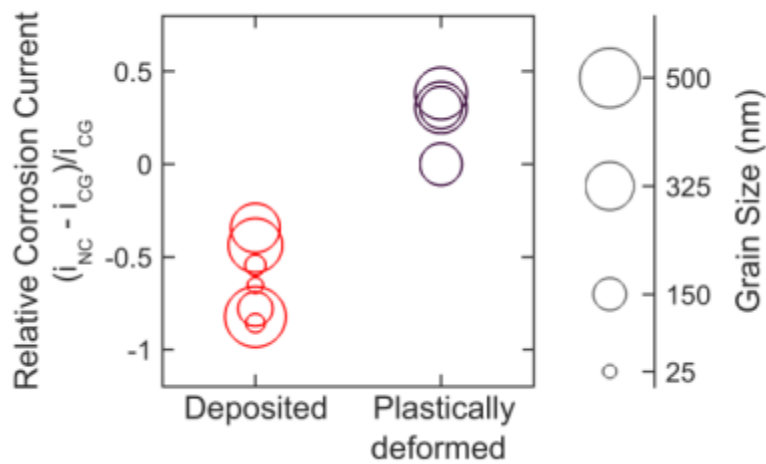
Figure 2.14: The effect of processing method on the corrosion of nanocrystalline copper manufactured by either deposition or severe plastic deformation. The fractional difference between the nanocrystalline and coarse grained corrosion currents from each study is shown, with negative ordinate values indicating an improvement in corrosion resistance. The area of each marker is proportional to that material's grain size. All data shown is from prior literature [162, 168-172].

This being a cross-study correlation, it is prudent to examine all factors that may be responsible for the observed behavior. In Figure 2.14, each marker has had its area scaled to be proportional to grain size, per the legend along the right side. From this, it can be seen that the trend holds across a range of grain sizes and that the process grouping is not merely serving as a proxy variable for grain size. Differences in impurity content could also be playing a role, as their segregation to grain boundaries can significantly enhance corrosion. Palumbo et al. [173] have attributed the (sometimes) superior corrosion performance of nanocrystalline metals to the dilution of impurities across a greater grain boundary area. However, electrodeposited materials in general have a higher impurity level than those prepared by equal channel angular pressing, which was the method of choice for every SPD study in Figure 2.14. If impurities were the controlling factor, a higher corrosion rate would be expected for the deposited group, but the opposite trend is found in Figure 2.14. With regards to strain energy, it could be hypothesized

that the higher strain energy of the severely deformed metals would promote corrosion, as it does for coarse-grained metals. However, Valiev et al. [174] have shown that short recovery heat treatments, which relax grain boundary structure and reduce strain energy, do not markedly improve the corrosion resistance of SPD materials. Differences in texture could also contribute to the corrosion resistance of the deposited metals. In the case of Inconel 600, Schuh et al. [175] showed that the corrosion rate of individual grains was proportional to their deviation from a {111} surface normal. One could therefore expect deposited materials, which often exhibit a {111} fiber texture, to exhibit enhanced corrosion resistance. Unfortunately, this is not an effect which is easy to control for, with Zhao et al. [162] showing how grain boundary character and texture have closely coupled effects on corrosion. In their work, nanotwinned copper was found to be more resistant to corrosion, with the effect being proportional to the extent of twinning [162]. However, the strength of the {111} texture was also proportional to the extent of twinning and distinguishing the effects proved challenging [162]. Most of the studies analyzed for Figure 2.14 do not include any texture information, which leaves open the possibility that the trend is due to a surface effect, rather than a grain boundary one [162, 168-172]. However, that conclusion presupposes that all of the deposited materials in Figure 2.14 have a {111} texture, even though there are many probable alternatives [176].

An interesting case that supports attributing the trend in Figure 2.14 to the GBCD is that of surface mechanical attrition of stainless steel [177]. It has been reported that a highly twinned nanocrystalline region of the sample was more corrosion resistant than the bulk, while a similarly grain sized area with a random boundary network was less resistant than the bulk [177]. While additional experiments would help bolster these conclusions, coupling our data to prior literature suggests that synthesis method affects the grain boundary networks of nanocrystalline metals and

47

that these features can help explain some of the variation in corrosion resistance that has been observed in past studies. This is in addition to the many other predicted effects of grain boundary type at the nanoscale, which notably include ductility and thermal stability [117, 156].

Conclusions

In summary, a systematic study of the grain boundary character distributions of several nanocrystalline metals, produced by different processing routes but with similar mean grain sizes, has been presented. It was observed that electrodeposition and sputtering produced similar GBCDs, due to their shared structure-determining kinetics, with growth accidents on {111} planes responsible for the high $\Sigma 3$ fraction [122, 123, 153, 154] that in turn leads to a high $\Sigma 9,27$ fraction [138]. These similarities were found in spite of differences in composition which should affect the stacking fault energies of the materials. The ball milled material exhibited a GBCD that was much different than the deposited GBCDs, with very few twins and many more $\Sigma 1$ boundaries. The GBCD of the ball milled material was quite consistent with prior reports on UFG metals, suggesting a continuity of the LEDS grain refinement mechanism to nanoscale grain sizes [122, 123, 135, 140, 141, 153, 154]. The ball milled GBCD also varied somewhat with milling time, even as grain size stayed roughly constant. These results were then applied to consider some prior literature on nanocrystalline corrosion, finding that differences in GBCD may explain why deformed and deposited nanocrystalline materials exhibit different corrosion resistance. The connection of GBCD to processing method and important material properties will hopefully motivate additional future work on other nanostructured materials. Such experiments will become more commonplace as TKD and PED become increasingly available to

48

researchers. As illustrated by the case of nanocrystalline copper corrosion, the GBCD can have a predictive power that can be even more important than grain size.

Chapter 3 - The Formation and Characterization of Large Twin Related Domains

Abstract

The enhanced properties of grain boundary engineered metals are a result of their unique microstructures, which contain large clusters of twinned grains, called twin related domains. These large twin related domains in grain boundary engineered Ni were found to form through a recrystallization process. Orientation mapping showed that the post-deformation heat treatment caused sparse nucleation of strain free regions that grew outward and underwent multiple twinning events, resulting in twin related domains containing hundreds of grains connected together in complex morphologies. A correlation was found between the size of the twin related domains and the overall twin boundary fraction. The same correlation was also observed in Cu and a Ni superalloy, showing that this is a general observation for grain boundary engineered microstructures. This finding can be understood through the topology of the twin related domains and an accompanying scaling relation is provided. The crystal orientations contained within each twin related domain were observed to depend on both the spatial correlation of twinning variants and the degree of branching in the twin boundary network. The results suggest a more natural way of quantifying grain boundary engineered microstructures and provide a step toward making a closer connection between processing, microstructure, and performance.

Introduction

Material properties can often be improved by controlling both the type and arrangement of grain boundaries, a process called grain boundary (GB) engineering [178]. These improvements have generally been linked to a profusion of twin boundaries, labeled as $\Sigma 3$ in the coincident site lattice (CSL) framework, making twin boundary fraction an important metric [94]. For example, Lin et al. [179] saw that the intergranular corrosion resistance of Inconel 600 was proportional to twin fraction. On the other hand, it has also been recognized that grain boundary topology, which cannot be assessed from boundary fraction, affects crack propagation [82, 160]. Taking a more holistic view, Gertsman and Henager [91] observed that clusters of many grains were mutually connected by twin boundaries in GB engineered Cu-Ni. Within each cluster, every grain was related by a $\Sigma 3^n$ misorientation [91]. This clustering concept was formalized by Reed and Kumar, who called such features twin related domains (TRDs) and offered a mathematical framework for their analysis [92]. Reed et al. [93] then showed how the length scale of TRDs can be used explain the fracture roughness of GB engineered and conventionally processed Ni subjected to intergranular stress corrosion. Likewise, Lind et al. [53] showed that TRD size affects the progress of thermal grain coarsening. As a whole, these studies demonstrate how the concept of TRDs can be a valuable tool for understanding how GB engineering affects material properties.

With mounting evidence that TRDs are important microstructural features, it is desirable to know more about how they form. The statistical increase in $\Sigma 3^n$ GBs brought about by low-strain recrystallization has been known for some time [98]. Lim and Raj [98] showed that the mechanism for this increase is $\Sigma 3$ twinning, with higher order $\Sigma 3^n$ GBs being formed by incidental $\Sigma 3$ interactions [98]. Their conclusions were reaffirmed by later transmission electron microscopy (TEM) observations showing how strain-induced boundary migration introduces

twins during GB engineering [100]. More recently, the effects of prior deformation and heat treatment on recrystallization twinning were quantified by Jin et al. [180]. Unfortunately, these sorts of ensemble boundary statistics do not provide the topological information needed to understand TRD formation. For example, Lind et al. [53] showed that the simulated reassignment of boundary types within conventional and GB engineered microstructures produces different TRD sizes at equal twin fraction. This indicated that a complete picture of TRD formation will require more information than simply the number of twins in the final microstructure. The formation mechanisms of large TRDs are also expected leave an imprint on their internal structure, not to mention the microstructure at large. Qualitatively, the thousand-member TRDs shown by Lind et al. [53] bear little resemblance to the textbook picture of convex grains subdivided by lamellar twins. It is presently unclear how the internal structure of these TRDs differs from those in conventional materials, in either kind or degree. Recent work by Cayron [52] has provided new metrics for assessing the internal structure of TRDs, especially regarding the orientations of their constituent grains. It was shown that stacking fault energy can affect internal TRD structure, and processing history might be expected to do likewise [52]. Applying these tools to TRDs in GB engineered materials provides an opportunity to better understand their formation and structure.

In this paper, we seek to understand how large TRDs form during a GB engineering process, how their topology develops, and how their internal structures differ. TRD formation is investigated by a series of interrupted annealing experiments, combined with orientation mapping. TRD boundary topology is considered, along with the probability of TRD coalescence. This leads to a scaling relationship linking TRD size to the twin fraction of the microstructure at large. Finally, we focus on understanding the internal structure of TRDs by

applying metrics previously proposed in the literature and by examining their graph structure. These results are then used to examine how large GB engineered TRDs compare to smaller conventional ones. Taken as a whole, this provides a description of how GB engineered microstructures form and how to naturally quantify them.

Materials and Methods

Varying degrees of cold work were applied to samples of commercial purity Ni (UNS N02201), oxygen-free electronic Cu (UNS C10100) and Inconel 718 (UNS N07718), followed by heat treatment. These materials were chosen because they can be readily grain boundary engineered and have a range of low to medium stacking fault energies. Inconel in particular is also of industrial significance in applications that can potentially benefit from GB engineering. The levels of deformation were selected to cover a range of GB engineering and conventional processes, with details presented in Table 1. The GB engineering treatments involve small deformations and are expected to produce high twin fractions, while the conventional processes have larger deformations and produce microstructures typical of commercially wrought material. Rolling was performed in a 10 inch mill, with no single-pass of less than 5%, and heat treatments were performed in air. Sample thicknesses are also listed in Table 1 because larger samples were observed to require longer times for complete recrystallization, presumably because they reached temperature more slowly. Specimens were water quenched, except for the Inconel samples, which were air cooled. Different material lots are identified in Table 1 because initial grain size and trace impurity content could have an effect.

Table 3-1: Processing, EBSD, and microstructural parameters

Table lists the rolling reduction, and heat treatment temperature and time for each material. Iterated steps are noted by the number of iterations followed by an 'x' and the details of the repeated step. The supplier lots and thickness after rolling are also included. The EBSD step and map sizes are listed, and can be compared to the grain and TRD sizes. Twin number fraction is also listed for comparison with other literature.

ID	Material	Processing Method	Thickness (in)	EBSD step size (µm)	EBSD map area (mm²)	Grain size (µm)	TRD size (quadratic mean)	Twin number fraction
1	Cu (1)[*]	60%, 500 ˚C/30min	N/A	1	4	17	4.7	0.25
2	Cu (1)[*]	2x(20%, 500 ˚C/30min)	N/A	1	4	32	18.4	0.36
3	Cu (2)	60%[**], 280 ˚C/195min	0.133	0.5	0.25	7	5.3	0.27
4	Cu (2)	60%[**], 500 ˚C/30min	0.133	0.5	1	8	2.4	0.17
5	Cu (2)	(60%[**], 500 ˚C/30min) + (20%, 500 ˚C/10min)	0.107	0.5	1	12	16.7	0.35
6	Cu (2)	(60%[**], 500 ˚C/30min) + 2x(20%, 500 ˚C/10min)	0.086	0.5	1	18	24.4	0.39
7	Cu (2)	(60%[**], 500 ˚C/30min) + 3x(20%, 500 ˚C/10min)	0.065	0.5	1	18	15.7	0.36
8	Ni (1)[***]	5x(20%, 900 ˚C/15min) + 900 ˚C/60min	0.413	2	4	54	3.0	0.22
9	Ni (1)[***]	3x(5%, 900 ˚C/15min) + 400 ˚C/24h	0.881	2	4	82	8.8	0.35
10	Ni (2)	25%, 800 ˚C/120min	0.286	2	4	96	1.9	0.14
11	Ni (2)	5%, 900 ˚C/15min	0.361	2	4	92	11.8	0.38
12	Ni (3)	25%, 900 ˚C/60min	0.388	2	4	62	2.0	0.12
13	Ni (3)	5%, 900 ˚C/15min	0.492	2	4	59	15.5	0.38
14	Inconel (1)	25%, 1020 ˚C/30min air cooled	0.375	2	3	24	2.8	0.21
15	Inconel (1)	as-received, 1030 ˚C/60 min air cooled	0.500	2	3	49	4.6	0.24

*These materials are the same used in Blobaum et al. [181], and were produced with a forging operation.

** Rolled immediately after prolonged submersion in liquid nitrogen

***The materials are the same used in Bechtle et al. [182]

Standard metallography techniques were used to prepare samples for electron backscatter diffraction (EBSD). Final polishing was performed with electropolishing when the stored plastic strain was of interest, in other cases mechanical polishing with colloidal silica was considered sufficient. EBSD data was collected using a Quanta 200 scanning electron microscope (FEI, Hillsboro, OR) equipped with a Hikari XP2 EBSD camera (EDAX, Mahwah, NJ). The map area and step sizes were selected to be suitable for the grain and TRD sizes of each sample, as listed in Table 1. The grain sizes are given as the circle equivalent diameter of the mean grain area. The orientation data analysis began with a standard dilation cleanup using commercial software (EDAX). Except when considering stored plastic strain, each grain was assigned a single average orientation and a 5˚ threshold was used for grain reconstruction.

Each TRD was reconstructed with a depth-first search for grains connected by Σ3 boundaries. This algorithm builds the twin network by starting at a random grain and exploring along a branch of twinned grains until no new twins are found, at which point it backtracks to another unexplored branch and the process repeats until every branch has been traversed. This search routine was repeated until every grain in the microstructure had been assigned to its parent TRD. A restrictive ±1˚ threshold was applied to identify Σ3 boundaries, in order to limit the influence of GBs that coincidentally have near-Σ3 misorientations [52, 53]. No higher order $\Sigma3^n$ boundaries were used to build TRDs because it has been shown that they do little to change the size of TRDs [53]. TRD size was characterized by the number of grains they contain rather than a physical length-scale, a method that allows for convenient comparison of TRDs across materials with different grain sizes. Within each TRD, the misorientation axis of every Σ3 boundary was tracked, after the method of Reed and Kumar [92]. Symmetry operators were

applied such that the four Σ3 variants were always expressed relative to the arbitrary starting grain, since each variant corresponds to one of the four unique <111> misorientation axes. These are then used to determine all of the $\Sigma3^n$ relationships within a TRD [52, 92]. This approach is necessary because the direct misorientation-based categorization of high order $\Sigma3^n$ relationships is impractical [52]. The number of $\Sigma3^n$ relationships increases exponentially with n, and they start to cluster very closely in orientation space at large values of n [72]. Once identified, each TRD (Figure 3.1(a)) can be conveniently represented by a network graph (Figure 3.1(b)), where each node (dot) represents a grain and each edge (line) a twin boundary. Mathematically, this information was represented by an adjacency matrix (T_{ij}), where each element records the twin variant connecting the ith and j^{th} grains, also shown in Figure 3.1(c). Another matrix can be easily calculated to find the $\Sigma3^n$ relationships between every pair of grains in the TRD, following Reed's concatenation rules [92].
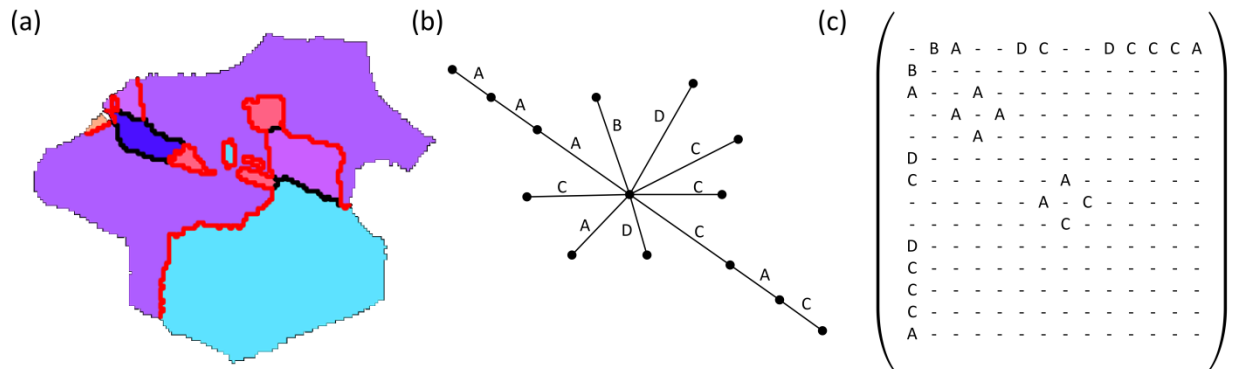
Figure 3.1: (a) The inverse pole figure color map of an example TRD and its corresponding representations as (b) a network diagram and (c) an adjacency matrix. Red lines in part (a) are twin boundaries, with other GBs shown in black. Each point in (b) represents a grain in (a). Each line in (b) corresponds to a grain boundary in (a) and an entry in (c).

Results and Discussion

Observations of TRD Formation during Annealing

The formation of large TRDs was investigated by interrupting the annealing step of a GB engineering process. Sections of Ni were rolled to 5% and then annealed for times ranging from

5 to 10 min. The microstructure after annealing for 5 min showed no change from the as-rolled state, with the grains remaining equiaxed and 16 μm in diameter. After 7 min, a few larger grains appeared in the microstructure, which are visible in the inverse pole figure (IPF) map in Figure 3.2(a). In this type of map, each pixel is assigned a color based on its orientation, which provides a means to visualize grains and texture. The subtle gradients in color within individual grains indicate lattice curvature, which is due to geometrically necessary dislocations (GNDs) accumulated during deformation. These color gradients can be seen more clearly in the small grains in Figure 3.3(a), which is enlarged from Figure 3.2(b) (7.5 min). The relative density of these defects can be approximated by analyzing the grain orientation spread (GOS) [46], also shown in Figure 3.2. GOS measures the average misorientation between every pixel in a grain and the grain's mean orientation [46]. It emphasizes grain-scale differences in GND density and residual plastic strain, although strictly speaking GOS lacks a quantitative relationship to either of these. Yellow/green grains in Figure 3.2 and Figure 3.3(b) have a high GOS, while blue grains are low GOS. After annealing for 7 min, most of the grains showed the same level of GOS that was found prior to annealing. This indicates that the residual plastic strain imparted by rolling has not yet been removed by either recovery or recrystallization. The key exceptions are the small scattered blue areas. These are relatively strain-free and correspond to the large grains visible in the IPF map. The appearance of large, strain-free grains was more pronounced after 7.5 min, as shown in Figure 3.2(b). After 8.5 min (Figure 3.2(c)), nearly the entire microstructure is composed of such grains and after 10 min (not shown), the change was complete.
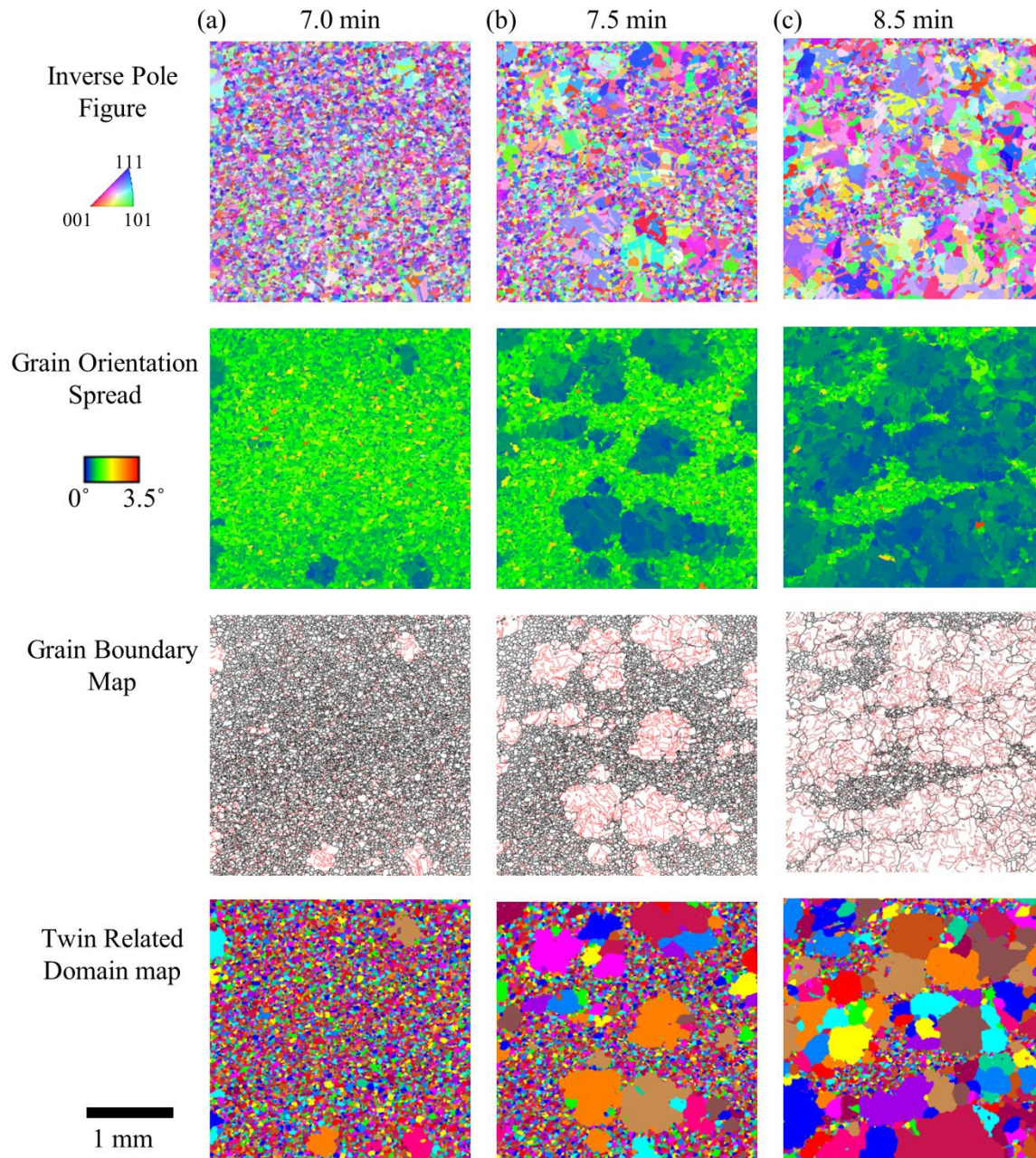
Figure 3.2: Orientation maps from a sample of Ni rolled 5% and annealed at 900C for 7, 7.5, and 8.5 min. The colors in the first row indicate grain orientation. In the second row, yellow/green colors indicate high residual deformation and blue indicates strain-free regions. The red lines in the third row are twin boundaries, black are TRD boundaries and all other GBs are gray. The colors in the fourth row identify each TRD.
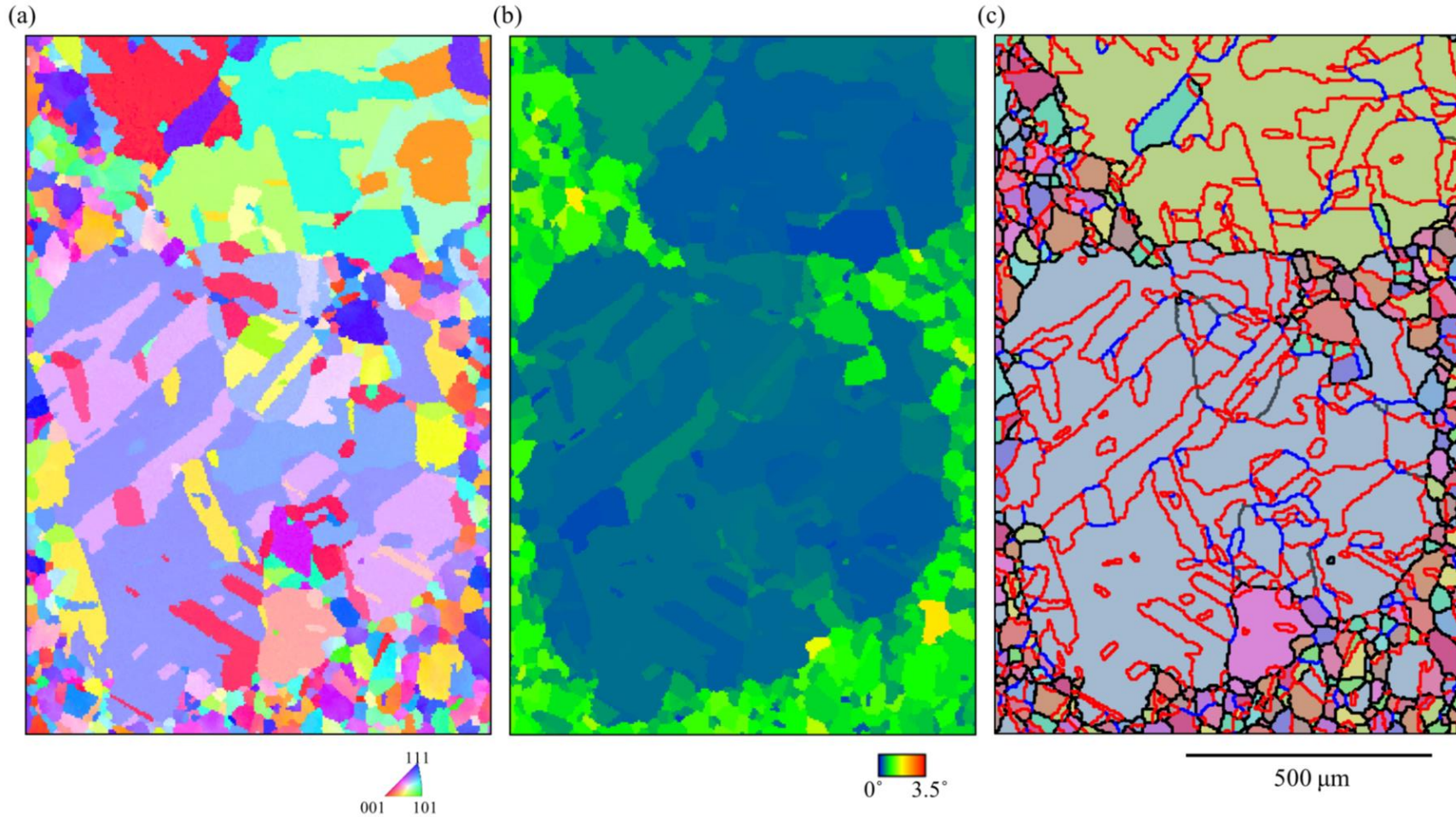
Figure 3.3: (a) Enlarged IPF, (b) GOS, and (c) TRD maps from the 7.5 min sample shown in Figure 3.2. In (c), Σ3 boundaries are represented by red lines, Σ9 and Σ27 by blue, TRD boundaries by black, and all others in gray.

The results presented in Figure 3.2 are a textbook example of primary recrystallization: the replacement of a deformed microstructure by new strain-free grains. While sometimes thought of as a higher deformation process, recrystallization in Ni can be induced at low strains via strain induced boundary migration [100]. After a ~7 min incubation time, recrystallized nuclei began to grow rapidly, consuming 30% of the deformed microstructure (GOS > 0.5) over the next ~30 seconds. This rapid evolution slowed as recrystallization neared completion, demonstrating the classic sigmoidal kinetics of recrystallization. Annealing times longer than 10 min produced only minor grain growth because the driving strain energy gradient had dissipated.

Comparing the three GB maps in Figure 3.2, it is obvious that recrystallization increased the fraction of twin boundaries (red lines). Figure 3.4 plots the overall twin fraction for intermediate stages and confirms that it increases in concert with the recrystallized fraction. In contrast, the twin fractions within the recrystallized and deformed regions remain constant during the process. This indicates that the overall change in twin fraction occurs because the recrystallized microstructure replaces the original one. Visually, this is apparent in Figure 3.2 where the recrystallized islands, blue in the GOS map, correspond with the clusters of twins in the GB map. Less obvious is that these recrystallized islands are also single TRDs. That is to say, all of the grains in each low GOS island are mutually connected by twins. This can be seen in the fourth row of Figure 3.2, where each TRD has been assigned an arbitrary color. It is likewise apparent in Figure 3.3(c), where the grain boundary map has been superimposed on an enlarged TRD map. This shows that the large TRDs formed as the result of recrystallization.
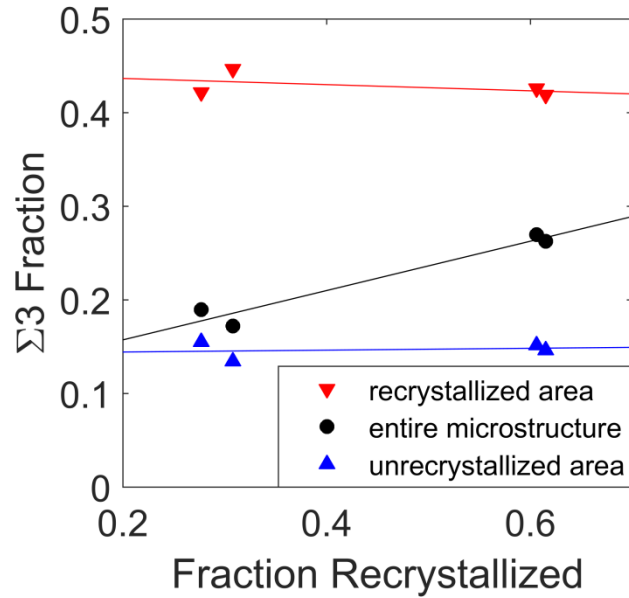
Figure 3.4: Twin number fraction for intermediate annealing stages, showing consistently high twin fraction in the recrystallized area (GOS < 0.5), low twin fraction in the unrecrystallized area (GOS > 0.6), and an overall twin fraction that reflects the material's composite nature.

TRD Formation as a Recrystallization Process

Regarding the formation of TRDs as a recrystallization process, it remains to discuss why they become so large in GB engineered materials. We will first examine if each recrystallized TRD originates from a single nucleation event, or if they somehow coalesce. Two independently nucleated TRDs can only coalesce into a single TRD if there is a $\Sigma 3$ at their impingement, as required by the definition of a TRD [53]. Warrington and Boon [183] give the probability ($P_{\Sigma 3}$) of forming a $\Sigma 3$ in a random polycrystalline aggregate, which is only ~0.02% for a ±1° tolerance. If the orientations along a TRD boundary were independent, the probability (P) of coalescence would then be:

$$P = 1 - (1 - P_{\Sigma 3})^m$$

Equation 3.1

or,

$$P \approx mP_{\Sigma3}, \text{ for large } m \hspace{4em} \text{Equation 3.2}$$

where m is the number of grain boundaries along the TRD boundary. For two TRDs that share a 100 GB-long boundary, the probability of coalescence would only be ~2%. Therefore, TRD coalescence is unlikely to factor predominantly into TRD formation, especially during the early stages of their growth. Even were coalescence to occur, the connectivity would be minimal and through a Σ3 that would probably be far from coherent. A Σ3 that formed by this sort of coincidence would likely be far from the ideal CSL relationship because the two orientations involved would be independently fixed by their parent TRDs.

A high density of nuclei would cause TRDs to impinge while still relatively small, as noted by Xia et al. [99]. Examining specimens 8-13 in Table 1, TRD nucleation density appears to be controlled by the level of cold work, with heavier deformations leading to denser nucleation (smaller TRDs). This is in agreement with other observations of Ni recrystallized after 5-50% strain [99]. The final microstructure for the material in Figure 3.2 had a TRD nucleation density of less than 40/mm^2. Minimizing TRD nucleation density would be desirable because of the benefits of large TRDs [53, 93], the origins of which will be discussed more in later sections. It remains an open question how low this density can be driven because a certain minimum deformation is required for recrystallization. Assuming a strain-induced boundary migration mechanism, one would expect a large initial grain size to reduce TRD nucleation density [32]. The density of second phase particles and annealing temperature should also be important variables affecting TRD size [32].

In the absence of twinning, the observed low nucleation density would have produced a microstructure ~10 times coarser than observed. This causes the TRD maps in Figure 3.2 to bear a strong resemblance to abnormal grain growth. In fact, early work on GB engineering attributed clusters of grains connected by special boundaries to abnormal grain growth and not primary recrystallization [97]. The two can be distinguished on the basis of the inhomogeneity of residual plastic strain [32]. In the case of primary recrystallization, intermediate stages will show inhomogeneous dislocation density, with a transition from high to low overall density as annealing progresses. In abnormal grain growth (secondary recrystallization), the dislocation density will remain low and homogenous. Figure 3.2 and Figure 3.3 demonstrate that recrystallization, not abnormal grain growth is occurring. This distinction between primary recrystallization and abnormal grain growth helps to explain why so many twins develop. In primary recrystallization, inhomogeneous dislocation density provides a driving pressure ~100 times greater than grain boundary energy does for secondary recrystallization [32]. The propensity for twinning has been shown to be proportional to the strength of this driving force [180, 184]. Indeed, a material which gains twins during primary recrystallization may lose some of them during subsequent grain growth [180].

From the IPF and GOS maps in Figure 3.2, we are confident that this GB engineering routine is a recrystallization process. The small deformation causes a low density of nucleation sites, from which large TRDs form by multiple twinning during boundary migration. These twinning events are driven by the gradient in dislocation density between the deformed and recrystallized regions, which would not be present in normal grain growth or secondary recrystallization. This is precisely the multiple twinning that Gertsman and Henagar [91] proposed from their early observation of TRDs, and also matches Lim and Raj's [98] even earlier

conclusions. The result is TRDs that grow to contain many twins and eventually impinge, forming a GB engineered microstructure.

Topological Models for TRD Growth

The recrystallization process described above leads to a distinctive GB topology. Consider the arrangement of boundaries in Figure 3.3(c), which shows two large recrystallized TRDs and the surrounding unrecrystallized material. Based on the previous section, it is clear that the two large TRDs are in the process of consuming the smaller grained regions. Note how the boundary between these two groups contains no twins. The same is true for the boundary where the two large TRDs have already impinged. However, within each TRD, there is a profusion of twinning, and also many $\Sigma 9$ and $\Sigma 27$ boundaries, shown in blue. This pattern has consequences for the final microstructure, including the overall twin fraction and the network connectivity. How this topology develops, and its effects, are considered in the rest of this section.

We will start with a simple geometric model based on the Eden cluster growth model (ECGM) [185]. This is a purely geometric model that has been used to study growth processes as diverse as bacterial colonies [185] and the crystallization of amorphous Al-Ge [186]. We use the ECGM here to model an artificial grain structure and test the effect of TRD nucleation density on the overall microstructure. Artificial 'TRDs' were built by first assigning random orientations to a number of seed locations within a 2D hexagonal lattice, which are analogous to nucleation sites. A random quaternion was used to create a uniform orientation distribution. The next step was to assign a $\Sigma 3$-related orientation to a neighboring location, creating a 'twin'. More 'twins' were added to the growing clusters until the simulation cell was filled (10,000 grains). This is analogous to the multiple twinning events that occur during TRD growth. No orientation was changed after its initial assignment. This reflects the observation that grains

within recrystallized TRDs are very stable [53]. To be clear, the ECGM does not include physical models for nucleation or growth, but is a set of geometric rules based on the phenomenology common to many growth processes [185].

The structures created by the ECGM contain clusters of grains connected by 'Σ3' boundaries and surrounded by an envelope of 'non-Σ3' boundaries, much like the real TRDs already discussed. This can be seen in the example ECGM output in Figure 3.5, where 'Σ3' boundaries are shown in red, TRD boundaries in black, and all others in gray. Examining instances of the ECGM having different seed densities, a correlation between 'twin' number fraction and 'TRD' size emerges. As 'TRD' size increases, the 'twin' fraction initially rose rapidly before eventually plateauing. This trend is shown as the dashed gray line in Figure 3.6, and it can be compared directly to real materials characterized via EBSD. The TRD sizes and twin fractions calculated for every material in Table 1 are plotted in Figure 3.6. TRD size was taken to be the quadratic mean of the number of grains per TRD because this weights them based on the fraction of the total microstructure they form. It is interesting that this simple model captures much of the TRD size dependence on Σ3 content. Given that there are no fitting parameters, the data agrees surprisingly well with the ECGM, suggesting that nucleation is the critical event that determines TRD size.

Figure 3.5: A close-up view of an Eden cluster growth model result. The red lines indicate 'twin' boundaries; black lines are 'TRD' boundaries. Other boundaries are shown in gray. The background color distinguishes each TRD.
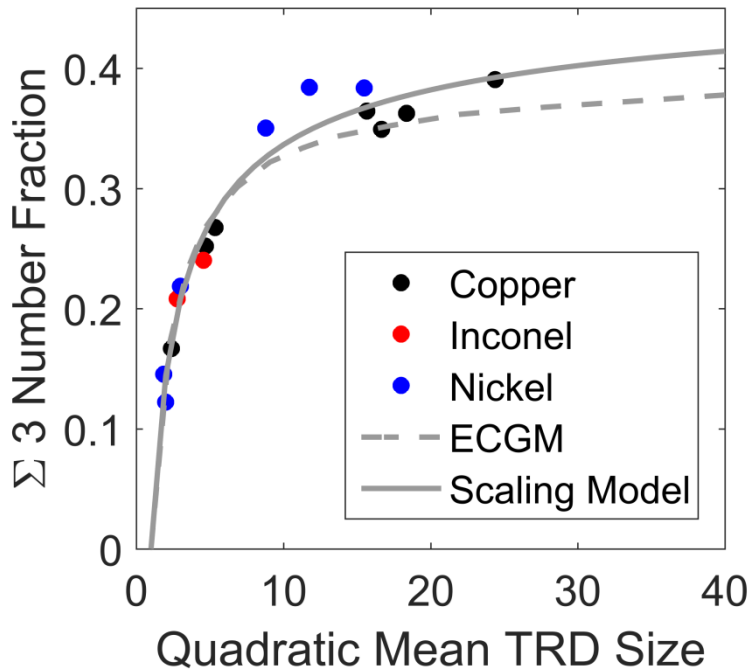
Figure 3.6: Twin number fraction relative to twin related domain size are shown for the materials listed in Table 1. The predictions of the Eden cluster growth model and a new scaling relationship are shown as dashed and solid lines, respectively.

This agreement between the ECGM and experimental data stems from a topological similarity between the two due to the external boundaries of a TRD being composed entirely of non-Σ3 boundaries. By the same tautology, all of the Σ3 boundaries lie within TRDs. From these two facts, a 2D geometrical argument can be constructed to explain the ratio of Σ3 to non-Σ3 GBs. As a TRD grows, an increasing fraction of its grains will lie in the interior area than at the perimeter. The usual scaling of area ($\propto length^2$) versus perimeter ($\propto length^1$) will then cause microstructures with larger TRDs to have higher twin fractions. This can be stated mathematically as follows:

$$f_{\Sigma 3} = \frac{c' B_{int}}{B_{int} + B_{ext}} \qquad\qquad \text{Equation 3.3}$$

where $f_{\Sigma 3}$ is the Σ3 number fraction, B_{int} is the number of boundaries inside TRDs, and B_{ext} is the number of grain boundaries around TRD perimeters. The constant c' assumes a fixed distribution of Σ3^n boundaries inside TRDs. If we simplistically assume TRDs to be large circles composed of smaller circular grains, then Equation 3.3 can approximated as:

$$f_{\Sigma 3} \approx c\,\frac{N - \sqrt{N}}{N} \qquad\qquad \text{Equation 3.4}$$

where N is the TRD size, and c is a proportionality constant that incorporates c' and geometric constants. Figure 3.6 shows the results of fitting Equation 3.4 to the EBSD data, shown as the solid line. Again, the agreement with the data is quite good, with a coefficient of determination or r-squared value of 0.96.

The limiting cases of Equation 3.4 are informative. In the trivial case of a microstructure composed of TRDs all having only 1 member, it correctly predicts a twin fraction of 0. In the case of infinitely large TRDs, it requires that the twin fraction approach c, which a least squares fit shows to be ~0.5. Equivalently, we could say that at a twin fraction of c (apparently ~0.5),

TRDs approach infinite size. Infinite TRD size prohibits a percolating path of weak (non-$\Sigma 3$) boundaries because such paths only exist at TRD boundaries. This can be compared to the results of random percolation models. Accounting for triple junction constraints, Schuh et al. [160] predicted that a twin number fraction of 0.275-0.335 would prevent percolation of non-$\Sigma 3^n$ boundaries. These values are much lower than the 0.5 $\Sigma 3$ threshold fraction that Equation 3.4 predicts. In fact, all of the microstructures studied here contained weak percolating paths, despite several having twin number fractions that exceed Schuh's predicted threshold. Preventing non-$\Sigma 3$ GB percolation in GB engineered materials is apparently more difficult than random percolation models predict. This is similar to the observation of Basinger et al. [187], who noted that the non-random arrangement of grain boundaries could promote percolating paths. In essence, the formation of large TRDs introduces twins in an ordered way that, compared to randomly distributed twins, is inefficient at breaking up weak GB paths.

Equation 3.4 also predicts that a high twin fraction will only occur for microstructures composed of large TRDs. As previously discussed, TRD size is inversely related to the level of pre-recrystallization deformation and therefore twin fraction should be as well. Indeed, prior literature generally shows just such a trend for Ni [99, 182, 188, 189]. With one exception, all of the single iteration processes studied by Guyot and Richards [189] show this trend. That exception is the case of Ni deformed to 2.5% and recrystallized at 900 °C, which showed a much lower twin fraction than did their sample deformed to 5% strain [189]. A probable explanation for this data point is that low strain was insufficient to cause recrystallization. Shimada et al. [190] found a similar trend in 304 stainless steel, with a peak special boundary content occurring for a 5% rolling reduction. This explains why many GB engineering treatments use strains in the range of 5-20% [89, 181, 182, 191, 192], even though absolute twin density increases with

higher strains [180]. This also points toward a limit of current GB engineering techniques, and explains their apparent inability to create the ideal 'twin limited' microstructure. Ideally, the pre-recrystallization strain would be large enough to drive TRD growth and frequent twinning, but simultaneously small enough to reduce nucleation density to nearly zero. These goals are competing, if not necessarily incompatible.

Characterization of Internal TRD Structure

The two large TRDs in Figure 3.3 contain grains of many different orientations. This is quite different from the lamellar TRDs found in columnar nanotwinned materials [156]. While columnar TRDs can also contain many twins, they all share a common twinning plane and are composed of only two distinct orientations [156]. This type of difference would not be evident from the size or deformation state of the TRDs, which are the only distinctions that we have so far drawn. The orientations of a TRD's constituent grains therefore provide another valuable source of information. The goal of this section is to analyze the orientations within TRDs to understand more about how large TRDs form and how they may differ from smaller ones. This will also address if the TRDs in GB engineered materials differ from those in conventional materials by some characteristic other than size.

Cayron [52] proposed to characterize the diversity of orientation within a TRD using a metric called polysynthetism. The definition of polysynthetism (P_s) is given by:

$$P_s = \frac{N}{N_o} \qquad \text{Equation 3.5}$$

where, N_o is the number of unique orientations within a TRD, as determined by reconstructing the twin graph [52]. Here, N remains the number of grains in a TRD. This can be interpreted as an inverse measure of orientation diversity, with high values indicating relatively few unique orientations, compared to the TRD size.

We measured the polysynthetism of each TRD in all of the samples listed in Table 1, with the results plotted in Figure 3.7(a). The mean value at each TRD size is shown. Here we have again comingled the data from samples 1-15 because an individual analysis added little insight, which is in line with the materials' similar stacking fault energies [52]. The general trend is for small TRDs to possess a lower polysynthetism than larger ones. In other words, large TRDs in the GB engineered materials contain fewer unique orientations relative to their size than do the small TRDs in the conventionally processed materials. There is a kind of diminishing returns in which a growing TRD gains new grain orientations at a rate inversely related its size.
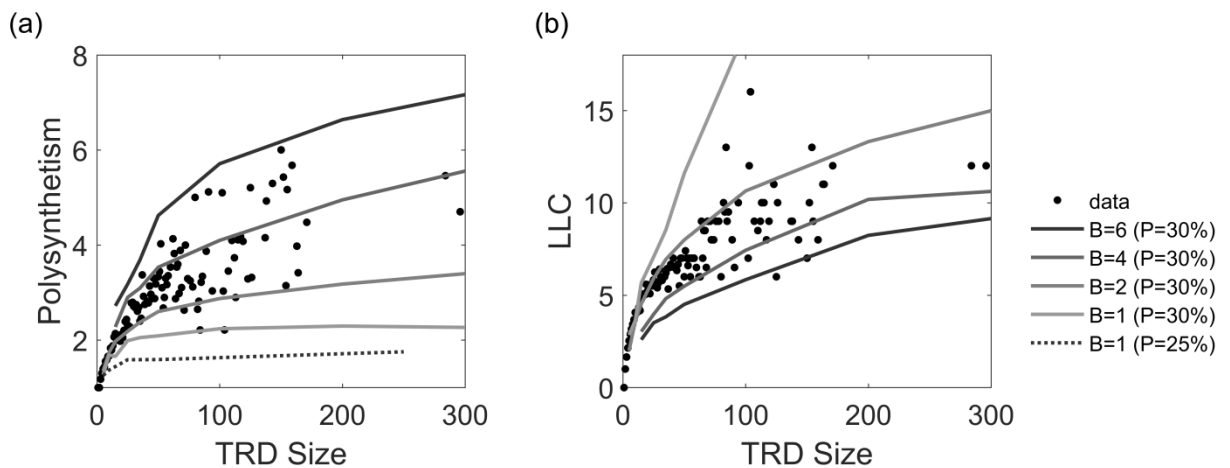
Figure 3.7: The measured values of polysynthetism (a) and the length of the longest twin chain (b) are plotted, with the mean value at each TRD size shown. Trend lines for simulated twin graphs with a range of repeated twinning probabilities (Pr) and branching factors (B) are also shown.

To understand how microstructure affects polysynthetism, synthetic twin network graphs were simulated. The simplest of these is a linear chain model, where one grain is twinned to a second, which is twinned to a third, and so forth. The only two parameters in this model are the length of the chain and the order of twin variants. The order of the twinning variants requires particular attention. As has been described by Reed and Kumar [92], grains connected by two

consecutive and identical twin variants have the same orientation ($\Sigma1$). Consecutive, but non-repeated, twinning generates a $\Sigma9$ relationship. We will quantify this as the probability of repeated twinning P_r, defined as:

$$P_r = \frac{n_{\Sigma1}}{n_{\Sigma1}+n_{\Sigma9}}$$ Equation 3.6

where $n_{\Sigma1}$ is the number of $\Sigma1$ relationships between second nearest neighbors in a TRD's twin graph, and $n_{\Sigma9}$ is the like measure of $\Sigma9$s. Intuitively, a high P_r would be expected to produce a high polysynthetism. For a $P_r = 1$, an infinitely long twin chain will have an infinite polysynthetism [52]. Similarly, an infinite twin chain with $P_r = 0$ would have a polysynthetism of 1. If each of the four possible twin variants were always equally probable, then the expected value of P_r would be 0.25. Using this value, many twin chains were generated, their polysynthetisms computed, and the means at a range of TRD sizes plotted in Figure 3.7(a). These are shown as the dashed gray line labeled '$P_r = 0.25$, $B = 1$.' Obviously, this model does not reflect the data well, predicting only about ½ the polysynthetism actually observed in the large TRDs. The arbitrary use of $P_r = 0.25$ is a likely suspect for the poor agreement, there being little basis for assuming the twinning variant is selected at random. Measuring the actual P_r in the data sets, it was found that the mean value for all TRDs is about 0.3. As can be seen in Figure 3.8(a), P_r is only weakly correlated to TRD size, having a Pearson correlation coefficient of -0.23. Repeating the simulations with this new value of $P_r = 0.30$, produced the line shown on Figure 3.7(a) that is labeled $P_r = 0.30$, $B = 1$. While the predicted polysynthetism is greater than it was for $P_r = 0.25$, it still falls well short of the data. This implies that the model is missing some import aspect(s) of TRD structure.
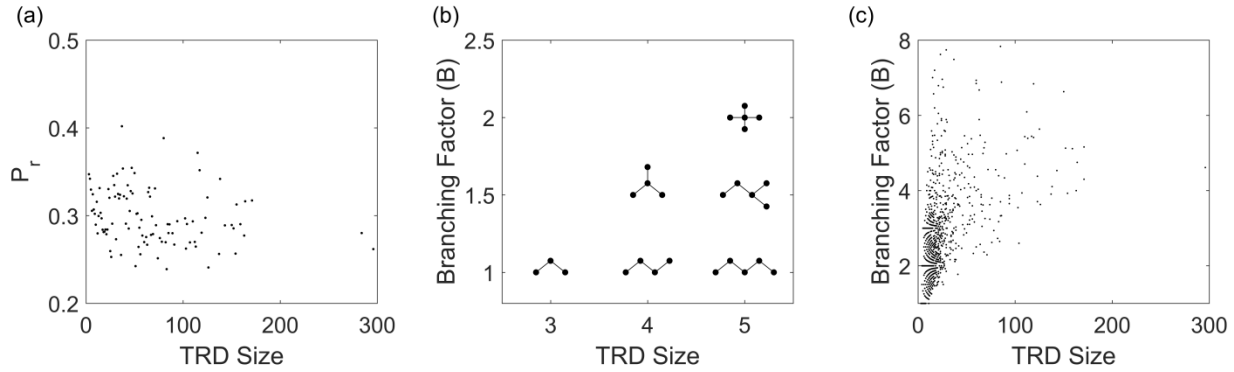
Figure 3.8: (a) The measured probability of repeated twinning, with the mean value at each TRD size shown. (b) Several example twin networks are plotted at positions corresponding to their sizes and branching factors and (c) the experimental values for branching factor.

One possible inadequacy is that real TRDs are not composed of linear chains, instead having complicated topologies like the examples in Figure 3.1, Figure 3.2, and Figure 3.3. To quantify this, we have adapted Bertz's [193] analysis of branching hydrocarbon chains. Our modification is to normalize Bertz's [193] branching factor by its minimum possible value at each TRD size. This new branching factor (B) is given by,

$$B = \frac{1}{2(N-2)}\sum_i^N d_i(d_i - 1)$$

Equation 3.7

where, d_i is the degree of each node i in a TRD's twin graph and N is still the number of grains in the TRD. The value of d_i is equivalent to the number of twin-neighbors that each grain has. This metric is always 1 for linear chains and increases for star topologies, with larger stars having greater branching factor values. This provides a way to categorize the branching in twin graph networks. The intuitive nature of branching factor is shown in Figure 3.8(b), where example TRD graphs are arranged according to their size and branching factor. The branching factors measured for each TRD in the EBSD data are shown in Figure 3.8(c). The trend is for a branching factor that is low for small TRDs and higher for large TRDs. Large TRDs (N>100), have a mean B value of 5.2 with a standard deviation of 1.9. To apply this network characteristic

to the analysis of polysynthetism, several thousand random networks were generated with varying degrees of branching. This was done by growing them outward from a starting node, and at each new node determining the degree by rounding a lognormally distributed random number. This distribution is convenient for always producing a positive number, and is otherwise a somewhat arbitrary choice. The random distribution creates nodes with varying degree, like those observed in real twin networks. To get a range of networks, the mean and variance of the distribution were varied. The mean probability of repeat twinning was held near the measured value of 0.30. This library of simulated TRDs was then sorted by branching factor and TRD size, and the mean values of polysynthetism calculated. In the extreme case of $B = 1$, this model simplifies to the linear chain model. The results are plotted in Figure 3.7(a), where it can be seen that higher branching factors increase polysynthetism. Importantly, the values of B where the simulations match the data best are within the range of the measured B values.

Before discussing the implications of P_r and B, it is worth checking if this analysis holds for metrics other than polysynthetism. The same line of reasoning and model generation was repeated to analyze the length of the longest twin chain (LLC) [52]. Also proposed by Cayron [52], LLC is defined as the highest $\Sigma 3^n$ relationship that exists in a TRD, irrespective of adjacency. It is relatively straight forward to calculate using the methods outlined by Cayron [52], or Reed and Kumar [92]. Figure 3.7(b) shows the measured values of LLC for the same set of materials discussed for polysynthetism. The trend lines in Figure 3.7(b) were generated using the same synthetic twin graphs as for polysynthetism. Again, the simulations match the data at branching factor values within the measured range. This suggests that P_r and B are describing polynthetism and LLC in a microstructurally meaningful way.

73

The preceding paragraphs aimed to show that the probability of repeated twinning (P_r) and branching factor (B) measure important aspects of TRD structure. If this is accepted, then it is noteworthy that P_r was not correlated with TRD size. That indicates the GB engineering does not significantly change the tendency for adjacent twins to share a misorientation axis. This might be surprising, given the different appearance of twins in GB engineered and conventionally processed materials. It also supports the idea that annealing twinning is responsible for forming both the large and small TRDs. On the other hand, there is a significant shift in B between the GB engineered and conventional microstructures. The higher branching factors in the GB engineered materials confirm the intuitive sense that GB engineered TRDs are different than similar sized clusters of lamellar twins, the latter having a branching factor of 1. This is probably a consequence of the dimensionality of their growth, GB engineered TRDs being 3D and lamellar ones being essentially 1D and having no opportunity to branch. Other forms of TRD growth may exist that produce characteristic differences in the probability of repeated twinning or branching factor. Annealed nanocrystalline foils can form TRDs by quasi-2D annealing twinning [194], and are therefore something of an intermediate case between GB engineered (3D) and lamellar TRDs (1D). It would also be interesting to examine twinning caused by grain rotation in nanocrystalline metals, as has been observed in MD simulations [195]. Perhaps these rotation induced twins can be distinguished from annealing twins with these new metrics, which is currently difficult to infer [196].

Conclusions

Twin related domains are unique building blocks of grain boundary engineered microstructures. Interrupted annealing experiments showed that they form by a recrystallization process that involves a low nucleation density and multiple twinning. An analysis of TRD

topology demonstrated how TRD size and twin fraction are related. This same analysis also suggested that percolation models overestimate the long range connectivity of $\Sigma 3$ networks. It was also shown that the constituent orientations of a TRD depend on the twin network's probability of repeated twinning and branching factor. The branching factor indicated that GB engineered TRDs are quite different than simple lamellar structures, most likely because of how they grow. In contrast, the probability of repeated twinning was nearly uncorrelated with TRD size, indicating a similarity in twinning mechanism.

Chapter 4 - The relative effect of twin boundaries on grain boundary strengthening

Abstract

The relative contribution of annealing twins toward grain size strengthening was measured using data from both new experiments and the prior literature. The yield strength and hardness of nickel and brass specimens were analyzed in relation to their densities of twin boundaries and random high angle boundaries. The relative effect of each boundary type was determined by applying Bayesian regression to a modified version of the Hall-Petch equation. In this formulation, grain size is replaced by boundary length density, which can be arbitrarily subcategorized and weighted. This reframes the usual question of whether or not to count twins as grain boundaries, instead allowing their fractional contribution to be quantified. The results from nickel suggested that twins add about 44% as much strength as random high angle grain boundaries. For brass, twins were only about 20% as effective as other boundaries. The credible intervals strongly reject the common assumptions that twins are either equivalent to other grain boundaries, or that they provide no strengthening.

KEYWORDS: Grain Size, Strengthening, Grain Boundaries, Twin Boundary, Hall-Petch

Introduction

Hall's [197] famous observation that yield strength is proportional to the inverse root of grain size has provoked a great deal of research into the underlying mechanisms and limits of the phenomena [8]. Among the competing physical interpretations that have been proposed [16, 197, 198], a unifying feature is their use of grain size for length scale. This choice implies that all grain boundaries contribute equal strength, even though nothing in the models' physics requires this. The reason for this limitation is that the concept of grain size requires a dichotomous definition for grain boundaries. This creates difficulties for studying highly twinned materials, since the mechanical response of twins is different from high angle boundaries. Slip-trace analysis has shown that twin boundaries can inhibit slip transfer and cause secondary systems to activate, much like other grain boundaries [199-203]. Unlike random boundaries, it has also been seen that properly aligned slip systems can cross twin boundaries with little resistance [199-202, 204]. These findings are mirrored by in situ TEM observations of dislocation-twin boundary interactions [200, 205]. Recently, Pang et al. [206] used a 3D orientation mapping technique to show that deformation caused the most lattice curvature near high angle boundaries, followed by volumes near twins, and then the grain interiors. Annealing and growth twins are widely thought to oppose deformation [59, 199, 203, 207-209], although probably to a lesser than random high angle grain boundaries [200, 210-212]. Still, there is some dissent from this view, with some arguing twins provide negligible strengthening [213], or even cause softening [214]. As a result, there is widespread confusion about how twins should be regarded in the context of the Hall-Petch equation, sometimes being counted as grain boundaries, and other times ignored.

It is desirable to quantify the strengthening power of twins more precisely, and more generally to find a way of incorporating relative (non-integer) boundary strengths into a Hall-

77

Petch type equation. This is especially important for emerging materials with extreme twin fractions or densities, like nanotwinned and grain boundary engineered metals. In the case of nanotwinned metals, it has been shown that a high density of twin boundaries can create very high strengths without the loss of ductility common to nanocrystalline metals [59]. Understanding the strengthening role of twin boundaries is of obvious importance for these materials [209]. This information would also help to understand the range of relative strengths that have been reported for grain boundary engineered materials, which have high twin fractions [181, 182, 215].

Attempts to resolve how twins should be considered in the context of the Hall-Petch equation have typically centered on which grain size metric produces the more satisfying fit [207, 208, 216]. Miura et al. [216] argued that twins should be counted as grain boundaries because that caused the Hall-Petch constants to be closer to their theoretical predictions made from single crystal strengths. Babyak and Rhines [207] compared the hardness of brass samples to their grain boundary areas, which showed better linearity when twins were included. Kral et al. [208] used a similar approach, but with the more familiar inverse-root dependence on grain size. For both brass and a nickel alloy, Kral et al. [208] found that counting twins as grain boundaries produced a better fit. There is a general consensus that considering twins to be grain boundaries produces better agreement with the Hall-Petch relation, but as Kral et al. [208] said in summarizing their results, "the relative influence [of twins] compared to random high angle grain boundaries has not been determined."

We propose a modification to the Hall-Petch equation that will allow it to model the comparative strengthening effect of different grain boundaries. Original data will then be used to estimate the relative strength of twins, with a discussion of possible confounding factors. These

results will then be compared to a reanalysis of Babyak and Rhines' data. Along with the most likely value for the relative strengthening effect of twins, a statistical analysis will be used to find the credible range of values. To be as generally applicable as possible, an agnostic view of the physical mechanisms of the Hall-Petch effect will be maintained as far as possible.

Materials and Methods

Pure Ni (UNS N02201) was selected for this study because it allowed a wide range of twin fractions to be produced, which was critical if the data were going to be sensitive to the hypothesis. This was possible because nickel's stacking fault energy (SFE) is low enough to facilitate grain boundary engineering, but high enough that low twin fractions are also achievable via conventional processing. The high twin fraction samples were created with a single-step, low deformation (5%), grain boundary engineering route. Some of the mechanisms of this process were recently presented elsewhere [217]. The low twin fraction materials were produced with a heavier deformation of 25%. In both cases, the deformation was introduced by rolling. The heat treatments required for recrystallization and grain growth were performed in air, followed by air cooling. A range of annealing temperatures and times were used to produce varied grain sizes, and are listed individually in Table 4-1.

Electron backscatter diffraction (EBSD) was performed to determine grain boundary types and densities, using a Quanta 200 scanning electron microscope (FEI, Hillsboro, OR), equipped with a Hikari XP2 EBSD camera (EDAX, Mahwah, NJ). Specimens were prepared by standard metallography techniques, followed by electrochemical polishing to ensure all surface damage was removed. For determining grain boundary character, every EBSD map had an area of 4 mm^{2,} and a scan step size of 2 µm. This gave a resolution of 1/20th the smallest mean grain size, although some of the narrowest twins observed were on the order of 2 µm thick. For

texture analysis, larger maps were collected at coarser resolution, capturing a minimum of 2600 grains. The data was processed with a standard dilation cleanup, followed by grain reconstruction using a minimum misorientation of 5°. Twin boundaries were identified using the coincident site lattice model and the Brandon criterion [49, 50]. Except for twins, no distinctions will be made between other grain boundaries, with all boundaries misoriented by more than 5° grouped under the loosely applied term 'high angle'. Boundaries with misorientations below 5° were ignored. While this marginalizes low angle boundaries, their fraction is essentially constant across every sample and so should not affect the results. Wherever the relative fractions of boundary types are reported, they were calculated in terms of length. Where grain size is reported, it was found by first determining grain areas, with twins counted as grain boundaries, and then the mean area was converted into a circle equivalent diameter.

Mechanical properties were measured with subscale tensile testing, with gauge sections measuring 3x3x11 mm. This size reduced the amount of material required while maintaining a minimum of ~25 grains through the thickness, which is sufficient to be representative [218]. The specimens were cut with electrodischarge machining because they were easily deformed by conventional machining, and even very small prior strains would overwhelm the expected effect of grain size strengthening. The specimen stress axis was aligned to the material's rolling axis. A table-top load frame (Instron 5848, Norwood, MA) was driven under displacement control to pull the specimens at a nominal strain rate of 4.5×10^{-4} s^{-1}. High precision measurement equipment was used because the expected differences in yield strength were small. Load was measured with a 2 KN load cell having a minimum accuracy of 0.5 N for loads below 200 N and 0.25% for higher loads (Instron 2530-418). Strain was measured with a clip-on type extensometer meeting the class B1 standard of ASTM E83 (MTS 632.26B-20, Eden Prairie,

MN). The yield strengths were calculated by using the linear hardening regime to back-extrapolate the stress at zero strain, as proposed by Kocks and Mecking [219]. This method produced results similar to the more common 0.2% offset method, but resulted is a slightly lower variance.

Theory

Pande et al. [210] have offered a variant on the Hall-Petch model that allows twins to be given a discounted importance by using an 'effective' grain size. This model was shown to perform well compared to the classic Hall-Petch model, but is limited by an assumed relationship between grain size and twin density [210]. One way to generalize this idea is to replace the 'effective' grain size with grain boundary density, which is easily measured with EBSD. Boundary density has previously been incorporated into the Hall-Petch equation by Hansen [220] to account for low angle boundaries in deformed samples. In that work [220], the usual grain size term was left unchanged and a new term added to increase the predicted strength in proportion to the density and misorientation of the low angle boundaries. Reformulating the Hall-Petch equation entirely in terms of boundary density allows an arbitrary number of grain boundary types to be consider, each with individual weighting factors. In this form, the yield strength (σ_y) can be expresses as,

$$\sigma_y = \sigma_0 + \left(\sum_i k_i \rho_i \right)^{1/2} \qquad \text{Equation 4.1}$$

where k_i are the strengthening coefficients for each type of boundary, which have densities ρ_i. The exponent is ½, instead of the more familiar -½ because boundary density is inversely related to grain size. The boundary density (ρ_i) would be best given by the boundary area per volume, but can be estimated from a 2D cross section as the boundary length per area. The term σ_0 has

the same meanings as in the usual Hall-Petch equation and can be thought of as providing the yield strength at infinite grain size, or equivalently zero boundary density.

If there is assumed to be a single value for all k_i, and also that mean grain size is inversely proportional to boundary density, then Equation 4.1 reduces to the usual Hall-Petch equation. The assumption that mean grain size is inversely proportional to boundary density implies a fixed distribution of grain sizes and shapes, i.e. all microstructures compared must be self-similar. This is actually not a new assumption, and is implicit in the conventional Hall-Petch equation, which does not contain any parameters characterizing the grain size distribution or grain shape. When this assumption holds, the traditional physical models for the Hall-Petch effect can be used to interpret Equation 4.1. Grain boundary density has the added advantage that it can be applied to microstructures where mean grain size is inappropriate. For example, mean grain size is ambiguous in materials with a bimodal grain size or high aspect ratio grains, but the interpretation of grain boundary density remains clear.

In the case where grain boundaries are categorized as either twin or high angle, Equation 1 can be written more simply as,

$$\boldsymbol{\sigma_y = \sigma_0 + (k_1\rho_{HA} + k_2\rho_{TB})^{1/2}} \qquad \text{Equation 4.2}$$

where ρ_{HA} is the density of high angle boundaries, ρ_{TB} is the density of twin boundaries, and k_1 and k_2 is their respective strengthening coefficients. This can be rearranged in terms of a relative strengthening effect as,

$$\sigma_y = \sigma_0 + k_1^{1/2}(\rho_{HA} + m\rho_{TB})^{1/2} \qquad \text{Equation 4.3}$$

$$m = \frac{k_2}{k_1}$$

<div align="right">Equation 4.4</div>

where m is a unitless parameter that gives the relative strengthening contribution of twin boundaries as compared to high angle ones. A value of m equal to zero corresponds to twins having no strengthening effect, and $m = 1$ implies equality with other grain boundaries. Armed with a model that can incorporate a continuum of relative boundary strengths, it only remains to determine m.

Provided data for a range of ρ_{HA}, ρ_{TB} and σ_y, an estimate of m could be made by a number of methods. Bayesian regression was selected because it provides an intuitive measure of the uncertainty in the estimate of m. To linearize the regression, the term $(\rho_{GB} + m\rho_{TB})^{1/2}$ in Equation 4.3 was evaluated over a range of m values. Each value of m forms a distinct hypothesis and receives its own Bayes Factor, which were determined using the BayesFactor library of the R project for statistical computing [221, 222]. This method uses a non-informative mixture of g-priors, which mitigates the potential to introduce bias [221]. The standard interpretation is that Bayes Factor's differing by a factor of ~3 indicate 'significant' support for one hypothesis over another, while a factor of 10 is regarded as 'strong' support [223]. For easy comparison, all Bayes Factors were be normalized by the greatest one, which provides the relative likelihoods for their respective hypotheses.

Results and Discussion

Microstructures

Quantifying relative grain boundary strengthening requires microstructures whose boundary populations vary as much as possible. Otherwise, the data would be insensitive to the hypothesis and the uncertainty in the relative boundary strengths (m) would be unacceptably

large. At the same time, it is important to avoid introducing other differences in the test materials that could confound the interpretation of m. A set of materials that approximate this ideal was produced with the thermomechanical process already described. These samples were characterized with EBSD, both to quantify the grain boundary network and to account for unintended differences. The grain boundary densities were calculated from the grain boundary maps shown in Figure 4.1, where twin boundaries are colored red, and others are black (misorientation > 5˚). The materials in Figure 4.1 (a-c) all showed a similar low proportion of twin boundaries (0.22-0.31), but had a wide range of grain sizes (40-113 μm) and boundary densities (22-69 mm^{-1}). Of course, these materials alone cannot address the central question. For that, the material shown in Figure 4.1 (d) is critical. This sample had a grain size (81 μm) and boundary (32 mm^{-1}) density intermediate the other three, but had a much higher twin fraction (0.59). These parameters are listed for each microstructure in Table 4-1, with each microstructure identified by the same letter as in Figure 4.1. Each microstructure is shown again in Figure 4.2, but with the images rescaled by the mean grain size. If the microstructures were perfectly self-similar then these images would all appear alike. On the contrary, Figure 4.2 shows some subtle differences whose implications will be discussed in a later section. Determining the relative strengthening value of twins is essentially a matter fitting Equation 4.3 against the strength of these four materials.
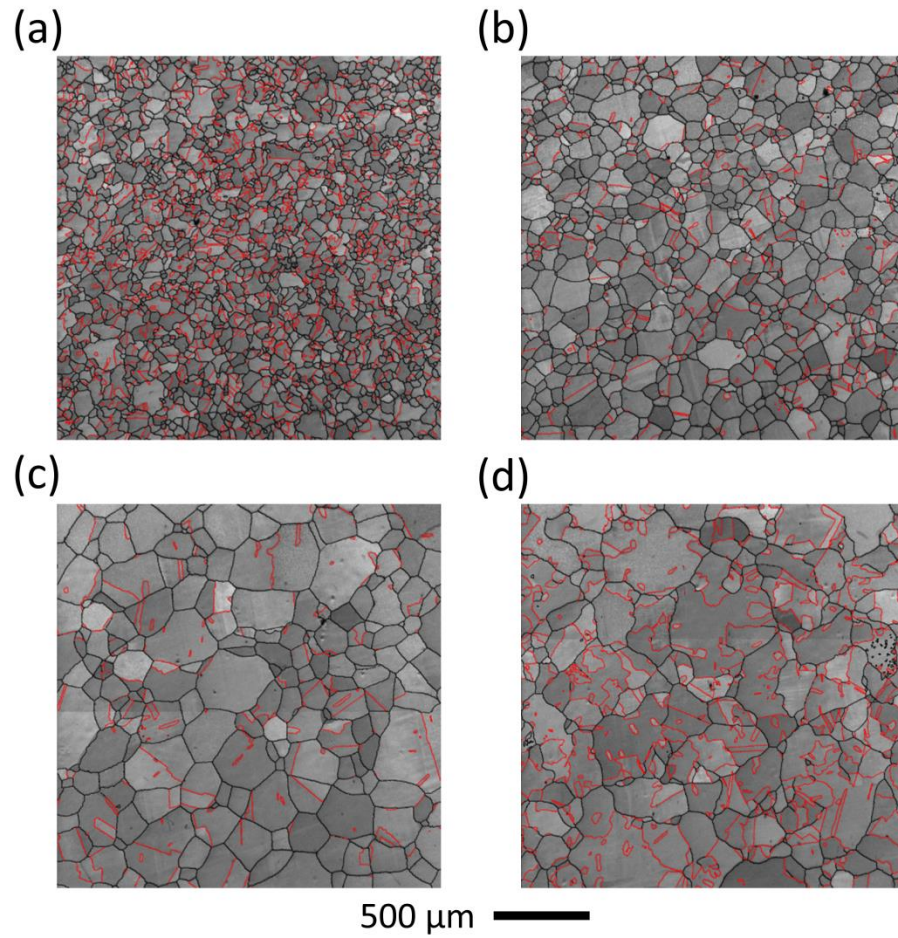
Figure 4.1: The microstructures in (a-c) show a range of grain sizes but relatively constant proportions of twin boundaries (red lines) compared to high angle boundaries (black lines). (d) shows an intermediate grain size, but with relatively more twins. These are quantified in Table 1.

(a)   (b)   177 μm   297 μm

(c)   (d)   500 μm   358 μm
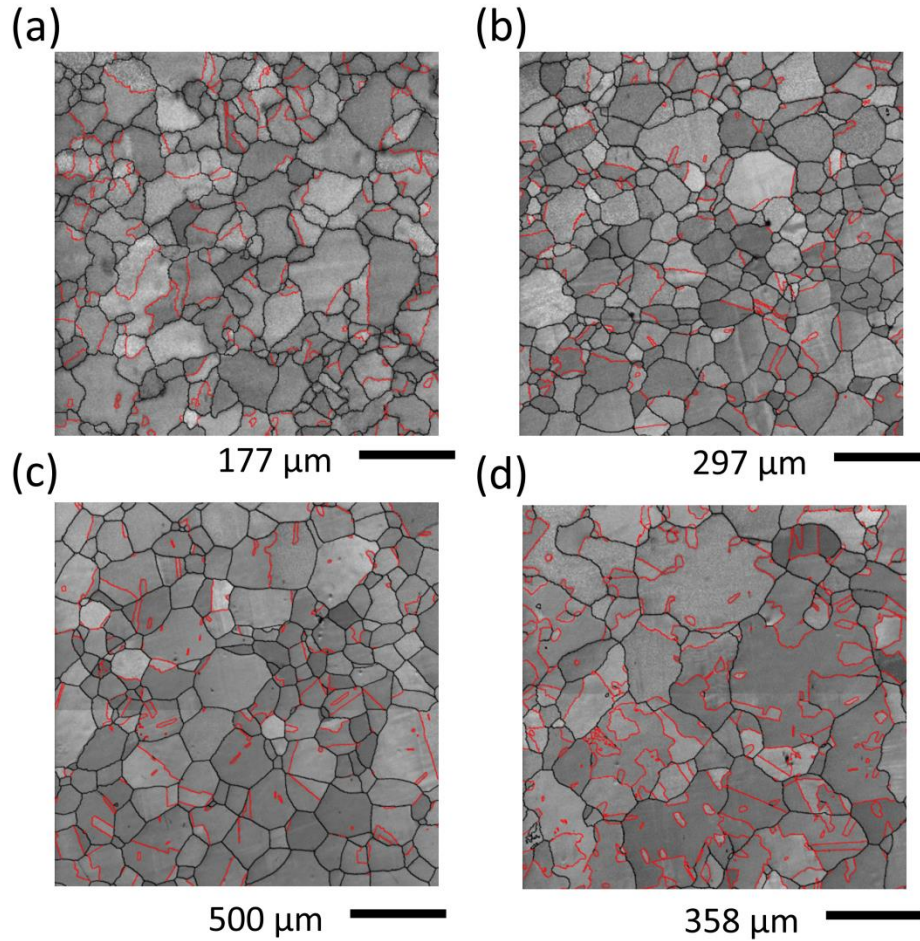
Figure 4.2: The microstructures are rescaled to show their relative self-similarity. Parts (a-d) correspond to the same materials as in parts (a-d) in Figure 4.1. Twins are shown in red and all other boundaries in black.

Table 4-1: The rolling reduction, annealing temperature and annealing time are given for each material, along with the resulting high angle and twin boundary densities, twin length fraction, grain size and grain size standard deviation. Each material is identified by the letter used to label it in Figure 4.1, Figure 4.2 and Figure 4.3.

Identifying Letter	Processing Conditions	High Angle Boundary Density (mm^{-1})	Twin Density (mm^{-1})	Twin Length Fraction	Grain Diameter (μm)	Grain Diameter Standard
(a)	25%, 800 ˚C, 15 min	47.8	21.0	0.31	40	49
(b)	25%, 800 ˚C, 2 h	29.5	8.5	0.22	67	80
(c)	25%, 800 ˚C, 6 h	15.7	6.1	0.28	113	141
(d)	5%, 900 ˚C, 15 min	13.1	18.8	0.59	81	129

86

Mechanical Properties

Yield strengths were determined with tensile tests because this geometry provides uniform strain. This is desirable because it is not currently known if the relative effect of twin boundaries on Hall-Petch behavior is constant at all strains. Figure 4.3 shows the stress-strain curves, with each one plotted from the mean of three tests. The results from individual specimens showed little scatter, and consistent elastic moduli were found. The near linearity of the region from 0.005 to 0.01 strain helped ensure a precise measure of yield strength, the values of which are listed in Table 2. These strengths were lower than for typical commercially supplied plate because the large grain sizes, see table 1. The tests were continued past the point shown, until about 5% strain, with no significant changes in trend. Of possible interest to future studies is the slightly different yielding behavior of the high twin fraction sample (black line), which seems to take a subtly different hardening path than the others. For the current interests, it is sufficient that its hardening also approached linearity well before 0.005 strain, allowing a comparable measure of its yield strength.

Table 4-2: The Taylor factor, measured yield strengths, mean yield strengths and texture-corrected strengths for each material, with the identifying letters matching those in Table 4-1.

Identifying Letter	Taylor Factor	Yield Strengths (MPa)	Mean Yield Strength (MPa)	Texture-Corrected Yield Strength (MPa)
(a)	3.00	70.0, 70.6, 70.3	70.3	72.0
(b)	3.02	67.8, 67.1, 67.2	67.4	67.8
(c)	3.02	64.2, 63.0, 62.8	63.3	63.2
(d)	3.07	64.2, 64.1, 65.4	64.6	64.4
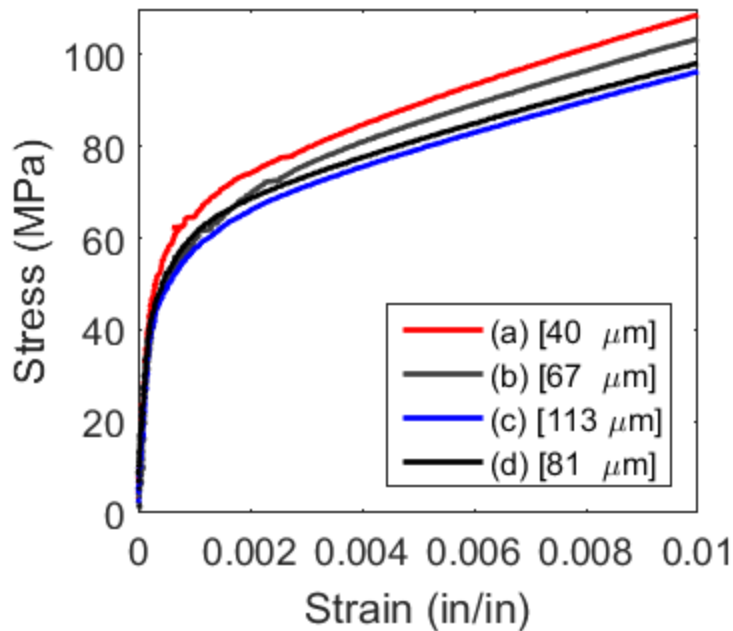
Figure 4.3: Stress-strain curves for the Ni materials, showing the elastic to plastic transition, and the linear hardening regime used to calculate yield strength. Each material is identified by the same letter used in Table 4-1, Table 4-2, Figure 4.1 and Figure 4.2. The grain sizes are listed inside brackets.

Potential Confounding Factors

Before proceeding to calculate the value of m, it is necessary to examine what sources of bias may exist. One potential source of error is the accumulated strain in the samples. Some grain boundary engineering treatments do not lead to full recrystallization, and the residual deformation hardens the material [215]. The resulting increase in hardness could easily dwarf the expected grain boundary effect. In such a material, orientation mapping would show regions of high grain orientation spread, corresponding to the unrecrystallized portions [217]. EBSD was used to check for this possibility, and the results showed that complete recrystallization had indeed occurred in every sample. These same orientation maps also show that there are differences in the grain size distribution and grain aspect ratios, which is evident from Figure 4.2. Specifically, the high special fraction microstructure shown in Figure 4.2 (d) has a broader

88

distribution of grain sizes, which is quantified by the grain size standard deviation listed in Table 1. This has the potential to introduce a bias in the data because a broadened grain size distribution can lead to a softer material [224]. Kurzydlowski and Bucki [224] have developed a grain composite model for this effect, weighting each grain's strength by its volume fraction. The strength of each grain is set equal to that of a microstructure having an equivalent uniform grain size. Unfortunately, their model is incompatible with ours because it cannot accommodate variable grain boundary properties. Furthermore, it requires that the grain boundary strengthening parameters be known, which is one of the questions being addressed. Without another model, these microstructural subtleties must be neglected, with the caution that doing so can only be justified by historical example [207, 208, 216].

A final variable that could skew the yield strengths is crystallographic texture. Texture is well known to depend on rolling reduction and to affect yield strength. It can be qualitatively assessed through pole figures, with preferred orientations being shown in multiples of random distribution. For each of the materials used, the pole figures showed a weak rolling texture, an example of which is shown in Figure 4.4. Still, the expected grain boundary effect is small and so a more quantitative analysis was desired. This was provided by the ViscoPlastic Self Consistent code (VPSC), developed by Lebensohn and Tome [37]. VPSC takes in a set of grain orientations and areas, computing the expected yield strengths by applying a user selected model. The affine model was used, which predicts strengths intermediate to the extremes given by the Taylor and Sachs models, conceptually embedding non-interacting grains in a homogenous equivalent medium. These expected yield strengths were then normalized relative to a simulated random texture, removing the effect of the model's fitting parameters. The resulting values were used to compensate for the effect of texture on the measured yield strengths. These texture-

corrected strengths are shown in Table 2. As expected from the pole figures, the impact is modest.
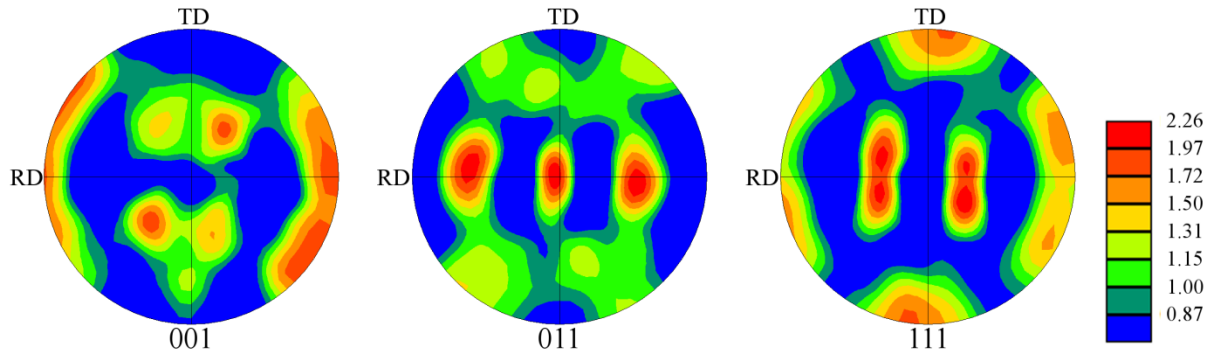
Figure 4.4: Representative pole figures showing the texture common to all the Ni samples, with the relative orientation frequency given in multiples of uniform distribution. The rolling and transverse directions are noted by RD and TD, respectively.

Twin Boundary Strengthening Coefficient

Nickel Experiments

Putting together the strength measurements and grain boundary characterization, it is possible to determine the most likely value of m, which represents the relative strengthening effect of twin boundaries in Equation 4.3. Using the Bayesian methods already described, the likelihoods for a range of m values were computed. Shown in Figure 4.5 (a), the most probable value was 0.44. The credible range of alternative values was 0.18 to 0.74, meaning that values outside that range are significantly less likely. Values below .05 or above 0.94 are 10 fold less likely than 0.44, and can be strongly rejected. When the texture-corrected strengths were used instead of the raw experimental values, the most likely value remained unchanged, but the credible range shrunk to 0.27 to 0.64. These likelihoods are plotted in Figure 4.5 (b). Values outside the range 0.16 to 0.77 can be strongly rejected. This implies that the model fits the data better after the effect of texture is accounted for with the VPSC model [37], although the conclusion was unchanged.
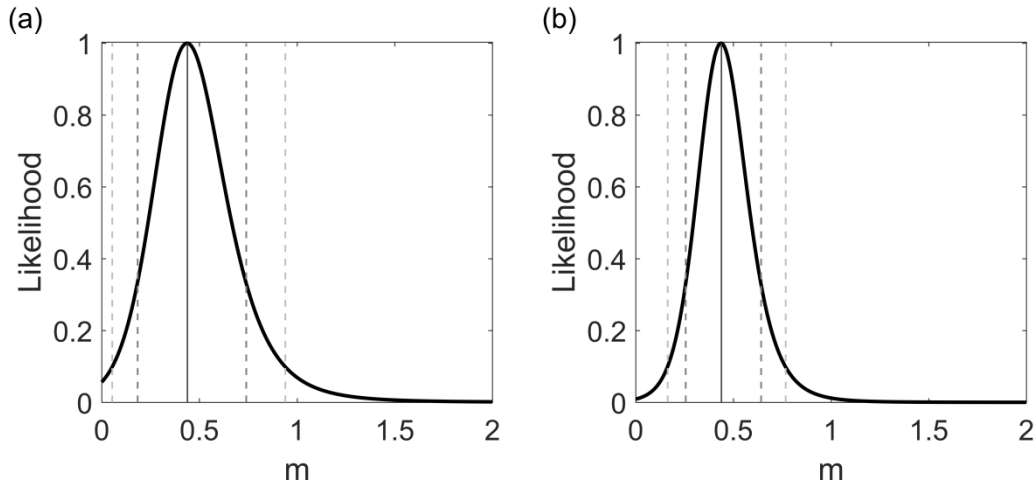
Figure 4.5: (a) The likelihoods calculated from fitting Equation 4.3 to the Ni samples' yield strength and grain boundary density under a range of m values. The solid vertical line represents the most probable value (0.44), and the dashed gray lines note the credible interval (0.18-0.74). (b) shows the same analysis compensating for effect of texture, with a most probable value of .44 and credible interval from 0.26 to 0.64.

Literature Data on Brass

These results can also be compared to the prior literature. The principal difficulty is that the grain boundary densities must be known, but are not customary included. One article to include this information is Babyak and Rhines [207], which has frequently been cited for their conclusion that, "The influence of the twin boundary upon hardness appears, within the precision of these measurements, to be quantitatively the same as that of the grain boundary." Their data set includes the hardness values of 18 brass samples covering a range of twin boundary fractions from 22% to 51%. The only information deficit is that the texture cannot be verified. Computing k_2 from this data, it was found that the most likely value was 0.20, with a maximum credible value of 0.51. This likelihood distribution is shown in Figure 4.6(a). This implies that the twins were far less potent strengtheners than the high angle boundaries
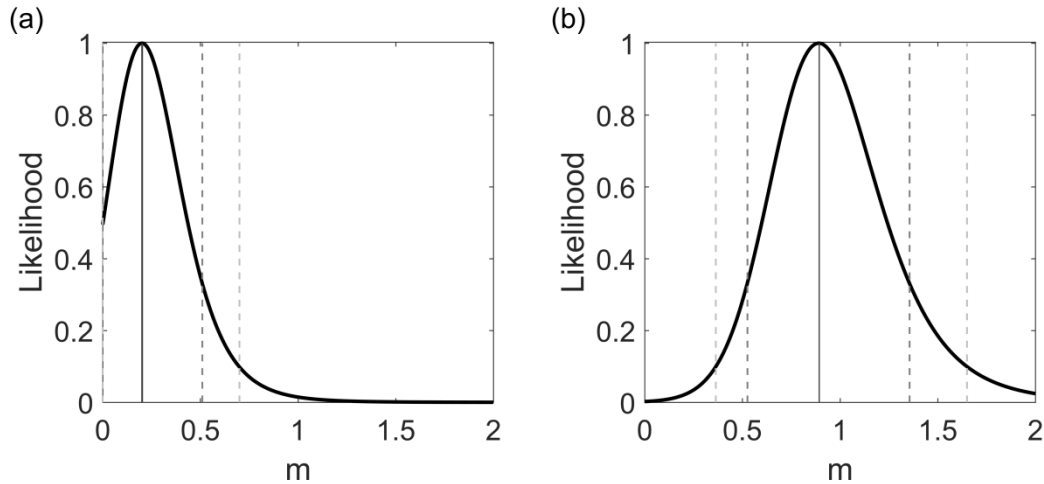
Figure 4.6: (a) The likelihoods calculated from fitting Equation 4.3 to the hardness and grain boundary density data from Babyak and Rhines [207] under a range of m values. The solid vertical line represents the most probable value (0.20), while the dashed gray line marks the upper most credible value (0.51). (b) shows the same analysis for the original model used by Babyak and Rhines [207], where the exponent in Equation 4.3 is not ½, but instead 1. The solid line is again the most probable value (0.89), and the dashed lines the credible interval (0.52-1.36).

The discrepancy with Babyak and Rhines' [207] original conclusion is because their model used a linear relationship between grain boundary density and hardness. That would be equivalent to Equation 4.3, but with the exponent of 1 instead of ½. That is inconsistent with the preponderance of experimental evidence [8], much of which has been accumulated since their original 1960 publication. Even so, doubts continue to be raised about the Hall-Petch exponent [225] and models predicting a linear relationship do exist [33, 226]. Giving the benefit of the doubt to these models, Figure 4.6(b) shows likelihoods computed for a linear fit. Like Babyak and Rhines found, the most probable value was near 1 (0.89), with a credible interval of 0.52 to 1.36. That means a linear grain boundary strengthening theory would have significant support in claiming that the effect of twins is somewhere close to that of other high angle boundaries. However, it is inappropriate to use this fit to make inferences about incompatible models, which has been common when citing Babyak and Rhines [207]. If one adopts a conventional Hall-

Petch theory, then the data suggest that twins should be regarded as contributing only about ~20% as much strength as random high angle boundaries.

Physical Interpretation

The interpretation of m, beyond being an abstract strengthening coefficient, requires an accompanying physical model. Equation 4.3 was constructed to be consistent with any Hall-Petch theory that scales with the inverse root of grain size, meaning that all the typically cited mechanisms still apply. For example, believers in the grain-boundaries-as-obstacles school could interpret this finding to mean that twins are weak barriers to dislocation transmission. That assertion would be in line with slip trace analysis [199-204] and in situ TEM imaging of dislocation-boundary interactions [200, 205], both of which have shown that twins provide little resistance to some slip systems but are strong barriers to others. This behavior also agrees with the empirical rules for slip transfer [205, 211], as well as the molecular dynamics results and line-tension model from de Koning et al. [227]. These last two theories also provide a way to reconcile the strengthening effect of twins with the Ashby hardening model. The possibility of easy slip transfer between some twins could make it possible to satisfy compatibility constraints with a lower overall GND density. Indeed, this was inferred by Kashihara and Inoko [201] from the deformation and recrystallization of twinned bicrystals. To be consistent with a grain boundary source model, our results imply that twin boundaries must be poor dislocation sources. That argument is consistent with molecular dynamics results that suggest coherent twin boundaries require high stresses to nucleate dislocations, roughly equivalent to the crystal interior. Of course, real twin boundaries contain incoherent steps, and they can act as dislocation sources [214, 228]. In short, the general concept of each theory is consistent with the observed strengthening effect of twins.

93

Conclusions

A minor revision to the Hall-Petch equation significantly expands its power to make predictions based on the relative strengthening effect of different grain boundary types. The form of this modification owes much to the work of Pande et al. [210], Hansen [220], and Babyak and Rhines [207]. Despite a caveat regarding grain size distribution, the data suggests twins have an appreciable contribution to strength, somewhere from half to one quarter that of other grain boundaries. This provides a way to understand the strength of several interesting materials with high twin fractions [59, 182]. The physical interpretation of this result depends on the Hall-Petch mechanism that one believes in. This could provide a way to select the best Hall-Petch model, but more quantitative predictions are needed.

Chapter 5 - Nanocrystalline Grain Boundary Engineering: Increasing Σ3 Boundary Fraction in Pure Ni with Thermomechanical Treatments

Abstract

Grain boundary networks should play a dominant role in determining the mechanical properties of nanocrystalline metals. However, these networks are difficult to characterize and their response to deformation is incompletely understood. In this work, we study the grain boundary network of nanocrystalline Ni and explore whether it can be modified by plastic deformation. Mechanical cycling at room temperature did not lead to structural evolution, but elevated temperature cycling did alter the grain boundary network. In addition to mechanically-driven grain growth, mechanical cycling at 100 °C led to a 48% increase in Σ3 boundaries, determined with transmission Kikuchi diffraction. The extent of boundary modification was a function of the number of applied loading cycles and the testing temperature, with more cycles at higher temperatures leading to more special grain boundaries. The results presented here suggest a path to grain boundary engineering in nanocrystalline materials.

Introduction

Nanocrystalline metals are promising next-generation structural materials with high strength, fatigue life and wear resistance [113, 229, 230]. Their enhanced properties can be attributed to the high density of grain boundaries, which is usually quantified indirectly by grain size. Indeed, grain size has been the fundamental metric used for the creation of nanocrystalline structure-property scaling laws to this point [17]. However, recent studies have highlighted the importance of also considering boundary type and topological arrangement [118, 152, 156]. Nanotwinned Cu, which contains grains subdivided into nanoscale twin domains, is perhaps the most notable example. This material shares the enormous strength of nanocrystalline copper but

remains ductile because twins replace random boundaries as the dominant network component, providing soft and hard directions for dislocation movement [118, 119]. In essence, the properties are improved by substituting a favorable boundary type (twin) for an unfavorable one (random).

Atomistic modeling studies suggest that changes to the grain boundary network can alter mechanical behavior. Rupert and Schuh [231] observed that subtle boundary relaxation, either through annealing or mechanical cycling, could increase the strength of a simulated nanocrystalline metal. Since catastrophic strain localization can occur if a high strain path percolates across a nanocrystalline specimen [232], ductility should also be intimately connected to features of the boundary network. Hasnaoui et al. [152] used molecular dynamics to show that shear strain can concentrate in the random boundaries, which resist sliding less strongly than low angle boundaries. Experimental studies support these observations, with boundary relaxation found to increase strength but also promote shear localization [233, 234]. In addition to mechanical properties, it has become evident that grain boundary network characteristics are closely tied to the thermal stability of nanostructured materials. Lagrange et al. [156] showed that a few highly mobile boundary segments can cause coarsening in an otherwise stable network. Clearly, the exact character and arrangement of grain boundaries is critical to the performance of nanostructured metals, providing motivation to study and control nanocrystalline grain boundary networks.

Tuning grain boundary networks is accomplished in coarse grained alloys through grain boundary engineering treatments [115]. Most commonly, this consists of repeated thermomechanical processing to maximize the number and connectivity of boundaries which are considered "special" [115]. Several analytical tools exist to classify grain boundaries and characterize a boundary network. Most GB engineering investigators apply the coincident site

lattice (CSL) model, which is based on the maximum theoretical periodicity of shared lattice sites [49]. The CSL values (Σ) can be approximately correlated with boundary energy [49]. Boundaries with Σ value less than 29 are considered special because of their low energy. Low angle ($\Sigma 1$) and twin ($\Sigma 3$) boundaries are often singled out for specific consideration because of their unique properties [115]. Triple junctions can be categorized according to the number of special ($\Sigma 1$-29) boundaries which they join. Network connectivity, which controls many intergranular phenomena, has been evaluated with both percolation theories and triple junction distributions [89, 160]. More recently, network topology has been quantified with the cluster mass approach, which is based on the length of interconnected boundary segments sharing a common type [81].

Typical GB engineering treatments are of two types, often called strain annealing and strain recrystallization [100]. In strain annealing, the metal is deformed 6-8% and then heated below the recrystallization temperature for several hours, with the whole process repeated several times [235, 236]. Unfortunately, the long annealing times cause significant grain growth and increase processing costs [100]. Alternatively, in strain recrystallization, the sample is deformed 5-30% and then heated to a high temperature for a short time, with these steps being iterated as needed [237]. In strain recrystallization, the level of strain energy is insufficient to cause complete recrystallization upon heating, instead causing boundary decomposition [100]. When this occurs, a boundary is split into new segments by the nucleation of a grain [100]. A higher energy boundary will tend to decompose into multiple lower energy segments, reducing the total system energy [100]. Inhomogeneous strain energy density causes the nucleated grain to expand into its neighbors, elongating the new low energy boundary segments [100]. When

97

repeated, this produces a fine-grained microstructure in which special boundaries are well incorporated into the network [100].

Traditional mechanisms should not operate in nanocrystalline systems, primarily because these materials cannot store the dislocation networks required to drive boundary decomposition. The lack of dislocation storage in nanocrystalline metals has been shown by in situ X-ray diffraction experiments, transmission electron microscopy (TEM) investigations, and atomistic simulations [26, 31, 238]. Fortunately, nanocrystalline metals deform through collective processes, which may supply a replacement mechanism for grain boundary network evolution. At grain sizes below ~100 nm, dislocations are emitted from grain boundaries and absorbed at interfaces on the other side of the grain [229]. While the traditional view of a dislocation is that it brings a small increment of plasticity, a single dislocation moving through a 15 nm grain in Al can cause a shear strain of ~2%, enough to change the grain shape [239, 240]. Such deformation should also require accommodation from surrounding grains to maintain compatibility at the interfaces. Grain rotation and sliding are the predominant carriers of plastic strain for grain sizes below ~20 nm [241, 242]. The underlying physical processes behind such mechanisms are atomic shuffling events at the boundary, which some authors have likened to the shear transformation zones in metallic glasses [26, 243, 244]. A priori, grain rotation must alter the local grain boundary character since the misorientation of the interface is changing. The possibility of longer range boundary modification is suggested by observations of textured nanocrystalline clusters formed by stress driven rotation [30]. The high stresses accessible in nanocrystalline materials can also lead to grain boundary migration, causing grain growth, softening, and increased ductility [28, 245, 246]. The common feature of these phenomena is

that they may directly modify the boundary network, providing the potential to controllably modify nanocrystalline grain boundary networks.

Until recently, the study of nanocrystalline grain boundary network reorganization was impossible due to the limitations of characterization tools. Electron backscatter diffraction (EBSD), the standard tool for studying coarse-grained networks, lacks sufficient resolution to characterize nanocrystalline materials. Two new techniques have been developed which relieve this difficulty, namely TEM based automated crystal orientation mapping (TEM-ACOM) and scanning electron microscope (SEM) based transmission Kikuchi diffraction (TKD) [44, 136]. TEM-ACOM uses precession enhanced convergent beam electron diffraction and pattern matching to enable orientation mapping with ~2 nm resolution [136]. A limitation of this technique for studying nanocrystalline materials is that diffraction patterns are generated for every grain the beam passes through. If there are overlapping grains, the resulting signals may be impossible to deconvolve [136]. This places a very strict limit on sample thickness and may pose challenges for specimen preparation. TKD uses Kikuchi patterns cast on an EBSD detector by electrons forescattered through a thin specimen [44]. The low interaction volume enables resolution down to ~3 nm, although this is dependent on atomic number [44]. The Kikuchi pattern is generated from only the lowest surface of the sample and thickness limits are significantly relaxed [42]. This technique also has the major advantage of being implementable on a standard EBSD equipped field emission SEM.

With new characterization techniques and an improved understanding of nanocrystalline deformation physics, the tools are now available for a study of nanocrystalline interfacial networks and their evolution under stress. In this study, we explore methods to directly modify the grain boundary network of nanocrystalline Ni, using combinations of applied stress and

99

elevated temperature. Room temperature mechanical cycling was found to be ineffective, leaving the grain structure and boundary network unchanged. However, cycling at elevated temperature did induce evolution of the grain boundary network. Grain boundary network evolution was most obviously observed as an increase in the $\Sigma 3$ boundary fraction. The effects of stress-free annealing and of creep were separately investigated to provide controls with which to compare the other treatments, showing that high stress and plastic deformation are needed for microstructural evolution. The most likely mechanism is believed to be collective deformation, although our results focus on statistical boundary metrics rather than micromechanisms.

Materials and methods

Nickel was selected for these experiments because its high stacking fault energy makes it challenging to grain boundary engineer by traditional means [96]. Nanocrystalline Ni was deposited onto Si wafers from a 99.999% pure Ni target using radio frequency magnetron sputtering for a final thickness of 260±9 nm (Ulvac JSP 8000). All of the material used for this work was deposited in a single batch to ensure a uniform as-deposited condition. The supporting Si was micromachined to produce a rigid frame around a free-standing Ni membrane, with dimensions of 2.5 by 10 mm. The fabrication process generally followed Vlassak et al., with deep reactive ion and XeF_2 etching replacing KOH and reactive ion etching, respectively [247].

The thin films were mechanically loaded with bulge testing, where a gas pressure deforms a diaphragm-like sample [248]. The test is convenient for thin film materials because the specimen and supporting window are co-fabricated, which eliminates sample handling and gripping issues [247]. It is also less cumbersome than microtensile or microcompression tests, especially when testing at elevated temperatures, while still delivering full stress-strain

measurements. A custom bulge test apparatus, which is capable of performing controlled thermomechanical cycling at temperatures up to 500 °C, was constructed. The device was similar to that of Kalkman et al. [249] , except that deflection was measured with a standard laser triangulation sensor (Micro-Epsilon optoNCDT 1700).

Bulge testing produces a biaxial stress, much like in the thin wall of a cylindrical pressure vessel [247]. For long rectangular specimens, the hoop stress and strain are constant across the sample, allowing for the uniform onset of plasticity within the film [250]. The hoop strain (ε_1) is given by:

$$\varepsilon_1 = \varepsilon_0 + \frac{a^2 + h^2}{2ah} arcsin\left(\frac{2ah}{a^2 + h^2}\right) - 1 \qquad \text{Equation 5.1}$$

where p is the applied pressure, a is ½ the membrane width, ε_0 is the residual strain and h is the maximum bulge height [250]. The hoop stress (σ_1) is given by:

$$\sigma_1 = \frac{p(a^2+h^2)}{2ah} \qquad \text{Equation 5.2}$$

Many authors who employ bulge testing combine this hoop stress with the smaller longitudinal stress component to calculate a von Mises equivalent stress. However, at elevated temperatures, some of our films become slack before testing. While they become taut in the hoop direction as soon as a small pressure is applied, making Eqns. (1) and (2) valid as long as the initial height is properly considered [251], the films take longer to become taut in the longitudinal direction. To remain consistent, we only report hoop stresses and strains in this study. While this can affect measurements of mechanical properties such as strength, calculating these properties is not our primary goal. Rather, repeatable mechanical cycling is our aim.

The bulge tests were controlled by setting the pressure as a function of time. According to Eqn. (2), the stress cannot be controlled without knowledge the bulge height. Rather than implement a complex feedback system, the peak cycling pressure was selected from our

monotonic tests on identical samples. If the peak deflection remains nearly constant, then this method will produce cycles with roughly constant stress amplitude, approximating stress-controlled cycling. In the case of accumulated plastic strain, the peak stress will drop as the peak bulge height increases. The applied pressure was varied slowly, at a cycling rate of 4 mHz, producing an average strain rate on the order of 10^{-6} s^{-1}.

Specimens were prepared for TKD and plan view TEM by thinning at cryogenic temperatures in a low angle Ar ion mill (Fischione 1010) at 2-3 kV and 5 mA. Immediately prior to TKD analysis, the samples were cleaned in a 10 W oxygen plasma for 5 minutes (South Bay Technologies PC2000). Cross-sectional TEM specimens were prepared using the focused ion beam (FIB) in situ lift-out technique in a Quanta 3D field emission gun (FEG) dual beam microscope. A voltage of 5 kV was used during the final thinning step to minimize the thickness of the damaged layer created by the FIB. Bright field TEM images were collected with an FEI/Philips CM-20 instrument operated at 200 kV. TKD was performed with an FEI Quanta3D equipped with an Oxford Instruments Nordlys F+ EBSD detector, operated at 30 kV and 11 nA with a 1 mm aperture and a 3.5 mm working distance. These parameters were selected using the information published by Keller and Geiss [44], and Trimby and coworkers [45, 252]. A custom holder was used to align the sample at a 20° tilt to the beam axis, as in Keller and Geiss's geometry [44]. A step size of 2-6 nm was selected based on the grain size. Maps were kept small to minimize drift, usually from 5000-24000 nm^2. A representative example of the as-collected TKD maps is shown in Figure 5.1(a).
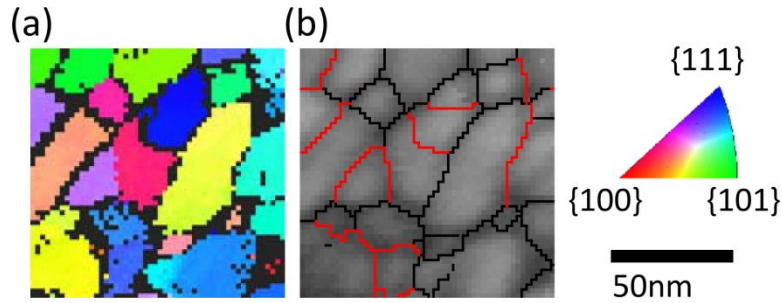
Figure 5.1: (a) Raw orientation map before any post-processing. The color scheme follows the inverse pole figure legend and non-indexed pixels are colored black. (b) Reconstructed grain boundaries have been overlaid on the patter quality map. Black lines represent random boundaries, while red are Σ1-29 boundaries. Lighter shades of grey in the grain interiors indicate higher quality diffraction patterns.

Orientation data was processed and standard noise reduction techniques were applied [39, 253] using the Channel5 software package (Oxford Instruments). A 2° critical misorientation angle was used to reconstruct grain boundaries and the Brandon criterion was then applied to categorized them into CSL types [50], as shown in Figure 5.1(b). Each boundary segment was classified as either random high angle or special ($\Sigma \leq 29$). Of the special boundaries, extra attention was given to the low angle ($\Sigma 1$), twin ($\Sigma 3$), and twin variant ($\Sigma 9$, $\Sigma 27$) types. These types were selected because they can be correlated with boundary energy and are commonly reported in traditional GB engineering research. Grain boundary statistics are reported according to length fraction because this measure is less sensitive to short, erroneously indexed boundaries [78]. Triple junction types were identified using code written in MATLAB (MathWorks). The grain size was calculated from the reconstructed grain areas, as recommended by ASTM E2627 [254]. The ASTM E2627 provision to discard grains with fewer than 100 indexed points was impractically restrictive, and was lowered to a threshold of 4 points [254].

Results and Discussion

As-Deposited Microstructure

Bright field TEM images of the as-deposited microstructure are shown in Figure 5.2. The plan view image in Figure 5.2(a) shows uniformly nanocrystalline and equiaxed grains, having a mean size of 23 nm. There are no abnormally large grains and the grain size distribution appears narrow. Material with a small grain size was desired to maximize the potential for grain boundary network reorganization through collective deformation physics. Vo et al. [255] showed that the amount of plastic strain which could be attributed to grain rotation is inversely related to grain size, theoretically increasing the overall network modification with decreasing grain size. Below grain sizes of ~10 nm, grain boundary sliding and rotation can become so dominant as to cause an inverse Hall-Petch effect [21]. A lower limit on the practical grain size was imposed by the resolution of TKD, which could only reliably detect grains larger than 5 nm. As such, a 23 nm mean grain size provided a good compromise between small grain size and TKD data quality. TKD measurement gave an average grain size of 22 nm, providing excellent agreement with the TEM results. All figures in this paper which quote grain size are referring to measurements taken from TKD.

A cross-sectional TEM micrograph of an as-deposited film is presented in Figure 5.2(b), showing only modest grain elongation in the film normal direction (ND). Many boundaries are perpendicular to the deposition direction, making this structure distinct from the columnar morphology sometimes found in sputtered films. An equiaxed grain structure is desirable for this study because it should mimic the response of a truly bulk nanocrystalline material. Free surface effects on stress-driven grain boundary migration are generally limited to a region within a distance of about one grain diameter from the surface [256]. In our samples, the presence of many grains through the film thickness limits the importance of any free surface effects.
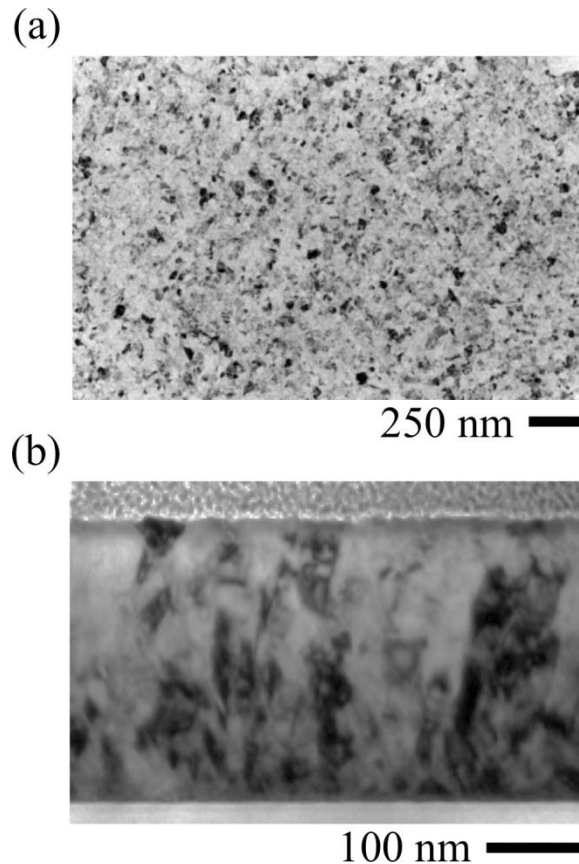
Figure 5.2: Bright field TEM images of the as-deposited microstructure in (a) plan view and (b) cross sectional view.

The as-deposited film texture is represented by the pole figures shown in Figure 5.3, which demonstrates a slight texture in the film's growth direction. Of the total material, 34±6% was oriented within 15° of the ideal <111> normal direction fiber (<111>//ND). This fiber texture is common to many sputtered films [257, 258]. In general, fiber textures will increase the fraction of CSL boundaries which share the same misorientation axis [259]. For a <111> fiber texture, an increased fraction of Σ 1, 3, 7, 13b, 19b and 21a boundaries would be expected [259]. We observed no measurable change in film texture after any combination of mechanical cycling or annealing.
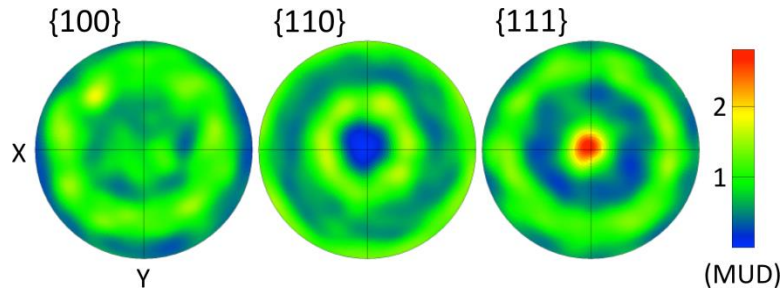
Figure 5.3: Pole figure showing the texture of the as-deposited films. The color scale is in multiples of uniform distribution (MUD). Neither annealing nor mechanical cycling changed the texture.

Room Temperature Mechanical Cycling

Samples were first deformed at room temperature to investigate our hypothesis that grain boundary mediated plastic deformation can alter the boundary network. In addition to monotonic loading to failure, a cyclic loading pattern was also used because it is expected to cause greater microstructural changes. Stress induced grain coarsening, one obvious form of boundary evolution, has been observed in several studies of nanocrystalline Ni deformed at room temperature. The magnitude of coarsening averaged ~600% higher in those studies that applied cyclic loads [113, 260-267], although it is impossible to control for differences such as sample purity and loading type. Molecular dynamics work has also linked cyclic stress to grain boundary evolution, showing a reduction in local structural disorder with increasing number of cycles [231]. Figure 5.4(a) shows the hoop stress-strain curves for films loaded both monotonically and cyclically. The nanocrystalline films demonstrate the high strength and low ductility characteristic of most nanocrystalline metals. A high peak cyclic stress of 1.2 GPa was selected to maximize the potential for stress driven grain boundary migration and grain rotation. The modulus was measured to be 150 GPa, and did not vary significantly between loading and unloading or with extended cycling. The brittle nature of the films did not allow a yield strength to be determined. Despite the lack of a clear yield point, plastic strain accumulated over the course of several cycles, eventually reaching a maximum of 0.35%. Isolation of the 1st, 5th,

25th and 125th cycles (presented in Figure 5.4(b)) shows that the initial hysteresis quickly disappears, indicating that any microstructural change is concentrated in the first few cycles. The gradual drop in peak stress with increased cycling is caused by the open-loop pressure controlled test procedure, as previously discussed.

Figure 5.4: Hoop stress-strain plots show the mechanical behavior of nanocrystalline nickel tested at room temperature. Part (a) shows the monotonic and full cyclic behavior, while Part (b) isolates the monotonic, 1st, 5th, 25th and 125th cycles.

Since grain coarsening is an obvious sign of structural evolution, we begin by looking at the grain size distributions. Figure 5.5(a) shows that the as-deposited, monotonically loaded, and cyclically loaded materials have identical mean grain size and distribution. No grain coarsening occurred, unlike some other reports on fatigue loaded nanocrystalline Ni [113]. Possible subtle changes to the grain boundary network were assessed by analyzing TKD orientation maps. The grain boundary character distribution (GBCD), which tracks CSL fractions, is shown in Figure 5.5(b). All error bars in this work represent a 95% binomial proportion confidence interval and were calculated using the Normal Approximation Method. Neither monotonic nor cyclic loading caused any change in the GBCD. Together, the unchanged grain size and GBCD indicate that no significant boundary network change was driven by mechanical cycling at room temperature.

This may be due to the limited plasticity; all of the literature motivating our hypothesis involved significantly more plasticity than was achieved in this case.
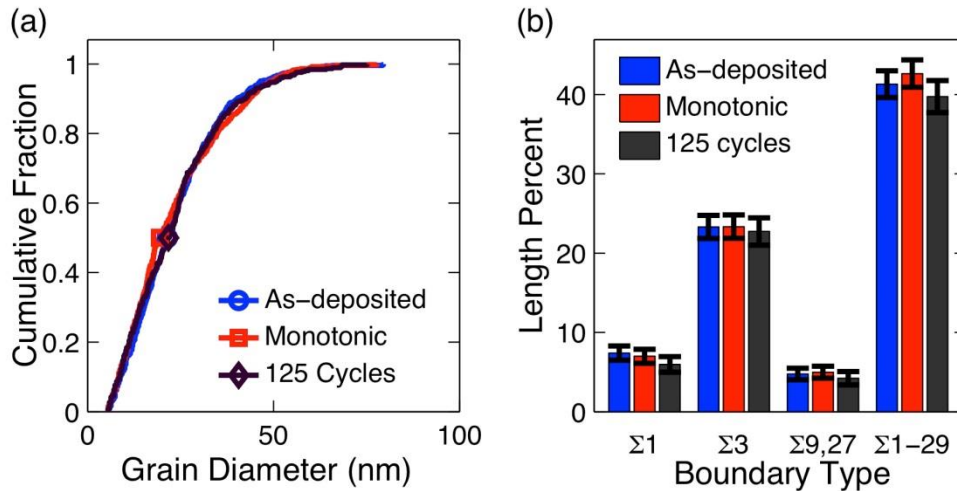
Figure 5.5: Mechanical loading at room temperature had no effect on either (a) the cumulative grain size distribution or (b) the grain boundary character distribution.

Warm Mechanical Cycling

Analytical models indicate that the amount of grain rotation should increase with increasing temperature, following an Arrhenius trend. Cahn and Taylor described rotation as the combined result of coupled grain boundary motion and sliding [29]. In the case of only coupled grain boundary motion, the overall extent of rotation will be directly tied to boundary mobility, until very high temperatures when the coupling breaks down [29, 268]. The contribution of grain boundary sliding to grain rotation has been isolated and modeled by Moldovan [269], who followed Raj and Ashby's [270] work. They showed that the sliding rate depends on the lattice and grain boundary diffusivities, which, like boundary mobility, follow an Arrhenius relation. Harris et al. [271] reached an identical conclusion using an analysis built on Ashby and Verrall's work [272]. Atomistic simulations by Panzarino et al. [195] agree with these analytical models, showing that stress driven grain rotation is enhanced at high temperature. Experimental work

has also shown that elevated temperature can promote stress driven nanocrystalline grain growth [273, 274].

Therefore, to encourage plasticity and concomitant structural evolution, the testing temperature was increased. For this study, the ideal temperature would allow for significant boundary mobility without causing thermal grain growth. Films were annealed at 100, 150, and 250 ˚C to gain a better understanding of the effect of temperature on thermal grain growth. At 150 and 250 ˚C, abnormal grain growth consumed most of the nanocrystalline material. At 100 ˚C, a modest level of limited abnormal grain growth occurred, but most of the material remained nanocrystalline. This seemed to provide the best balance between boundary mobility and grain size stability.

The stress strain results for mechanical testing at 100 ˚C are shown in Figure 5.6(a), where the monotonic behavior and cyclic response are both shown. For clarity, the 1st, 5th, 10th and 50th cycles have also been plotted separately in Figure 5.6(b). The peak stress amplitude was reduced to 900 MPa to avoid rupturing the sample. Elevated temperature reduced the modulus to 110 GPa and increased the total plastic strain to nearly 1%. It is apparent that the plastic strain accumulated exceeds that observed during room temperature cycling. The mid-loop hysteresis and incremental increase in plastic deformation decreased with increasing cycle number. Taken together, the cycling behavior indicates more potential for microstructural change than was seen at room temperature, despite the lower peak stress.
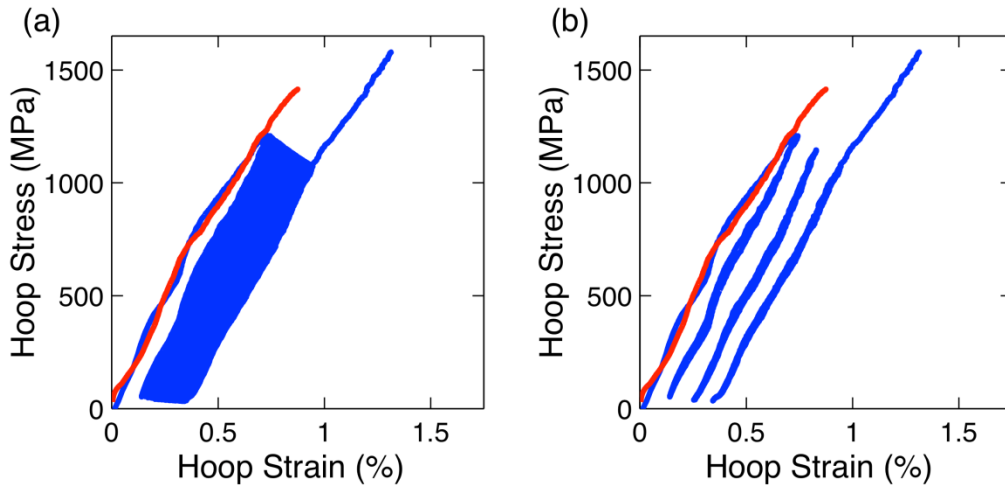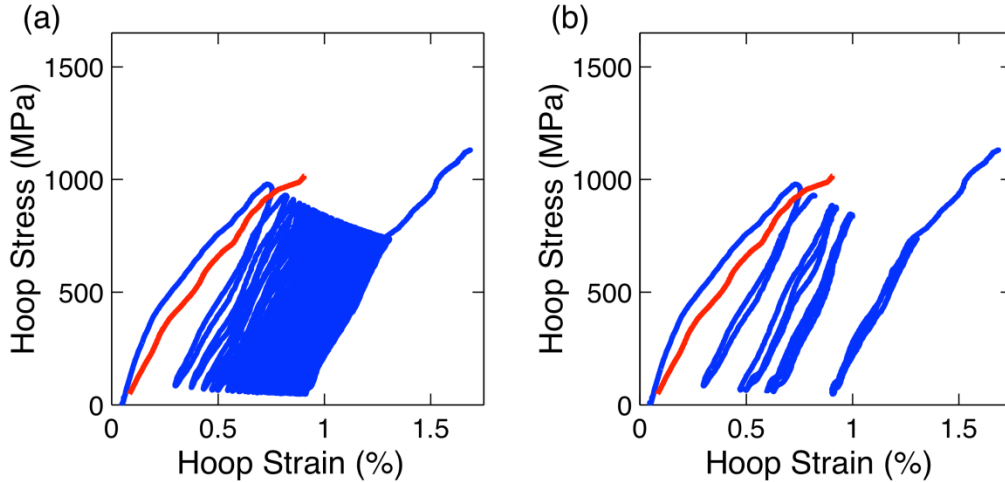
Figure 5.6: Stress strain plots show the mechanical behavior of nanocrystalline nickel tested at 100 ° C. Part (a) shows the monotonic and full cyclic behavior, while Part (b) isolates the monotonic, 1st, 5th, 10th and 50th cycles.

The top row of Figure 5.7(a) presents TEM images from samples that were mechanically cycled at 100 °C, showing that cycling was accompanied by grain growth. The extent of microstructural change qualitatively correlates with the number of loading cycles. To isolate the effect of cyclic plasticity, a series of stress-free annealing experiments was also performed. In Figure 5.7, each image of cycled material is above an image of material which was annealed stress-free for a time matching the duration of the cycling experiment. The annealed specimens show much less structural evolution, indicating that cyclic plasticity is of prime importance. The bottom row of Figure 5.7 also shows that annealing at 100 °C can cause a few large grains to form. This abnormal grain growth is expected for pure nanocrystalline metals and is a mechanism for reducing excess boundary energy [275, 276]. To preserve this study's focus on nanocrystalline phenomena, the abnormally grown grains were excluded from the TKD analysis. Ideally, this would have been done by collecting very large maps and then post-process sorting by grain size. Unfortunately, drift required that maps be so small that they could not encompass the larger grains, which would have made post-process sorting ambiguous. It was instead

decided to exclude the large grains prior to orientation mapping by selecting nanocrystalline regions based on the forescatter image.
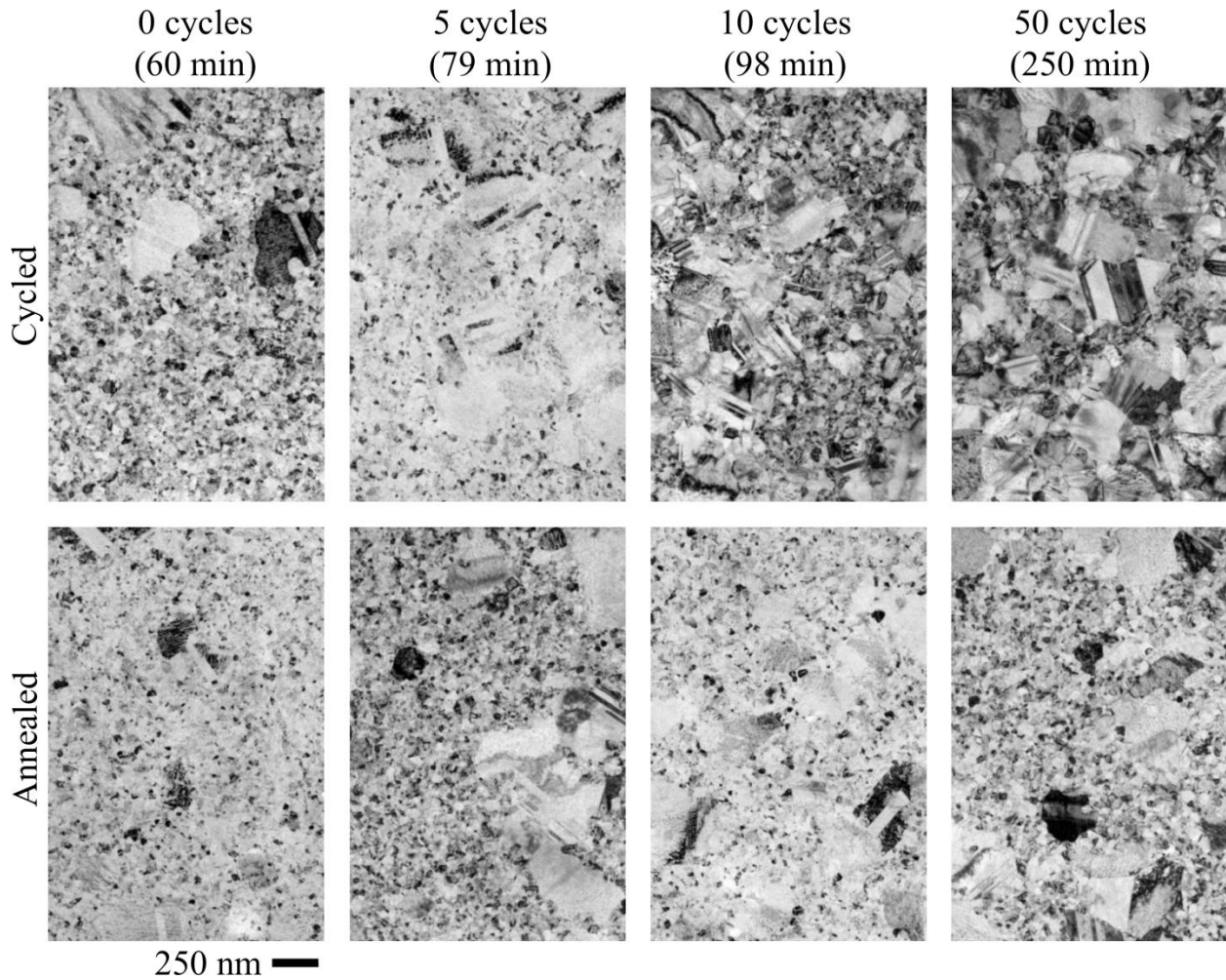
Figure 5.7: The bright field TEM images in the upper row show films which were mechanically cycled at 100 °C, while those in the lower row were annealed stress-free at 100 °C for equivalent times.

Grain size distributions are presented in Figure 5.8 for both the stress-free and mechanical cycling treatments at 100 °C. For stress-free annealing, the grain size distribution remains unchanged through 100 min. A small increase in grain size is observed after annealing for 250 min. On the other hand, mechanical cycling caused significant changes to the grain size distribution. Fifty loading cycles increased the average grain size to 51 nm, up from a starting value of only 22 nm, and the entire grain size distribution shifts toward the largest values. After

111

50 cycles, the microstructural evolution was so extensive that it became slightly more difficult to identify and exclude the abnormally grown grains using only the forescatter image. This reduces our certainty that the 50 cycle data is entirely free from the influence of larger grains. In any case, the trend for increasing grain size with mechanical cycling remains obvious. Similar grain growth caused by repeated mechanical stress has previously been observed in several studies, as mentioned previously [113, 260-267]. The observed coarsening could be caused by stress driven boundary migration or rotation induced coalescence [277, 278].
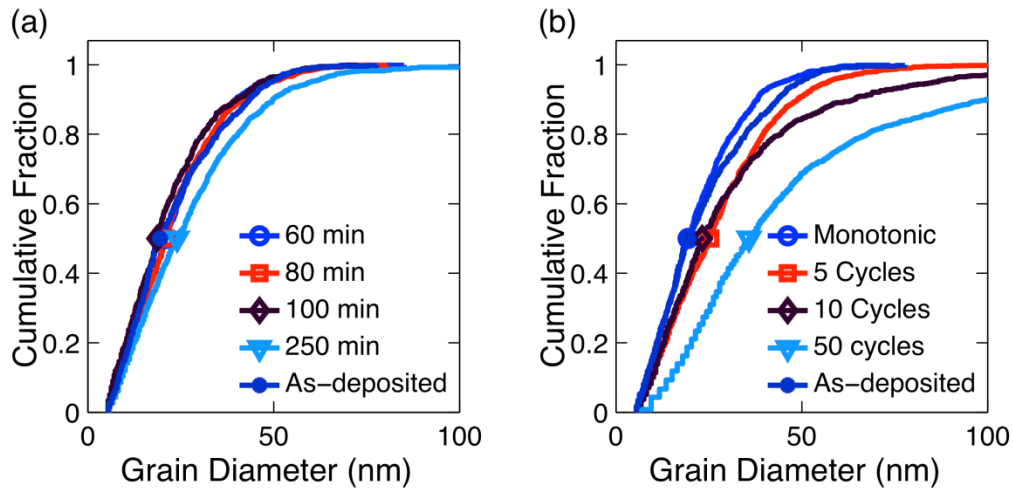
Figure 5.8: (a) Stress-free annealing at 100 °C only causes subtle grain growth, while (b) mechanical cycling at 100 °C affects the cumulative grain size distribution in a much more pronounced manner.

The coarsening trend indicates grain boundary rearrangement, the nature of which was investigated with TKD orientation mapping. Four types of grain boundaries are quantified in Figure 5.9, as a function of applied mechanical cycle. Data from the stress-free annealing control experiments is also included to provide a baseline. The largest change in the grain boundary character distribution was an increase in $\Sigma 3$ fraction, shown in Figure 5.9(b). The small change after 1 and 5 cycles was followed by increases of 30% after 10 cycles and 48% after 50 cycles. In each case, the change is quantified relative to the starting material. The trend

of increasing Σ3 fraction with increased cycling is further evidence that grain boundary rearrangement is driven by the repeated deformation. The Σ3 length fraction remains constant during the stress-free annealing.
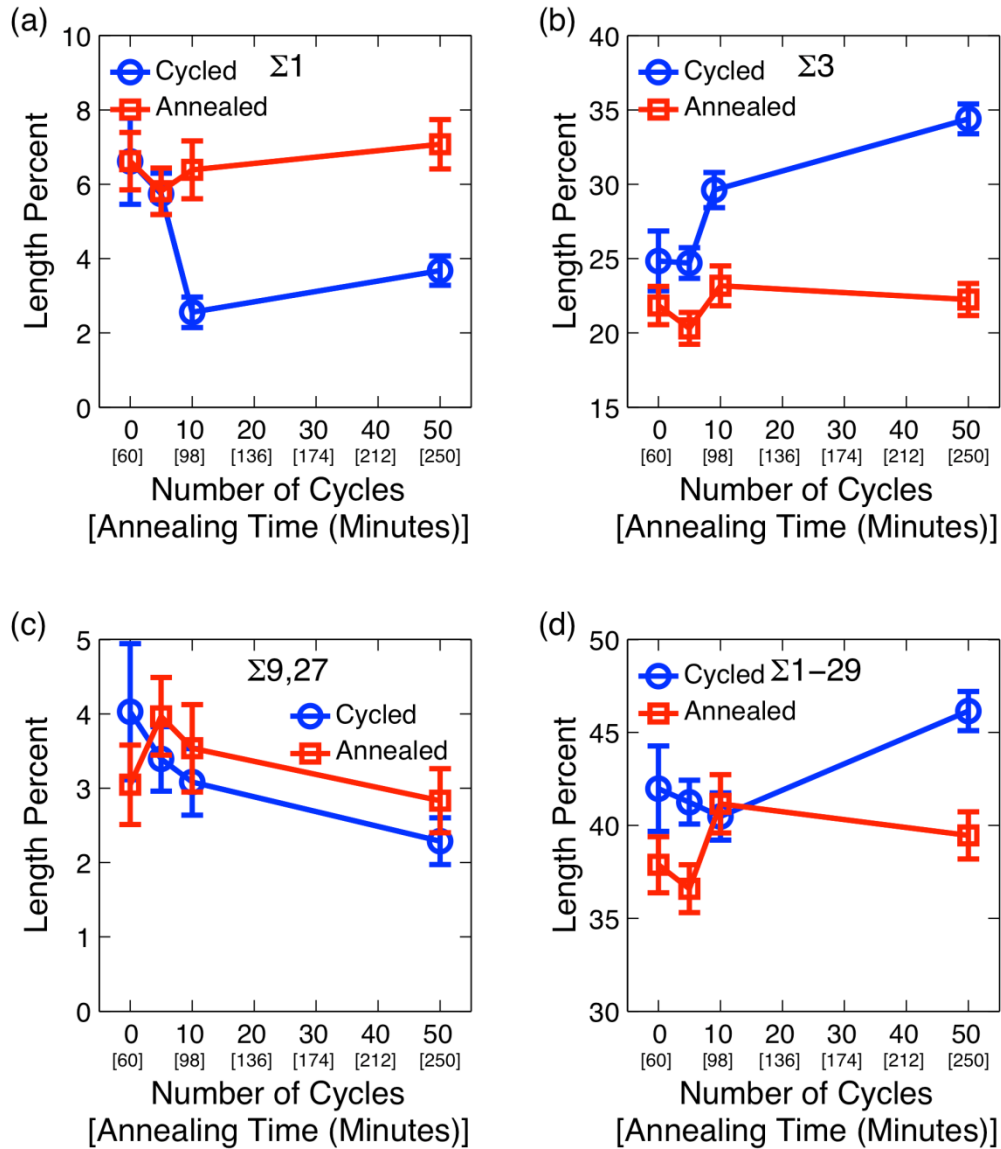
Figure 5.9: The length fractions of (a) Σ1, (b) Σ3, (c) Σ9,27 and (d) Σ1-29 boundaries after stress-free annealing and mechanical cycling at 100 °C. The material was either annealed (red squares) or mechanically cycled at 100 °C (blue circles).

There are currently very few reports which statistically quantify the grain boundary network of nanocrystalline materials because the required microscopy techniques are so new. In

one such work, Brons and Thompson [279] have reported the grain boundary character distribution for a sputtered Ni film created under slightly different processing conditions. For an initial grain size of 37 nm and strong <101>//ND texture, these authors found a Σ3 length fraction of only 5.2% [279]. The Σ3 length fraction increased to a maximum of 9.2% after annealing at 450 °C, which also caused substantial coarsening. In comparison to these results, the 34.4% Σ3 fraction which we observe here appears to be quite high. The difference in film texture may contribute to the difference between the results of Brons and Thompson and our own.

Kobler et al. [280] found that deformation could either increase or decrease the number of twins per grain in nanocrystalline Pd. They found that twin density fell in samples with a large initial concentration of twins, while it rose in material which initially contained few twins per grain [280]. This suggested to them that deformation was driving the sample toward an equilibrium state which balanced concurrent twinning and detwinning [280]. In support, Kobler et al. cited prior reports showing that nanocrystalline metals can twin and detwin under deformation, even for high stacking fault materials [281, 282]. Luo et al. [283] found that the number of twinned grains in nanocrystalline Au increased after fatigue loading, although their proposed twin assisted grain growth mechanism appears to predict twins with misorientations outside the accepted range. Figure 5.10 shows the cumulative distribution of twins based on their deviation from the ideal 60° <111> misorientation, up to the Brandon criterion of 8.66°. In such a figure, perfect twins will skew the distribution towards the left and the curve becomes sharper, while less perfect twins will cause it to skew right and more gradually rise to the total twin fraction present. Mechanical cycling causes the distribution to skew progressively leftwards, toward low deviation angles. This reveals that cycling preferentially increases the number of

near-perfect twins. Such a trend suggests that there is an increase in the fraction of coherent twins, which are more likely to have near-perfect misorientations [284]. This rearrangement could be facilitated by the rotation of existing twins toward perfect twinning, as reported in molecular dynamics experiments by Panzarino et al. [195]. It could also be explained by an increase in the length or number of annealing twins. It is desirable to better quantify the types of Σ3 boundaries because of the dramatically different properties they may exhibit [284]. Unfortunately, the two-dimensional TKD data does not provide boundary plane inclination. The stereological method developed by Saylor et al. [285] is not applicable because of the low number of boundaries. In the future, emerging three-dimensional techniques with nanometer resolution could be used to provide added detail [286].
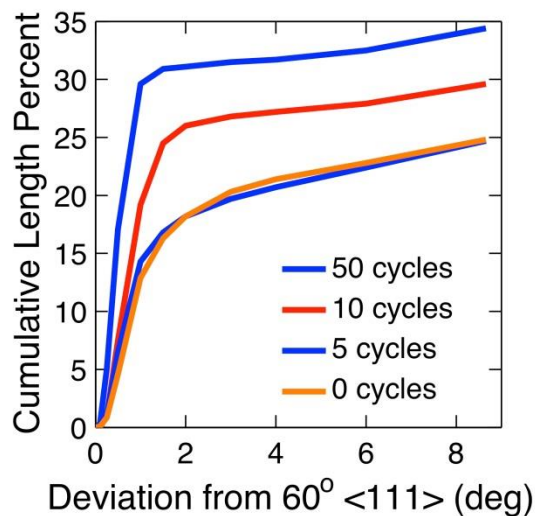
Figure 5.10: The cumulative distribution of Σ3 boundaries as a function of their deviation from the ideal 60° <111> misorientation are shown for thermomechanically processed material. It shows that, on average, the Σ3 boundaries become more perfectly aligned after mechanical cycling at 100 °C.

Our as-deposited material had an initial Σ1 fraction of 5.8%, much lower than the 25.6% reported by Brons and Thompson [279]. Changes to the Σ1 fraction are shown in Figure 5.9(a), revealing that mechanical cycling at 100 °C caused the Σ1 fraction to decrease to 2.3%. One

115

possible explanation is the grain-rotation-coalescence model proposed by Haslam et al. [278], in which rotation reduces boundary misorientation until neighboring grains merge. Panzarino et al. also observed that neighboring grains could rotate and coalesce into new grains with bent lattices [195]. Fatigue stress in ultrafine grained Cu has similarly reduced the fraction of low angle grain boundaries (LAGB) [287].

The fractions of $\Sigma 9$ and $\Sigma 27$ boundaries is slightly reduced by mechanical cycling (although always within the error bars of our annealed data), which is in contrast to the behavior encountered in coarse-grained grain boundary engineering. An increase in the $\Sigma 3$ fraction typically leads to more $\Sigma 3$-$\Sigma 3$ interactions, which in turn produce twin variants by the CSL product rule [138]. The slight drop in $\Sigma 1$ and $\Sigma 9$, 27 fractions yielded a total special boundary fraction ($\Sigma 1$-29) that increased less than the $\Sigma 3$ fraction. The CSL fractions discussed here have been included in Table 5-1 for easy reference.

Table 5-1: GBCD data for mechanically cycled and annealed nanocrystalline nickel.

Number of Loading Cycles [time held at temperature (min)]	Temperature (°C)	$\Sigma 1$ (Length %)	$\Sigma 3\%$ (Length %)	$\Sigma 9\%$ (Length %)	$\Sigma 27\%$ (Length %)	$\Sigma \leq 29\%$ (Length %)	Average Grain Size (nm)
0	22	7.4±0.9	23±1	4.3±0.7	0.4±0.3	41±2	22
Monotonic	22	7.0±0.9	23±1	4.4±0.7	0.5±0.3	42±2	22
125	22	6.0±1	23±2	3.2±0.7	1.0±0.6	40±2	22
0 [60]	100	6.6±0.8	22±1	2.6±0.5	0.4±0.3	38±2	21
0 [79]	100	5.8±0.6	20±1	3.2±0.5	0.7±0.3	37±1	21
0 [98]	100	6.4±0.8	23±1	2.5±0.5	1.1±0.3	41±2	19
0 [250]	100	7.1±0.7	22±1	2.5±0.4	0.3±0.2	39±1	27
Monotonic [60]	100	6.6±1	25±2	3.1±0.8	1.0±0.6	42±2	20
5 [79]	100	5.7±0.6	25±1	3.0±0.4	0.4±0.2	41±1	25
10 [98]	100	2.6±0.4	30±1	2.7±0.4	0.4±0.2	40±1	30
50 [250]	100	3.7±0.4	34±1	1.9±0.3	0.4±0.2	46±1	51

Triple junction distributions were used to quantify the frequency of interactions between special and random boundaries. In a typical GB engineering process, type 3 triple junctions would be expected to increase and type 0 junctions would decrease, which is indicative of increasing special-special interactions [138, 160]. The effect of annealing and mechanical cycling on the fraction of each junction type is plotted in Figure 5.11. The small number of junctions sampled led to wide confidence limits and requires a cautious interpretation. The type 3 junctions underwent the expected increase, showing a special boundary fraction that is incorporating into the grain boundary network [160]. The slight drop in type 2 boundaries can be explained by their conversion to type 3 boundaries under the triple junction product rule. The unchanged type 1 fraction is also predicted by the theoretical triple junction distribution [160]. The constant type 0 fraction differs from the theoretically predicted drop [160]. Overall, the trend is suggestive of an increasing $\Sigma 3$ fraction that is somewhat integrated into the boundary network. The small map size used in this study precludes corroborating this with a more rigorous cluster mass analysis of network connectivity [81].
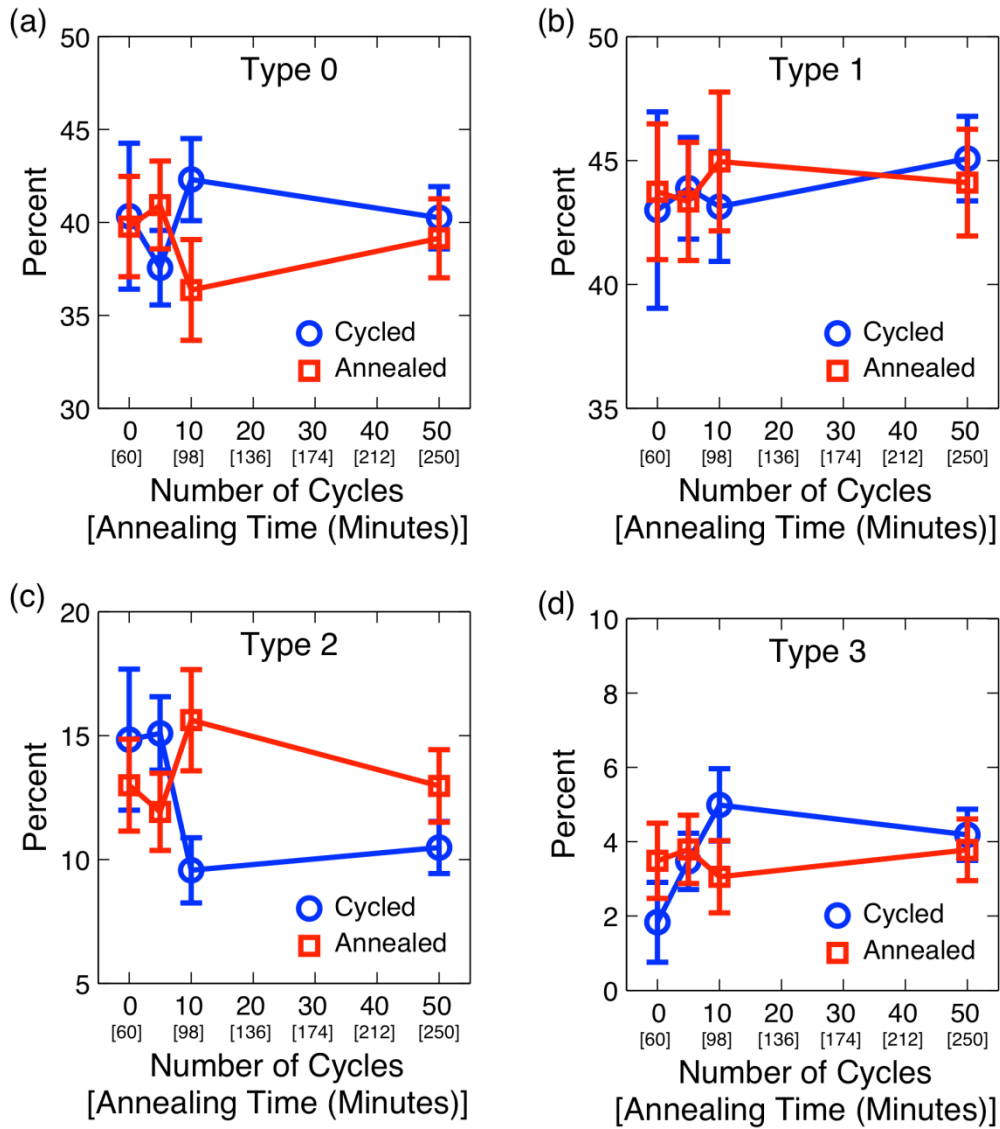
Figure 5.11: The triple junction distribution is represented as the fraction of (a) type 0 (no special boundaries), (b) type 1 (1 special and 2 random boundaries), (c) type 2 (2 special and 1 random boundaries), and (d) type 3 (3 special boundaries). The material was either annealed (red squares) or mechanically cycled at 100 °C (blue circles).

Warm Static Loading

The structural evolution we observe in the TEM images, cumulative grain size distribution functions, and GBCDs all correlate with the number of stress cycles. However, before attributing the cause of these observations to cyclic plasticity, the possible role of creep

needs to be explored [113, 288]. To this point, creep and cyclic effects could have been conflated because mechanical cycling exposes the specimen to high stress for a time which is proportional to the number of cycles. To isolate these phenomena, another specimen was cycled at 8 mHz (twice the usual frequency) for 50 cycles. This halved the total time the specimen was exposed to high temperature and stress (125 min versus the original 250 min), while keeping the number of cycles unchanged. Any creep effects should therefore be more pronounced in the sample cycled at low frequency, i.e. for a longer time. Figure 5.12 shows that the GBCD is insensitive to the duration of cycling, demonstrating that creep is of negligible impact and that cyclic plasticity is the driving mechanism. An in situ TEM fatigue study of nanocrystalline films by Kumar et al. [89] showed that grain rotation during cycling can be caused by reversible dislocation motion. If this is the case, it is likely that a ratcheting mechanism can reduce the overall boundary energy [9]. Panzarino et al. [71] used molecular dynamics to show that grain sliding and rotation can also result in increased levels of microstructural evolution as the number of loading cycles is increased. In both of these studies, cyclic loading modified the microstructure in ways not observed under monotonic loading. The relative importance of these several mechanisms and their dependence on thermomechanical conditions are currently open questions. Atomistic simulations will hopefully provide a definitive answer in the near future.
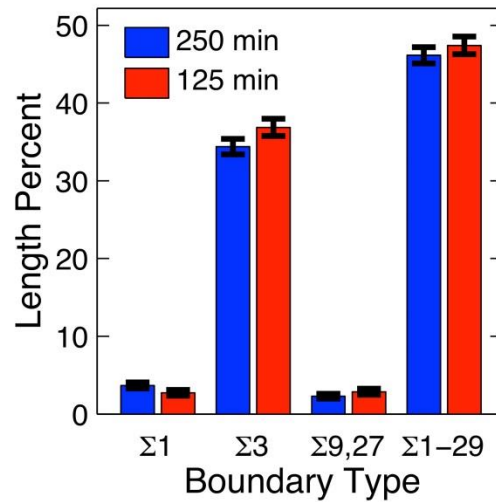
Figure 5.12: For 50 mechanical cycles at 100 °C, the grain boundary character distribution is unaffected by a change from 250 to 125 minutes of total cycling duration. This indicates that creep did not contribute to the evolution of the GBCD.

Possible Effects on Properties

It remains to be shown what effects the observed microstructural changes may have on physical, chemical or electrical properties. The slight changes in triple junction fractions, along with the relatively low total special boundary fraction, suggest that the connectivity of the random boundary network will not be disrupted [160]. This implies that intergranular degradation will not be reduced, even though the Σ3 fraction increased significantly. Still, the increased special boundary fraction would likely affect other properties. Specifically, grain boundary sliding is strongly affected by boundary type; low energy boundaries being most shear resistant and acting to concentrate shear along random ones. Hasnaoui et al. [152] showed that this could produce localized shear flows between special boundary clusters. In addition, dislocation nucleation and dislocation-GB interactions are strongly affected by GB structure [289]. In the case of nanotwinned metals, special dislocation-twin interactions accommodate

significant plasticity while maintaining extraordinary strength [118]. These phenomena suggest that the observed increase in Σ3 fraction is likely to influence strength and plasticity.

While considering the effects of boundary type, the choice of "special" boundaries should be revisited. As recognized in traditional GB engineering research, which boundaries are considered special depends on the property being optimized [284]. For example, corrosion and segregation resistance may be very different for the same boundary type [284]. Similar subtleties are already emerging from the study of nanocrystalline boundary networks, such as Lagrange et al. [156], who showed that a small fraction of incoherent twins can degrade the thermal stability of nanotwinned Cu. Furthermore, boundary mediated deformation mechanisms in nanocrystalline metals are only beginning to be linked to specific boundary types. Given this, it is not clear a priori which boundary types deserve the most emphasis in this study. Nonetheless, the CSL types we have focused on here are a time-tested framework, whose new implications can be further explored in future work.

Conclusions

The effect of deformation on nanocrystalline boundary networks has been studied using nanometer resolution orientation maps. The changes induced by monotonic and cyclic loading were quantified by analyzing the texture, grain size, grain boundary character and triple junction distributions. Deformation at room temperature did not produce microstructural evolution. Similarly, neither annealing nor monotonic loading at 100°C had any effect other than minor grain growth. Significant boundary modification was only seen under the combined influences of cyclic loading and elevated temperature. The extent of boundary evolution was dependent on the number of applied loading cycles. We conclude that the most likely mechanism is a set of

collective deformation processes enabled by enhanced boundary mobility, which explains the observed temperature and cycle dependence.

In addition to providing insight into the deformation response of nanocrystalline Ni, this study suggests a pathway to improve nanocrystalline materials through grain boundary engineering. Based on the observed increase in $\Sigma 3$ boundary fraction, it may be possible to use controlled plastic deformation to tailor nanocrystalline boundary networks and produce more favorable properties. Given the unique deformation processes in nanocrystalline metals, we consider it an open question what grain boundary network characteristics would be ideal. Future work may focus on linking nanocrystalline grain boundary network characteristics with different types of properties, as has been done for traditional GB engineering in coarse-grained materials.

Chapter 6 - The Effects of Large Cyclic Strains on Nanocrystalline Grain Boundary Networks

Abstract

The grain boundary network evolution of nanocrystalline copper was studied under several combinations of temperature and cyclic loading, with strain amplitudes of up to 2% and total strains of 5%. It was found that cyclic loading increased both the grain size and the $\Sigma 3$ fraction, with the magnitude directly related to temperature and accumulated strain. At room temperature, the increase in grain size and twin length fraction were up to 24% and 41%, while at 100 ˚C they were 56% and 151%, respectively. The resulting twin related domains favored larger sizes and repeated twin variant selection. The possible mechanisms are discussed and stress-induced grain boundary migration is concluded to be the most likely explanation.

Keywords: Nanocrystalline metals; Grain boundary; Cyclic loading; Grain boundary migration, Twinning

Introduction

Grain boundary engineering of a nanocrystalline metal has been an attractive goal for quite a few years [94, 290]. The motivation is provided by the extreme density of grain boundaries, which makes their character especially important [17]. The most successful attempts to control nanocrystalline grain boundary character have relied on creating a high density of growth twins in low stacking fault energy metals produced by sputtering [154] or electrodeposition [119]. This parallels conventional grain boundary engineering, where improvements in properties have also come from techniques that increase the twin fraction [95, 179]. Other nanocrystalline GB engineering techniques have used either in situ deposition treatments or post-deposition annealing to increase the $\Sigma 3$ fraction [291, 292]. The results have included improvements in ductility [119], fatigue life [293], corrosion resistance [162] and

conductivity [119]. While these materials have the high twin fractions typical of conventional grain boundary engineered metals, they also have columnar grain structures that pose new challenges. Lagrange et al. [156] showed that the grain boundary network topology leaves these materials vulnerable to thermal coarsening, despite the supposed stabilizing effect of the twins. Recently, a warm cyclic deformation process has been used to increase the length fraction of twins in nanocrystalline Ni by 48% [196]. This type of thermomechanical approach is appealing because it does not produce a columnar structure and could theoretically be applied to a bulk nanocrystalline material, similar to the practice of conventional grain boundary engineering.

Several opportunities exist to extend the understanding of how nanocrystalline grain boundary networks are affected by this type of warm cyclic deformation treatment. These include clarifying the role of the process parameters, understanding the active mechanisms, and describing longer range changes in the grain boundary network. While the number of stress cycles has been shown to increase the extent of microstructural changes [113] [196], the effect of stress/strain amplitude is less clear. Similarly, these previous study did not address grain boundary connectivity except through triple junctions [196]. The following pages will aim to expand on these points by using improved techniques to collect larger orientations maps over a greater range of cyclic strains and temperatures than were employed in our previous work. Clarifying the active mechanisms is of particular interest because they are likely to be encountered in the context of other nanocrystalline processing methods and service environments.

Materials and Methods

Nanocrystalline Cu films were sputter deposited with a grain size of ~20 nm, which is well within the nanocrystalline regime, but still large enough for successful orientation mapping

[45]. A 5 cm diameter planar direct current magnetron system (LAB Line, Kurt J. Lesker, Jefferson Hills, PA) was operated at an argon pressure of 4 milliTorr and a power of 40 W, which yielded a deposition rate of 0.057 nm/sec. The pre-deposition chamber pressure was in the range of 10^{-6} Torr. A total thickness of 103 ± 9 nm of Cu was deposited onto 22 μm thick cellulose acetate substrates. This polymer substrate was used because it reduced strain localization in the Cu during loading. This technique is adapted from the flexible electronics community, who have shown that this type of composite allows much larger strains to be applied to ductile metal films than would be possible if they were free standing [294]. It can be well modeled as a Voigt iso-strain composite [295]. Identical strains in the Cu and Acetate were verified by using a scanning electron microscope (Phenom Pro-X, Eindhoven, NL) to check for cracks or delamination, which were not detected. This requires strong adhesion and was achieved by preparing the cellulose acetate with a dehydration bake and a titanium layer of ~1 nm thick. The goal of this approach is to enable larger strains than were possible in prior work [196]. It has been hypothesized that larger strains could increase the extent of grain boundary mediated deformation and the accompanying boundary network evolution.

Warm cyclic strains were applied to the acetate/Cu composites because our previous work indicated that elevated temperature and cyclic strain can combined to cause grain boundary network evolution. For elevated temperature tests, the samples were warmed with hot air. A standard load frame was used (Instron 5848, Norwood, MA). The specimens were approximately 3 mm wide, with a gauge length of 27 mm. The tests were all displacement controlled, with most using a 2% tensile strain, followed by a 1.97% unloading strain, repeated 100 times, at a strain rate of $10^{-3}s^{-1}$. The result was a superimposed ramp and triangle wave, which is shown in Figure 6.1 (a,b). Part (a) shows all 100 load cycles, while part (b) shows only

125

the first 5 cycles. The peak strain slowly rises from 2% to 5%, with a constant 2% amplitude. This will be referred to as the 2-5% cycling condition . Notice from Figure 6.1 (c) that the acetate remains elastic to strains of ~2%, far more than a copper film can sustain. This means that during loading the metal film is deformed past its elastic limit in tension and then plastically until a total 2% strain is reached. Upon unloading, the copper film will experience an elastic unload, followed by plastic compression until the acetate is relaxed. The acetate is capable of compressing the metal film because of its much greater thickness. This approximates a fully reversing load on the copper, which is an unusual feature in a tension-tension test geometry. Figure 6.1(b) highlights how the unloading step only released 98.5% of the tensile strain from the prior loading. This slow increase in the peak displacement helps compensate for creep in the acetate. Since the acetate creeps at room temperature, a simple triangular displacement profile would have led to ever diminishing elastic strains. The advantage of the applied loading profile is that it maintains a high elastic strain amplitude in the acetate, and therefore its ability to apply a reversing load to the metal film. The stress is given as a fraction of the peak stress because the actual load partitioning between the metal and polymer is unknown. Attempts to deconvolve them with a composite model failed because the properties of the acetate vary under the influence of cyclic loading and temperature. These variations masked the relatively small effect of the copper layer, which is only 0.0045 times the thickness of the acetate. A similar loading profile as shown in Figure 6.1(a) was also used, but with a 1% tensile strain and 0.985% unload, at a strain rate of 5×10^{-4} s^{-1}. This will be called the 1-2.5% cycling condition because the peak strain goes from 1% to 2.5%. Warm cycling temperatures of 60 ˚C and 100 ˚C were also used. While the acetate creep becomes more severe at higher temperatures, the stress state remains highly reversing, see Figure 6.1(d). The upper limit of 100 ˚C was selected because it produced

126

a modest increase in grain size in the absence of strain. Our prior study indicated that this level of thermal activation is sufficient to facilitate grain boundary evolution when applied in combination with a cyclic stress [196]. All materials were held at temperature for 70 minutes.
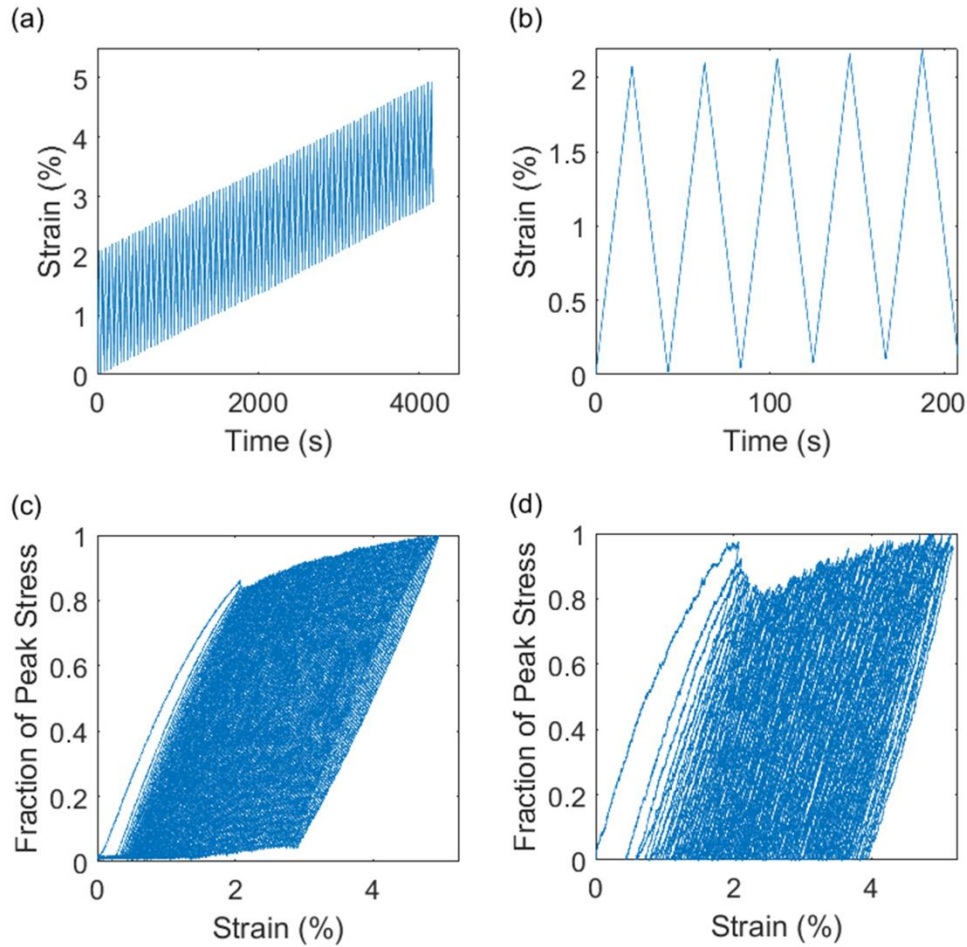
Figure 6.1: The 2-5% strain cycling applied to the acetate/copper composite, with 100 cycles shown in (a) and a closer look at the first 5 cycles in (b). The mechanical response at 20 °C is shown in part (c), and 100 °C in part (d).

Orientation maps were collected with transmission Kikuchi diffraction (TKD), which provides the nanometer resolution necessary for such small grains [44, 45]. Improved microscope stability allowed the maps in this work to be much larger (~10^6 nm^2) than our previous study (~10^4 nm^2). Samples were prepared for TKD by dissolving the cellulose acetate with acetone, rinsing in methanol and then isopropyl alcohol and affixing to TEM grids with

adhesive. The free standing foils were further thinned by ion milling at 2 KeV and 1mA (Gatan model 691, Pleasanton CA). These relatively low power parameters were selected to avoid damage to the thermally sensitive samples. Once loaded into the SEM (FEI SCIOS, Hillsboro OR), an in-chamber plasma cleaner was used for 90 seconds to reduce organic contamination prior to scanning. All orientation maps were collected with a 2 nm step size and post-processed with a standard dilation clean-up. An FEI Titan transmission electron microscope (TEM) was also used to collect images of the microstructure and check the sample quality before TKD.

Results

Grain Size

Microstructural evolution in a nanocrystalline metal can be partially assessed using TEM, which provides a rapid assessment of overall size and grain morphology. Bright field TEM images showed that the as-deposited material had the desired nanocrystalline grain size of about 20 nm. This fine grain size was stabilized by oxygen impurities introduced during the sputtering process, with small oxide particles observed at some triple junctions using energy dispersive spectroscopy. Bright field images of each material are shown in Figure 6.2, arranged according to the applied cyclic strain and temperature. The three images in the top row of Figure 6.2 all show materials that were heated to 100˚C for the 70 minutes. The difference between the materials is the extent of cyclic strain that they were subjected to while hot. The leftmost material was not strained, while the rightmost underwent 100 strain cycles, with a peak strain of 5%. This is the so-called 2-5% strain case. The middle image corresponds to an intermediate level of strain, the 1-2.5% case. From these three data points, it is clear that higher plastic strains led to greater grain growth. The same trend can be seen in the middle and bottom rows of Figure 6.2, which are for materials strained at 60˚C and 20˚C, respectively.

Regarding the role of temperature, the images in the left hand column of Figure 6.2 show that heating the materials to 100˚C was sufficient to cause grain growth in the absence of stress. Likewise, the right hand column shows that the grain growth which occurred under the influence of cyclic stress was greater at higher temperatures. This raises the question of whether the stress and temperature are independent drivers of grain growth, or if there is a synergistic relationship. In the case of independent phenomena, the principal of superposition applies and the grain growth due to cyclic strain at elevated temperature should be equal to the sum of the grain growth under strain free annealing and that caused by room temperature straining. Answering this question can help to decouple the effects of strain and temperature, which in turn can help to understand the mechanisms at play.
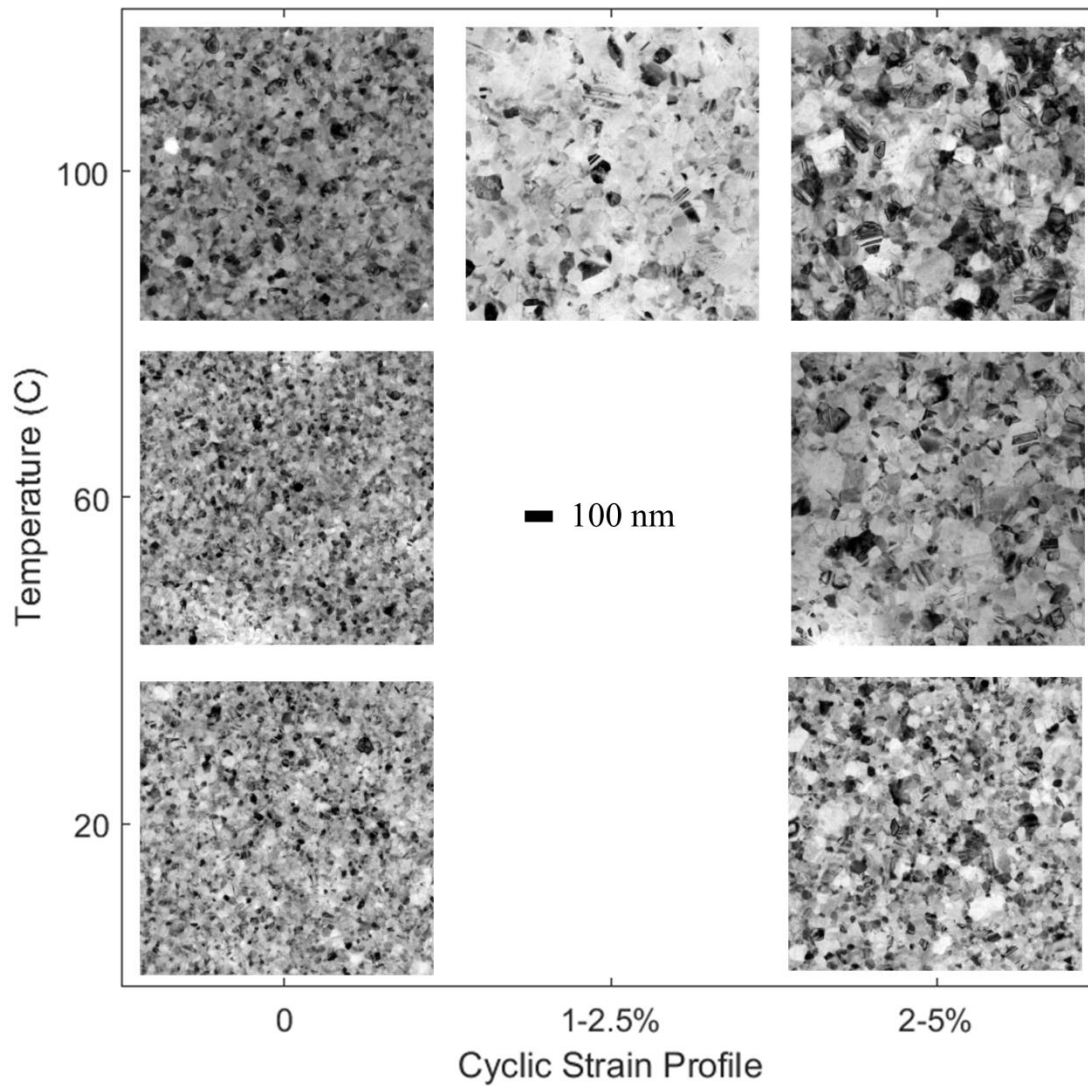
Figure 6.2: Bright field TEM images of each copper sample, with each image's location on the axis marking the thermomechanical process applied. The applied temperature is labeled on the vertical axis and strain on the horizontal axis.

Assessing whether or not strain and temperature act independently requires a more quantitative analysis of grain size. Orientation maps provide a convenient means of accomplishing this, along with also providing a basis for more sophisticated microstructural

130

metrics. Figure 6.3 shows example orientation maps for each specimen. In the left column of Figure 6.3, each pixel color represents a measured orientation, no post-processing having been performed on this set of maps. The black areas are those locations where no orientation could be determined. Even in their unprocessed state, many of the same trends visible from the TEM images are also apparent. The first step in quantitatively analyzing these maps was to assign orientations to the black pixels. This was done with the typical dilation process. When this was complete, any grain composed of fewer than 4 pixels was eliminated and the dilation repeated. The grain reconstruction used a 2° threshold to separate grains, with $\Sigma 3$ boundaries counted as grain boundaries. The grain diameter was found by first computing the mean grain area, which was then converted to an equivalent circle diameter.

These grain size measurements, presented in Figure 6.4, show the same qualitative trends as the TEM images. Quantitatively, this plot also shows that the effect of temperature and strain cycling are clearly not independent processes. The total increase in grain size under the simultaneous action of cyclic strain (2-5%) and high temperature (100°C) is 83% more than the sum of the two individual processes. The same trend held for the case of cyclic strain at 60°C. This implies that the mechanism(s) responsible for the cyclic strain related grain growth must be enhanced by higher temperatures. The error bars in Figure 6.4, and all other figures with error bars, represent the 95% confidence interval.

Another effect of warm cyclic strain was to broaden the grain size distribution, as shown in Figure 6.5. In this type of cumulative distribution plot, the vertical axis displays the fraction of grains smaller than the size listed on the horizontal axis. For materials of different mean grain sizes, but identical distributions, the curves would be offset but have the same shape. A broader range of grain sizes manifests as lower peak curvature. The fact that no tail is observed at the

131

lower grain sizes indicates that the TKD resolution was insufficient to resolve the smallest grains present. Only the as-deposited material and 100 ˚C samples are shown for the sake of clarity.

(a)   (b)   (c)

100 nm ▬

(d)   (e)   (f)

100 nm ▬

(g) (h) (i)

100 nm ▬

(j) (k) (l)

100 nm ▬

(p)   (q)   (r)

100 nm

(m)   (n)   (o)
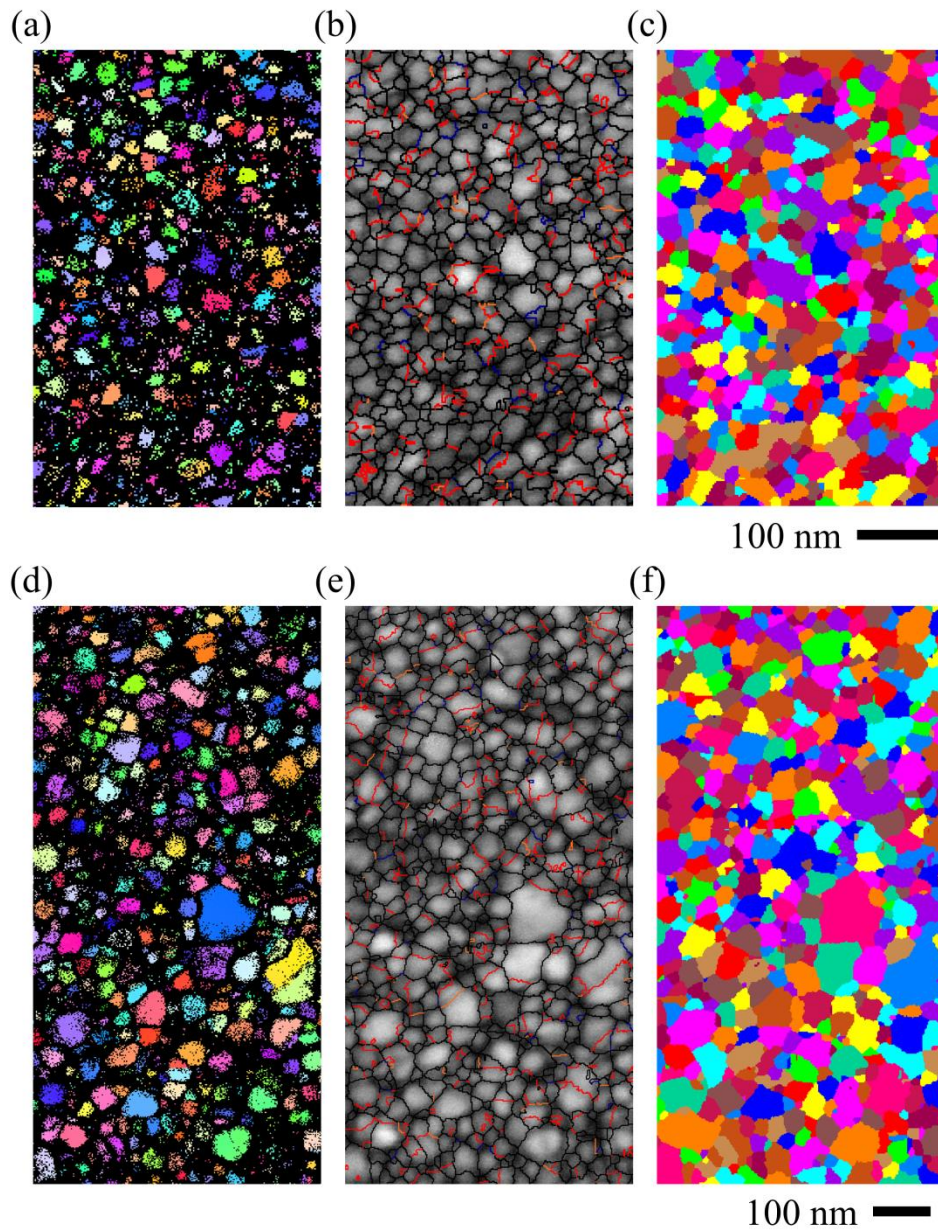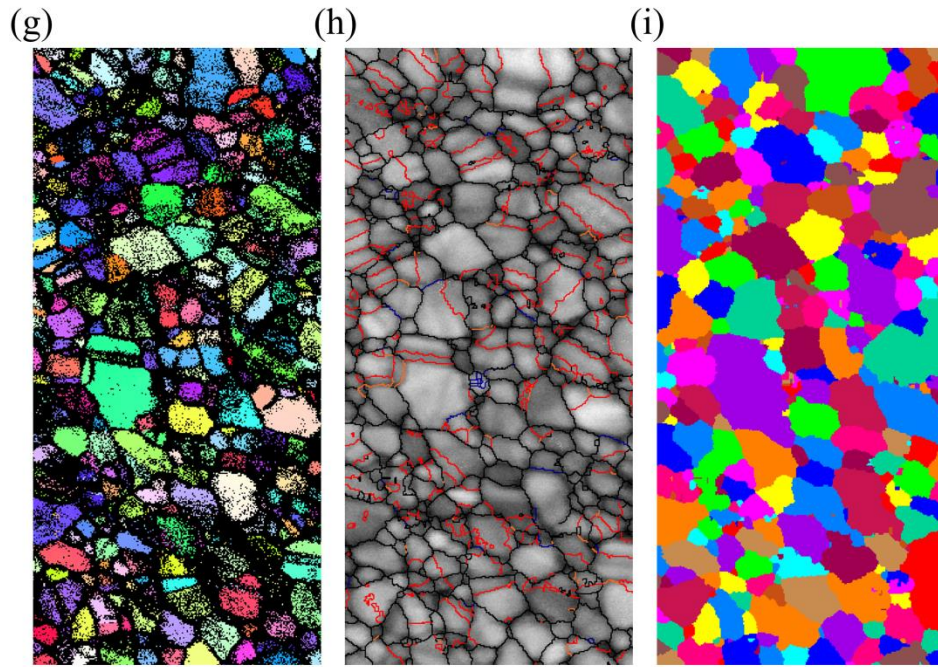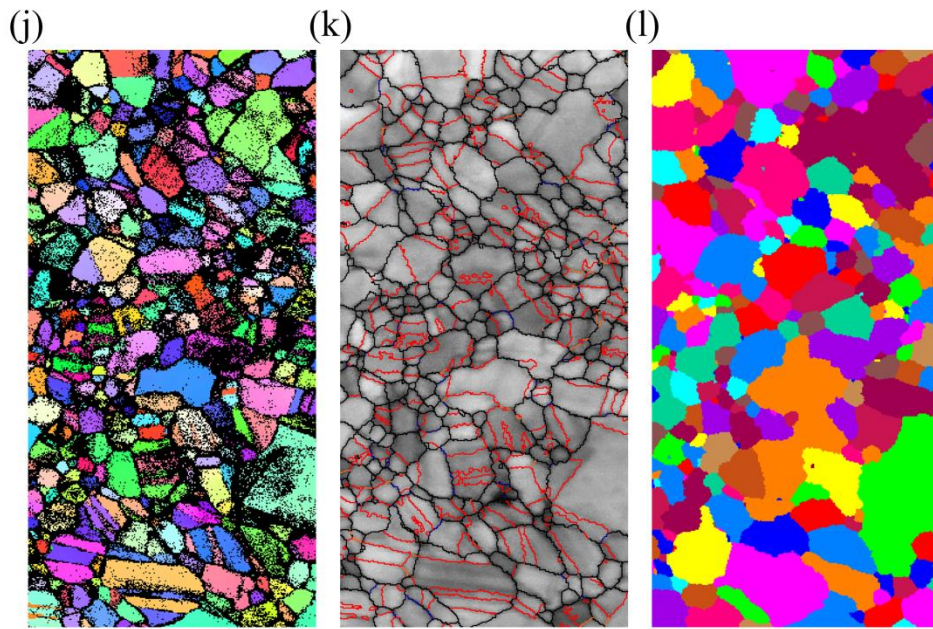
100 nm
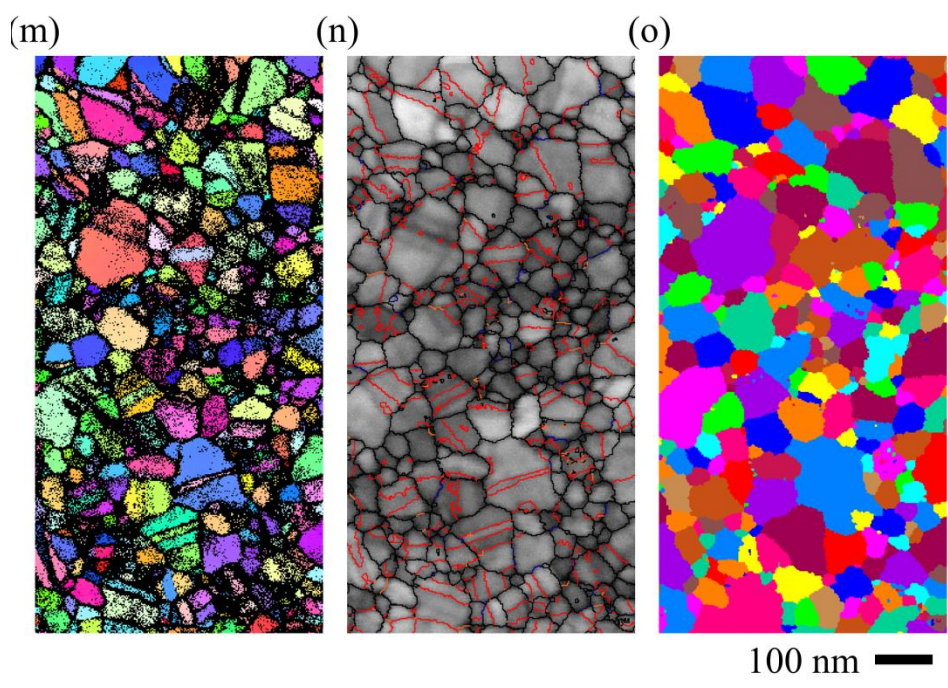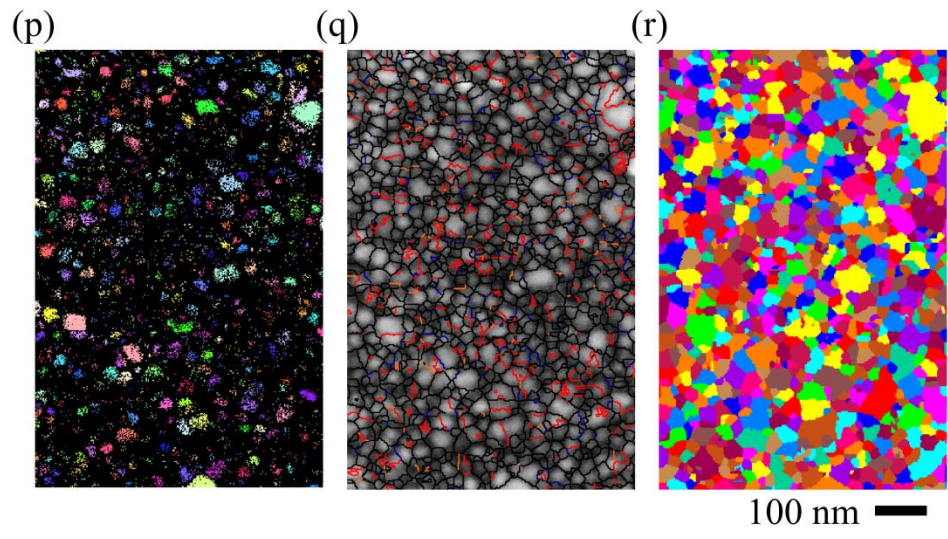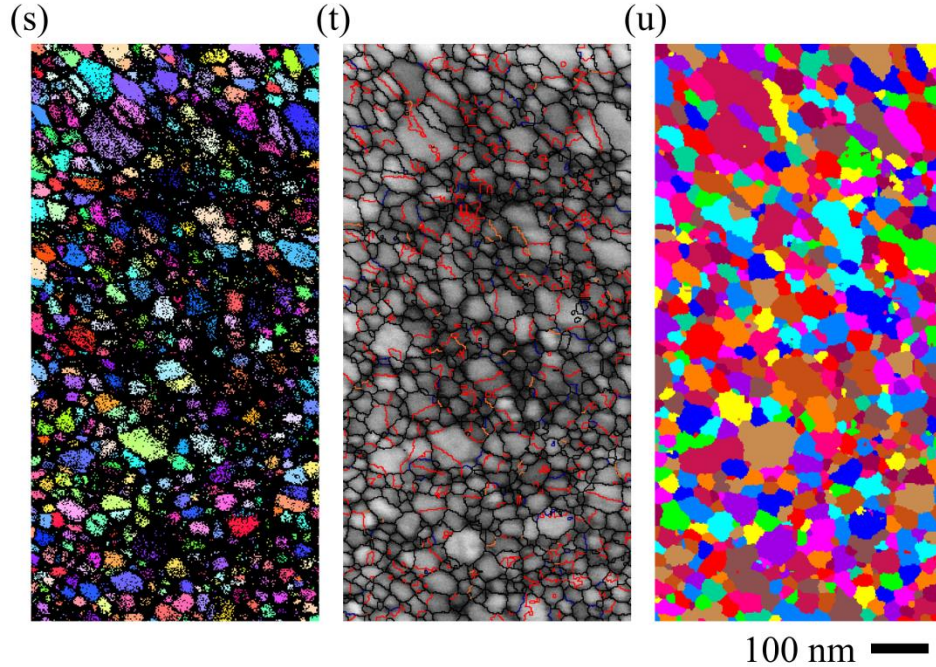
Figure 6.3: The unprocessed inverse pole figure (IPF), grain boundary and twin related domain maps for each specimen, shown respectively in the left, center and right columns. The as-deposited material is shown in parts (a-c), 2-5% 20 °C in (d-f), 2-5% 60 °C in (g-i), 2-5% 100 °C in (j-l), 1-2% 100 °C in (m-o), 0% 60 °C in (p-r), 0% 100 °C in (s-u).
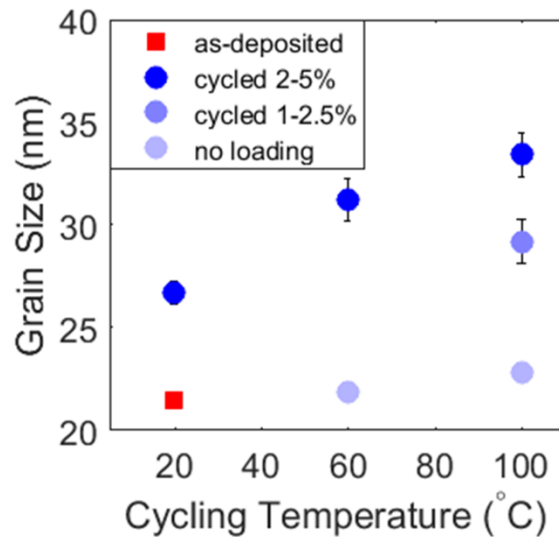
Figure 6.4: The effect of cyclic strain and temperature on grain size. The red square shows the as-deposited case, and the shade of each blue circle corresponds to the level of strain for every other material.
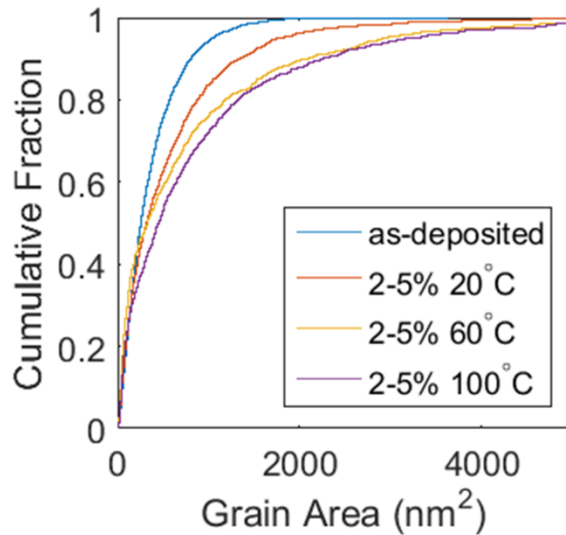
Figure 6.5: The grain size distributions for the as-deposited material and those cycled 2-5% at several temperatures.

Grain Boundary Network

Using the grain orientations available from the orientation maps, each boundary can be classified according to the coincident site lattice criterion [49]. The middle column of Figure 6.3 shows the reconstructed grain boundaries overlaid on the Kikuchi pattern quality. The $\Sigma 3$ boundaries are shown in red, $\Sigma 9$s in orange, $\Sigma 5$, $\Sigma 7$ and $\Sigma 11$s in blue and all others in black. The relative length and number fraction of various CSL types could then be plotted as the grain boundary character distribution, see Figure 6.6. Just like in our previous work on Ni, the most obvious change is the fraction of twin boundaries [196]. None of the non-$\Sigma 3^n$ low CSL boundaries underwent significant changes. As Figure 6.7 shows, the length and number fraction of twin boundaries both increased with strain cycling. The trends observed for $\Sigma 3$ fraction are very similar to those seen for grain size. In both cases, the changes were correlated with cyclic strain and temperature. Just like in the case of grain size, the increase in $\Sigma 3$ fraction is apparently due to a synergistic combination of elevated temperature and strain, with the combined effect

being from 1.2 to 1.4 times the summed individual effects, measured respectively by number and length. Regarding whether twin nucleation or the preferential destruction of non-twins occurred, this cannot be assessed from boundary fraction.

The $\Sigma 3$ length and number fraction metrics convey subtly different information. An increase in number fraction indicates that either more twins were added to the microstructure or that other boundaries were preferentially removed during the grain growth. In addition to these possibilities, the length fraction is also sensitive to the relative length of $\Sigma 3$s compared to other boundaries. These facts can be combined to give a measure of the average twin length by simply dividing the length fraction by the number fraction. In general, it is expected that twins will have longer mean lengths than other boundaries because of their low energy [138]. This is the case for each material studied here, with twins being from ~1.5-3 times the length of other boundaries. This relative length was increased by cyclic strain, with the general trend following that of grain size and twin fraction. This data is shown in Figure 6.8.

Cyclic strain also caused changes in the twin boundaries' deviation from the ideal CSL misorientation. Figure 6.9 shows that cycling 2-5% at 100°C caused the length-weighted mean deviation to drop to 1.4°, down from 2.3° in the as-deposited material. A similar change was observed in the number-weighted mean CSL deviation. These changes could be caused by the lengthening or creation of coherent twins, or alternately by the shortening/destruction of incoherent segments. Alternately, this result requires a change in the misorientation of existing $\Sigma 3$ boundaries. The distribution of deviations from the ideal CSL was also examined, but no trends were observed beyond the shifting mean. Ideally this metric would also be complemented by an analysis of twin coherency. Such information would provide information on the fraction of

coherent twins by length and number and would help clarify why the mean deviation angle

dropped. Unfortunately, the boundary trace accuracy was insufficient for this analysis.

139
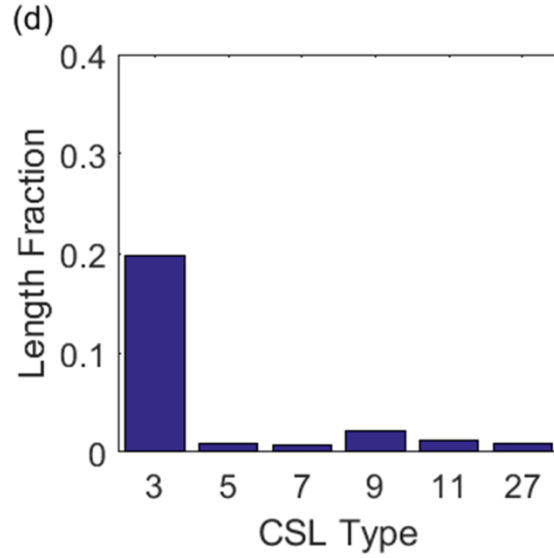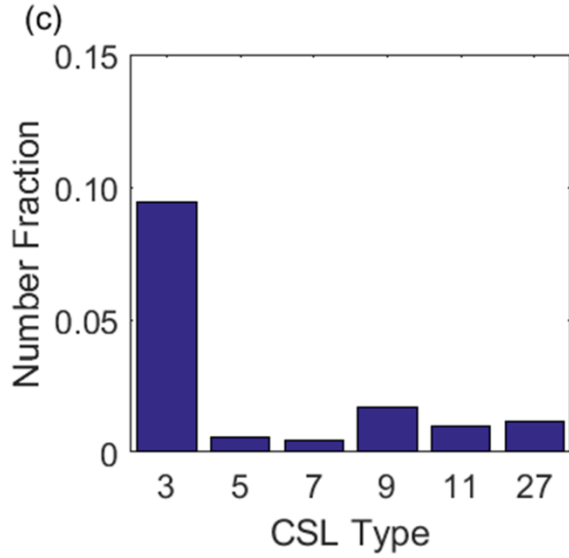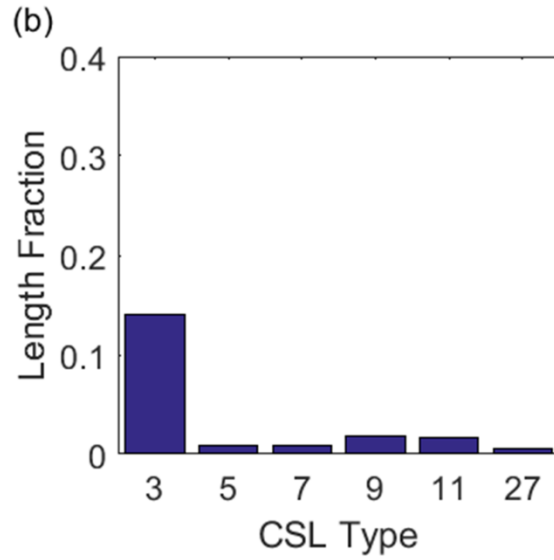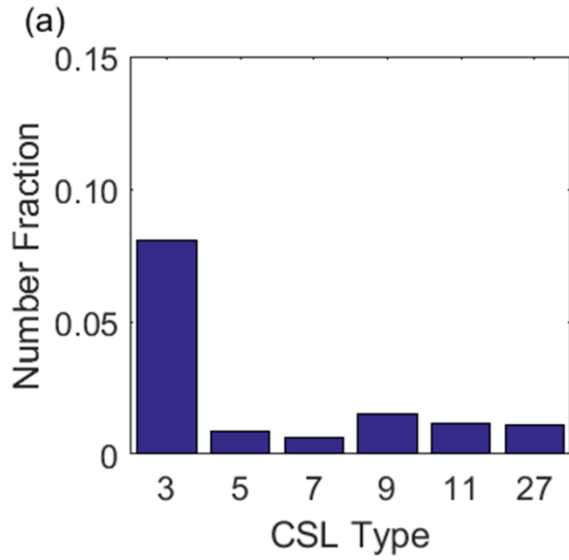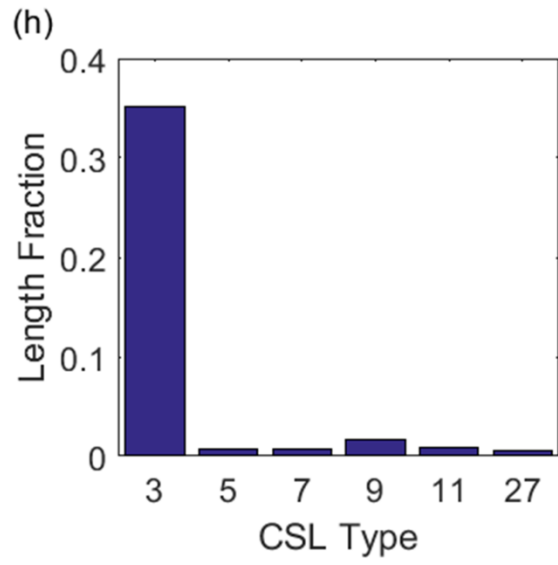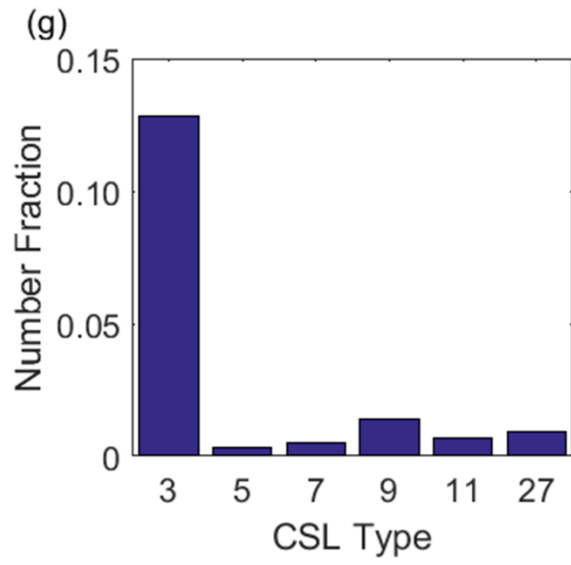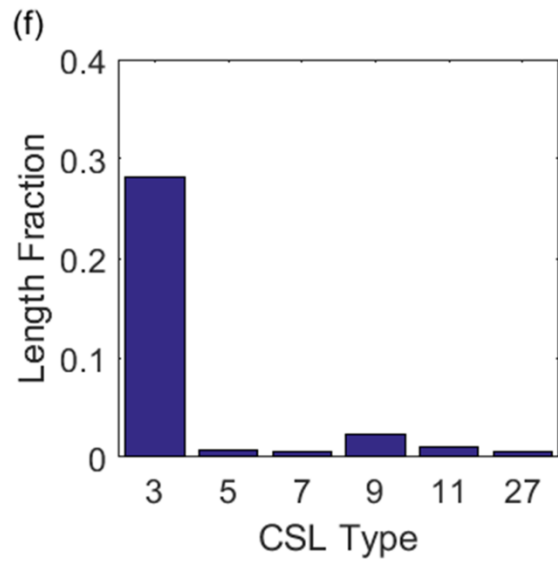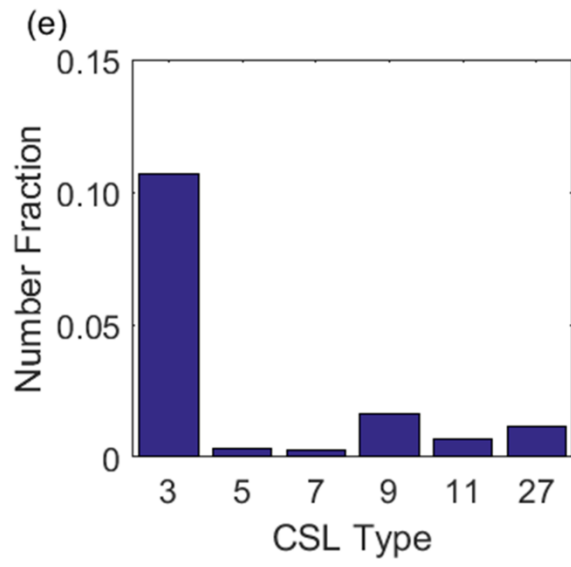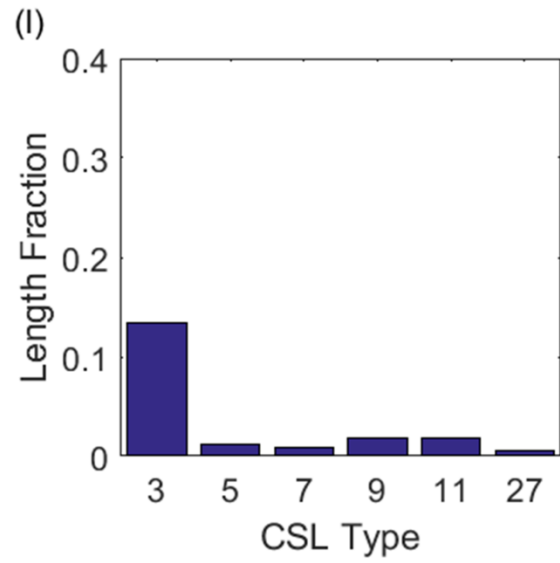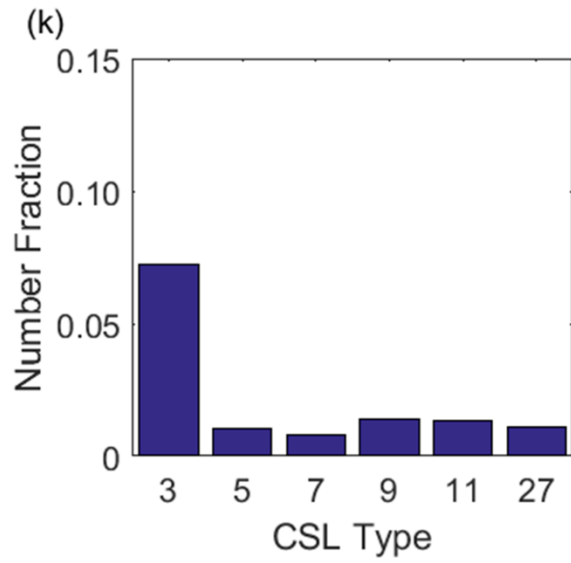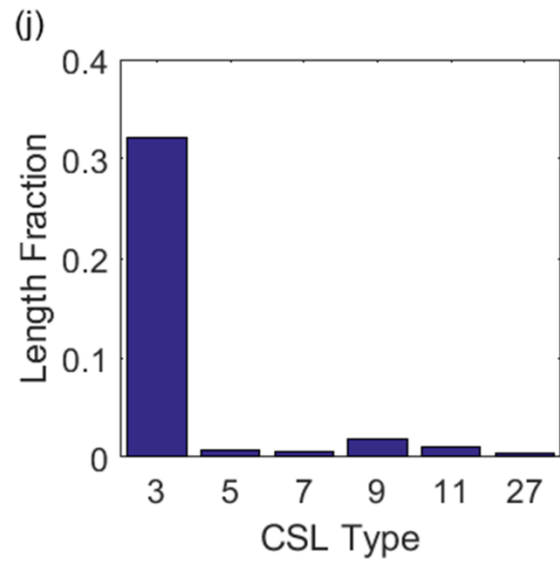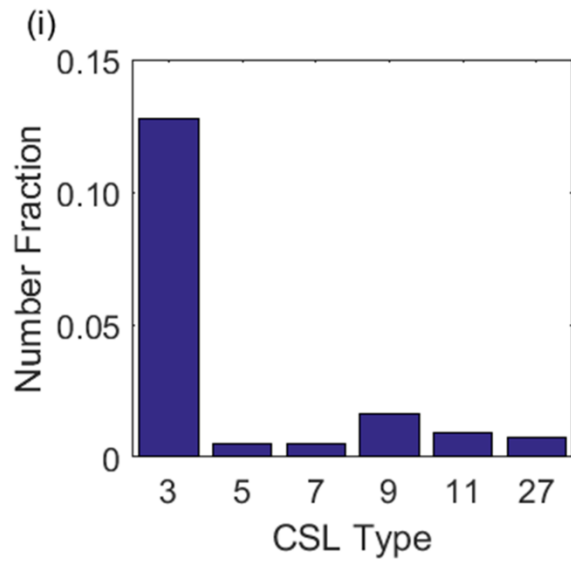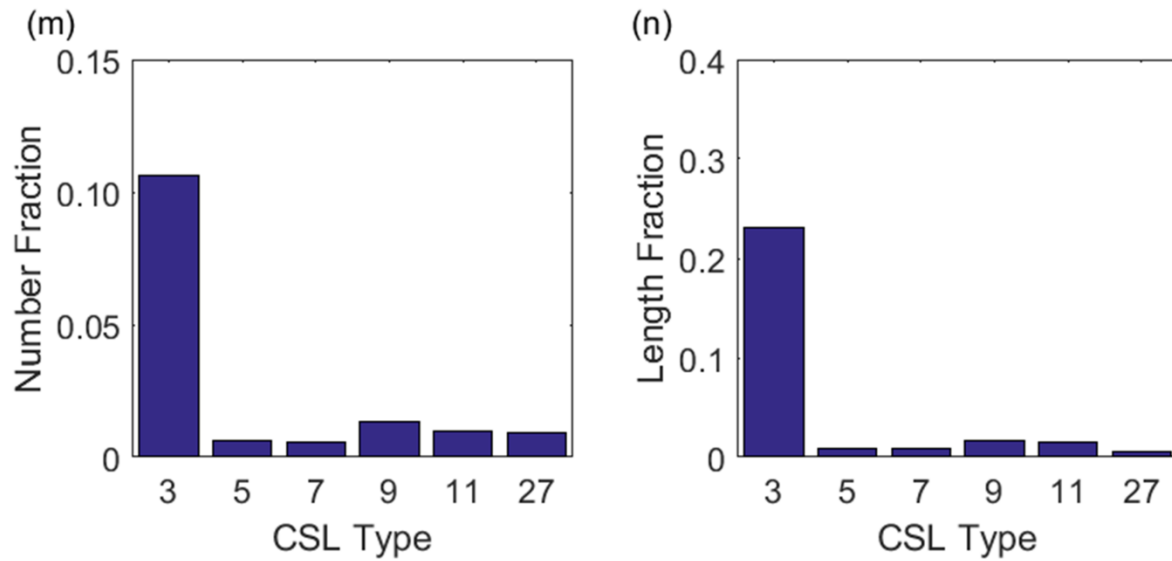
Figure 6.6: The grain boundary character distributions by length and number fraction. The as-deposited material is shown in parts (a,b), 2-5% 20 °C in (c,d), 2-5% 60 °C in (e,f), 2-5% 100 °C in (g,h), 1-2% 100 °C in (i,j), 0% 60 °C in (k,l), 0% 100 °C in (m,n).
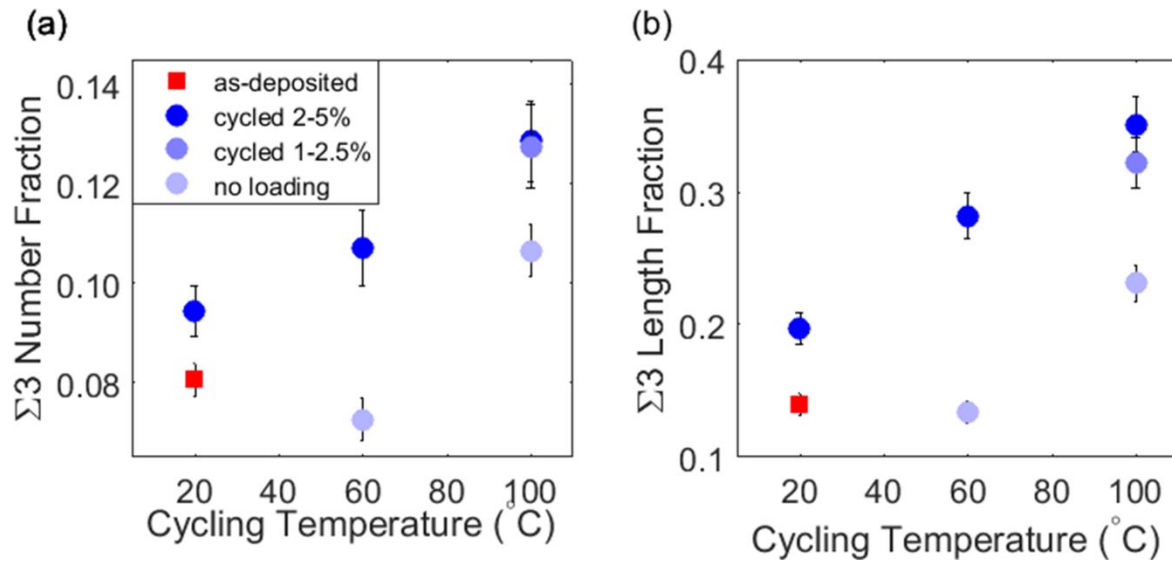

Figure 6.7: The Σ3 number and length fraction of each material, both of which increased with thermomechanical cycling
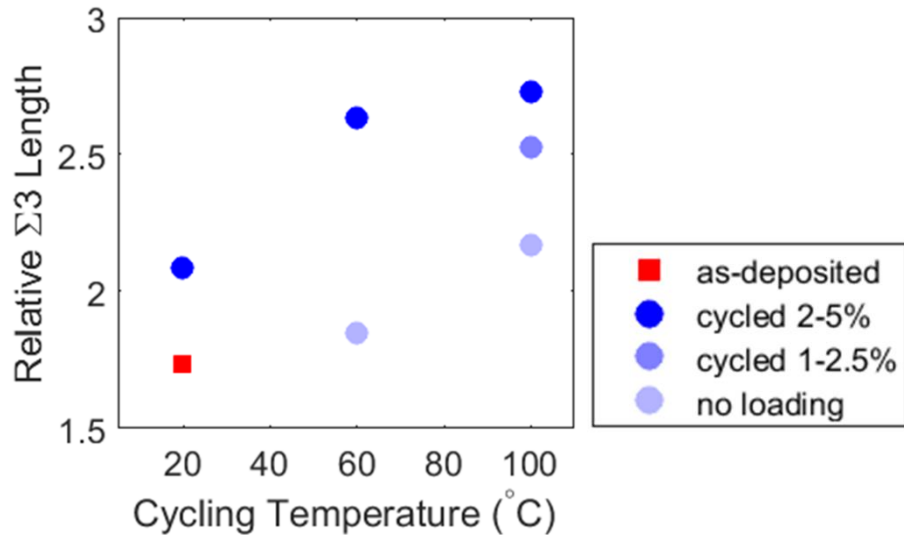
Figure 6.8: The mean length of Σ3 boundaries relative to all other boundaries in each material. In every case Σ3 boundaries were longer than average, with the amount increasing with thermomechanical cycling.
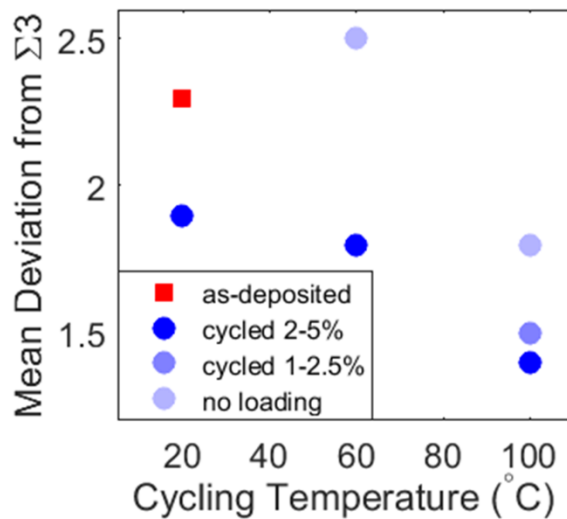
Figure 6.9: The average misorientation angle of the Σ3 boundaries from perfect CSL configuration, termed deviation, decreased with cycling.

While these aggregate statistics are evidence of significant changes in the grain boundary network, the longer range characteristics of that network can also help explain the processes at

work. For this, the concept of twin related domains (TRDs) can be used [53, 93]. TRDs are collections of grains mutually connected by twin boundaries[92]. Most simply, TRDs can be quantified by their size, as measured by the number of twinned grains they contain. These clusters are shown in the right-most column of Figure 6.3, with each TRD assigned a distinguishing color. Figure 6.10 plots the root-mean-squared (RMS) TRD size, which weights each TRD by its number of members. The size of these domains increased in concert with the twin fraction, as is expected [196]. The increase in RMS TRD size can be further broken down by looking at the distribution of TRD sizes, shown in Figure 6.11. Not surprisingly, the number of 1 member TRDs decreases with strain cycling. Either twin nucleation or the removal of untwinned grains would lead to this result. Perhaps more surprising is that the fraction of grains in 2-member TRDs experienced a smaller increase than those in 3-member TRDS. One explanation is that nucleated twins converted two member TRDs into 3 member TRDs at a faster rate than 1 member TRDs became 2 member TRDs. Alternately, 1 member TRDs could have been bisected by new twins and jumped directly to being 3 member TRDs. This point is worth note because it has bearing on the responsible mechanisms. The question of whether or not new twins are nucleated could be settled by the maximum TRD size present in the material. If twins were nucleated, then this number would presumably increase. Unfortunately, the available data does not provide a large enough pool of TRDs for this to be answered with any statistical confidence.
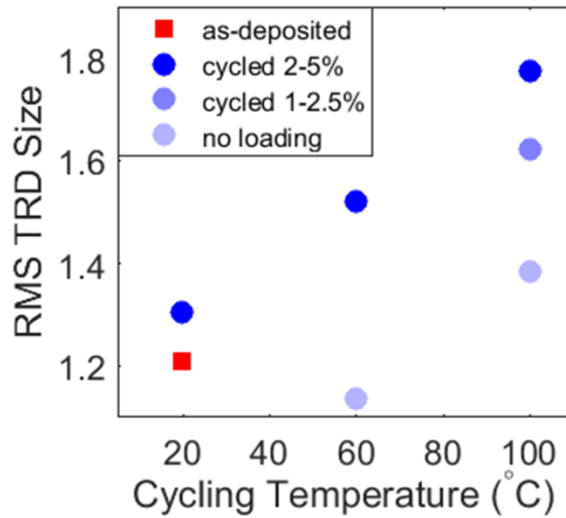
Figure 6.10: The RMS TRD size for each material. The increase in this parameter with cycling indicates that more grains became part of larger TRDs
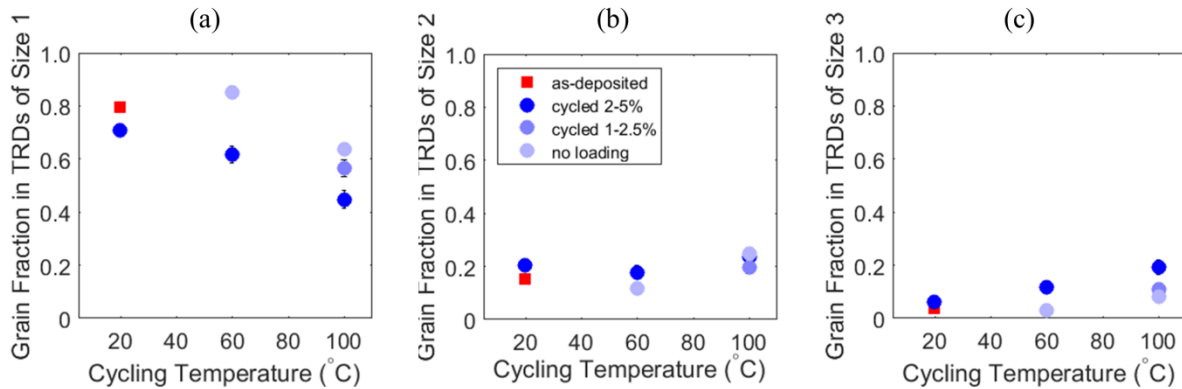
Figure 6.11: The number fraction of grains in TRDs of size 1 are shown in part (a), of size 2 in part (b), and of size 3 in part (c).

The internal structure of twin related domains can also be assessed for changes. The probability of repeated twinning is a measure of the orientation correlation between second nearest neighbors [217, 296]. To understand this metric, consider three grains connected by two twin boundaries. If the two twin boundaries are repeats of the same twin variant, then two of the three orientations will have a $\Sigma 1$ relationship. If the twinning variants are not repeats, then a $\Sigma 9$ relationship must exist. This is a simple case of the more general theory of $\Sigma 3^n$ related domains

144

described by Reed et al. [92]. The probability of repeated twinning looks at the fraction of Σ1 versus Σ9 relationships between second nearest neighbors [217]. This is plotted in Figure 6.12, with only 3 member TRDs counted. While the error bars are too large to draw any conclusions about the changes in repeated twinning, the mean value of all the specimens is intriguing. Each has a probability of repeated twinning in the range of 64-93%. This is much higher than seen in the same sized TRDs of conventional grain size copper which form during recrystallization (~30%) [217].
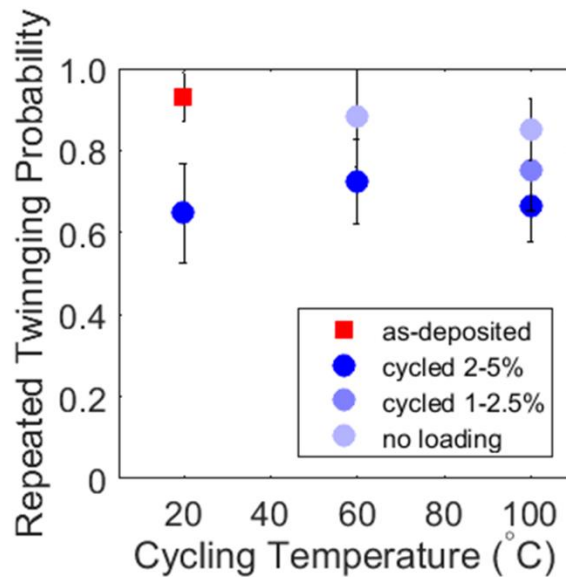
Figure 6.12: The probability of repeated twinning for each material correlates second-nearest neighbor orientations and relates to the frequency with which neighboring twin boundaries are of the same variant.

Discussion

Given these findings on the effect of temperature and cyclic strain on grain size and the boundary network, the next challenge is to identify the responsible mechanism. Whatever this mechanism may be, it seems clear that it needs to predict changes that are proportional to the applied strain and temperature, with the combined effect being greater than the individual ones.

The sought mechanism should also be consistent with prior observations on the interplay of deformation and nanocrystalline boundary networks. These works include several studies that show grain growth during the fatigue of nanocrystalline metals, as reviewed by Padilla and Boyce [113]. An et al. showed that cyclic deformation of nanocysralline Cu could also be accompanied by twinning [297]. There is also our previous work on Ni, which showed the twin boundary length fraction increased in proportion to the number of stress cycles, but with diminishing returns [196].

Curvature Driven Boundary Motion

The observed grain growth at elevated temperatures in the absence of stress indicates that grain boundary curvature was an important driver. That said, the obvious importance of stress means that another mechanism must also have been active in the materials subjected to cyclic strains. The synergistic effect of temperature and strain imply that this unidentified second mechanism must also depend positively on temperature.

Stress Driven Grain Boundary Motion

One potential mechanism for the cyclic strain related grain growth is shear-coupled grain boundary motion. In this phenomenon, shear stress causes normal motion of a grain boundary by driving grain boundary dislocations [28, 29, 298]. This has been observed to occur in stressed bicrystals at high temperatures [298, 299]. This mechanism has also been implicated in several prior studies of deformation related nanocrystalline grain growth [245] [246] [277] [113]. Legros et al., [277] have documented the effect in nanocrystalline aluminum, using in situ TEM to observe rapid grain boundary motion near an opening crack tip [277]. An experiment by Rupert et al. [246] geometrically separated the areas of maximum stress and strain and found that maximum grain growth occurred at the location of maximum stress, not maximum strain. This is

146

consistent with a shear coupling mechanism. Interestingly, stress driven grain boundary motion can reverse direction under continuous loading, apparently because of fluctuating grain boundary structure and bifurcated shear coupling factors [277]. A related phenomena appears to be at work during the fatigue loading of nanocrystalline specimens, where marked increases in grain size having been observed [113]. At the extreme, this coarsening can lead to very large grains and initiate failure [300]. In these cases, inhomogeneous dislocation storage may also become important once the grains become large enough [28].

The observed grain growth depended on the accumulated strain, a fact that may seem at variance with the well-established stress dependence of shear-coupled grain boundary motion. In a weakly strain hardening material like nanocrystalline Cu, high accumulated strain does not translate directly into high stress. This apparent discrepancy can be reconciled by considering how the total plastic strain influences the chances of any individual grain boundary experiencing a high stress. At high macroscopic stress but low strain, some grains will remain at low stress because of polycrystalline inhomogeneity. As strain increases, plastic deformation will cause different grains to become highly stressed. The extremely small grain size means that the motion of even a single dislocation can cause large local strains and changes in stress [301]. That means large strains increase the chance that any given grain boundary will, at least temporarily, experience a stress sufficient to cause significant migration. A similar argument applies to cycle count, because accumulated plastic strain will cause a different stress distribution during each loading and unloading sequence. This is an important point because cycle count has been observed to correlate with grain growth in nanocrystalline Ni [196].

Interestingly, stress induced grain growth would also reduce the flow stress, which in turn would reduce the driver for further grain growth. Such a mechanism may be responsible for a

microstructural rate of change that diminishes with increasing accumulated strain. Such a tend is supported by figures 6.4 and 6.7, which show the 1-2.5% strain case caused more than half as much microstructural evolution as the 2-5% case, despite nominally accumulating only half the plastic strain. Likewise, our previous study of cyclically strained Ni showed a similar trend for the effect of cycle count on twin fraction.

Temperature dependence is another point to be considered in evaluating the potential role of shear coupled motion. It has been shown by Winning et al [298] that the velocity of grain boundaries propelled by a shear stress can be increased several orders of magnitude by a modest increase in temperature. This is because shear coupled grain boundary motion requires dislocation climb and vacancy diffusion [298]. While the exact change in grain boundary mobility is structure dependent, an Arrhenius type relation generally applies [299]. The measured activation enthalpies in Al bicrystals are all on the order of 1 eV [299], thus explaining the strong temperature dependence. One complication is that higher temperature would also be expected to lower the flow stress, and therefore the driving force for migration at yield. That said, the expected drop in flow stress is much less than the accompanying increase in boundary mobility. This indicates that shear coupled grain boundary motion should generally lead to a positive correlation between temperature and grain growth. An exception has been observed in the case of very pure nanocrystalline copper, where indentation-induced grain growth was greater at cryogenic temperature than at ambient. However, the materials in the present study are relatively impure and thermal activation is more likely to be important. For example, Gianola et al. [28] have observed that small oxygen concentrations in Al can inhibit boundary migration at stresses more than double those needed to drive rapid grain coarsening in purer samples.

Next, it must be evaluated if stress-induced grain boundary motion could also be responsible for the twin-related changes in the grain boundary network. In fact, there are several possibilities for how this may have occurred. In the first case, it is well known that a moving grain boundary can provide an opportunity for twinning via either growth accidents [61, 62] or stacking fault packets [64]. Of course, these classic results are based on boundaries driven by plastic strain energy or capillarity and it is unclear if the same phenomena would be expected for stress-driven motion. This possible mechanism has been termed "mechanically driven annealing twinning" by An et al. [297], although it has yet to be widely reported. It is also possible that stress driven grain boundary motion may lead to the lengthening of preexisting twins that are dragged by connecting boundaries. It is thought that the kinetics of shear coupled motion may be limited by the drag of triple junctions, a conclusion drawn by analogy to curvature driven migration [298]. In this situation, the low energy of a twin would mean that dragging the associated triple junction so as to extend the twin should be relatively easy. Lastly, it is believed that low CSL boundaries are more stable under stress driven migration [302], and therefore they may be less likely to be removed from the microstructure. In contrast, a highly mobile grain boundary may be swept across a grain and into another boundary, removing itself from the material. This is the type of preferential survival that is thought to increase twin fraction during conventional grain growth [60, 303].

Either the growth accident or stacking fault packet twinning mechanism would also be compatible with the observed twin related domain size distribution. For a stacking fault packet model, the tendency to form 3 member TRDs is very natural because a single grain bisected by a twin forms a 3 member TRD. This would also fit the observed tendency for a high probability of repeated twinning because the stacking fault packets would create coplanar twin boundaries. For

149

a growth accident model, the propensity to form 3 member TRDs over 2 member ones is less easily explained. It could be caused by a tendency for boundaries to continue migrating once unpinned, with continued motion leading to multiple twinning. The tendency for a moving boundary to drag and elongate a connected twin would not explain this TRDs size distribution, but neither is it incompatible.

Other Possible Mechanisms

The potential role of dislocation plasticity on the microstructural evolution also needs to be considered. For grain sizes from about 100nm to 10nm it is believed that grain boundaries become the predominant dislocation sources and sinks, with no dislocation-dislocation interaction or storage [26, 255, 304]. It is possible for these dislocations to nucleate twins [305-307], and also cause detwinning [293]. In this model, a leading partial is nucleated from the grain boundary, but not followed by a trailing partial, leaving a stacking fault [307]. If another partial is emitted on a neighboring plane, then a twin can be formed. This is similar to deformation twinning in conventional grain size materials and new twinning dislocation multiplication mechanisms have been proposed [308]. It has been suggested that this is the source of unexpected twins in nanocrystalline aluminum [306] and has been the explanation cited for the twinning and detwinning observed by Kobler et al. in deformed nanocrystalline Pd [280]. This type of nanocrystalline deformation twinning shares the same temperature dependence as conventional deformation twinning, i.e. it becomes easier at lower temperatures [309]. This is contrary to the observations in this study and so it seems unlikely that deformation twinning is responsible for the increased twin fraction.

Grain rotation is another possible mechanism that has been proposed for nanocrystalline twinning and grain growth [195, 310]. The idea is that neighboring grains can reduce their grain boundary energy by rotating into a low CSL configuration. The rotation is thought to be

150

facilitated by grain boundary sliding and atomic shuffling events [26, 244, 311]. Alternately, grain boundary dislocation climb has been hypothesized to facilitate grain rotation [312]. Experimentally, Shan et al. [30] and Ke et al. [241] have both presented in situ TEM straining experiments that appear to show grain rotation. This has been followed by in situ precession enhanced electron diffraction based orientation mapping that showed grains rotate relative to their neighbors [313]. It has been proposed that these rotations could cause low angle boundaries to disappear, facilitating grain growth by coalescence [195, 310]. Experimentally, in situ TEM images have shown that clusters of nanocrystalline grains separated by low angle boundaries may be formed via deformation [30]. An analogous process for twin formation has been proposed in which near-$\Sigma3$ boundaries may rotate into a $\Sigma3$ relationship [314]. Panzarino, Pan and Rupert [314] showed molecular dynamics evidence for this process, terming it rotation-induced twinning. Those authors have also observed that the same process produced $\Sigma11$ boundaries [314]. The activity of this mechanism is challenged by the TRD size distribution, which favored the creation of 3 member TRDs over 2 member ones. A rotation induced twinning mechanism would have the opposite effect because it relies on preexisting near-$\Sigma3$ neighbors, which are rare [69]. The probability of clusters of near-$\Sigma3$ neighbors is obviously even less likely, and so the presence of large TRDs is difficult to explain with a rotation based model. The near-constant $\Sigma11$ fraction is also potentially at odds with a rotation-induced twinning mechanism, see appendix A for more discussion of this point.

Conclusions

The magnitude of grain growth in cyclically strained nanocrystalline copper was shown to depend directly on strain amplitude and temperature, with a synergistic effect when applied together. It was also found that cyclic straining caused the number and length fractions of twins

to increase. This was accompanied by an increase in the relative length of $\Sigma 3$s and a decrease in their deviation from the perfect CSL configuration. The twin related domains that formed favored 3-member configurations over 2-member ones, with a high probability of repeated twinning. This adds to prior work showing that the number of stress cycles increases the extent of grain growth and twinning. Of the previously hypothesized mechanisms, stress-induced grain boundary motion provides the most complete explanation for the observations. Neither deformation twinning nor rotation induced twinning are consistent with the observed trends. The results are relevant to nanocrystalline metals processing, understanding possible changes during their service life and to finding improved means for nanocrystalline grain boundary engineering.

Appendix A

It is desirable to have a quantitative hypothesis for the GBCD that would be produced by boundary energy driven grain rotation. Panzarino et al. [314] have tracked the proportion of $\Sigma 3$ and $\Sigma 11$ boundaries during cyclic deformation simulations using molecular dynamics, but necessarily for only a very small boundary population. An alternate means of forming a quantitative hypothesis is to use a simple Monte Carlo simulation using the grain boundary energy function developed by Bulatov et al. [58]. Starting with a random pair of orientations, the minimum energy GB plane was found. Next, a small random rotation was applied and the new minimum energy plane found. If the new GB energy was lower then the new orientation was accepted, and if not, the previous orientation was retained. This eventually leads to the boundary representing the local energy minimum. This rough approximation of the hypothesized mechanism considers only two neighbors to reduce computation. This is somewhat justified because the GB energy landscape contains relatively few cusps and so it is unlikely a grain will have multiple boundaries with high rotation dependent energy gradients. The model also ignores

the magnitude of energy gradient, but tests with arbitrary energy gradient cutoffs showed similar results. The results, shown in Figure A.1, give the expected GBCD for grain boundary energy driven rotation. It predicts that ~80% as many $\Sigma 11$ boundaries should be formed as $\Sigma 3$ boundaries. The conclusion is that a detectable change in one should be accompanied by a detectable range in the other, which is contrary to the observations.
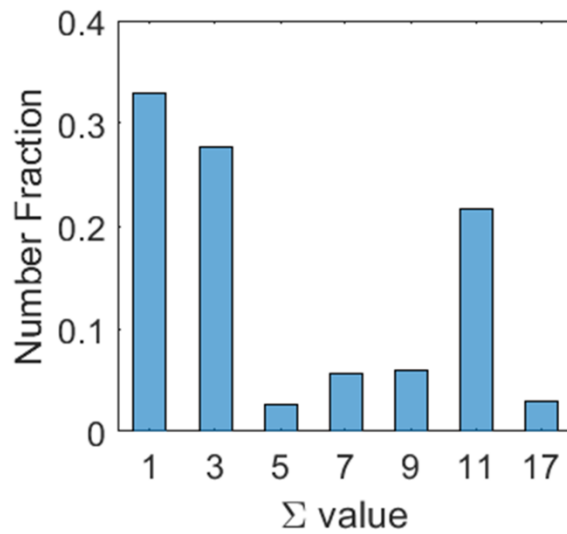
Figure A.1: The GBCD predicted by Monte Carlo simulation of grain boundary energy driven rotation.

References

[1]		Vander Voort GF. Metallography, Principles and Practice, ASM International, 1984.

[2]		Adams BL, Morris PR, Wang TT, Willden KS, Wright SI. Description of orientation coherence in polycrystalline materials, Acta Metallurgica 35 (1987) 2935-2946.

[3]		Venables JA, Harland CJ. Electron backscattering patterns - new technique for obtaining crystallographic information in scanning electron-microscope, Philos. Mag. 27 (1973) 1193-1200.

[4]		Hall EO. The Deformation and Ageing of Mild Steel: III Discussion of Results, Proc. of Phys. Soc. London Section B 64 (1951) 747-753.

[5]		Petch NJ. The cleavage strength of polycrystals, J. of Iron Steel Inst. 174 (1953) 25-28.

[6]		Holden AN, Hollomon JH. Homogeneous yielding of carburized and nitrided single iron crystals, Trans. of American Inst. of Mining Metall.l Eng. 185 (1949) 179-185.

[7]		Armstrong R, Douthwaite RM, Codd I, Petch NJ. Plastic deformation of polycrystalline aggregates, Philos. Mag. 7 (1962) 45.

[8]		Cordero ZC, Knight BE, Schuh CA. Six decades of the Hall–Petch effect – a survey of grain-size strengthening studies on pure metals, International Mater. Rev. (2016) 1-18.

[9]		Khalajhedayati A, Rupert TJ. High-Temperature Stability and Grain Boundary Complexion Formation in a Nanocrystalline Cu-Zr Alloy, JOM 67 (2015) 2788-2801.

[10]		Cantwell PR, Tang M, Dillon SJ, Luo J, Rohrer GS, Harmer MP. Grain boundary complexions, Acta Materialia 62 (2014) 1-48.

[11]		Clark WAT, Wagoner RH, Shen ZY, Lee TC, Robertson IM, Birnbaum HK. On the criteria for slip transmission across interfaces in polycrystals, Scr. Metall. Materialia 26 (1992) 203-206.

[12]		Koning Md, Miller R, Bulatov VV, Abraham FF. Modelling grain-boundary resistance in intergranular dislocation slip transmission, Philos. Mag. A 82 (2002) 2511-2527.

[13]		Eshelby JD, Frank FC, Nabarro FRN. The equilibrium of linear arrays of dislocations, Philos. Mag. 42 (1951) 351-364.

[14]		Li JCM, Chou YT. Role of dislocations in flow stress grain size relationships, Metall.l Trans. 1 (1970) 1145.

[15]		Taylor GI. The mechanism of plastic deformation of crystals. Part I. theoretical, Proc. of Royal Soc. of London Series A 145 (1934) 362-387.

[16]		Ashby MF. Deformation of plastically non-homogeneous materials, Philos. Mag. 21 (1970) 399.

[17]		Gleiter H. Nanocrystalline materials, Prog Mater Sci 33 (1989) 223-315.

[18]		Asaro RJ, Krysl P, Kad B. Deformation mechanism transitions in nanoscale fcc metals, Philos. Mag. Lett. 83 (2003) 733-743.

[19]		Cheng S, Spencer JA, Milligan WW. Strength and tension/compression asymmetry in nanostructured and ultrafine-grain metals, Acta Materialia 51 (2003) 4505-4518.

[20]		Chokshi AH, Rosen A, Karch J, Gleiter H. On the validity of the hall-petch relationship in nanocrystalline materials, Scripta Metallurgica 23 (1989) 1679-1683.

[21]		Schiotz J, Jacobsen KW. A maximum in the strength of nanocrystalline copper, Science 301 (2003) 1357-1359.

[22]		El-Sherik AM, Erb U. Synthesis of bulk nanocrystalline nickel by pulsed electrodeposition, J. of Mater. Sci, 30 (1995) 5743-5749.

[23]		Erb U. Electrodeposited nanocrystals: Synthesis, properties and industrial applications, Nanostructured Mater. 6 (1995) 533-538.

[24]		Schuh CA, Nieh TG, Yamasaki T. Hall–Petch breakdown manifested in abrasive wear resistance of nanocrystalline nickel, Scripta Materialia 46 (2002) 735-740.

[25]		Gertsman VY, Hoffmann M, Gleiter H, Birringer R. The study of grain size dependence of yield stress of copper for a wide grain size range, Acta Metallurgica et Materialia 42 (1994) 3539-3544.

[26]		Yamakov V, Wolf D, Phillpot SR, Mukherjee AK, Gleiter H. Deformation mechanism crossover and mechanical behaviour in nanocrystalline materials, Philos. Mag. Lett. 83 (2003) 385-393.

[27]		Van Swygenhoven H, Derlet PA. Grain-boundary sliding in nanocrystalline fcc metals, Phys. Rev. B 64 (2001).

[28]		Gianola DS, Van Petegem S, Legros M, Brandstetter S, Van Swygenhoven H, Hemker KJ. Stress-assisted discontinuous grain growth and its effect on the deformation behavior of nanocrystalline aluminum thin films, Acta Materialia 54 (2006) 2253-2263.

154

[29]   Cahn JW, Taylor JE. A unified approach to motion of grain boundaries, relative tangential translation along grain boundaries, and grain rotation, Acta Materialia 52 (2004) 4887-4898.

[30]   Shan ZW, Stach EA, Wiezorek JMK, Knapp JA, Follstaedt DM, Mao SX. Grain boundary-mediated plasticity in nanocrystalline nickel, Science 305 (2004) 654-657.

[31]   Budrovic Z, Van Swygenhoven H, Derlet PM, Van Petegem S, Schmitt B. Plastic deformation with reversible peak broadening in nanocrystalline nickel, Science 304 (2004) 273-276.

[32]   Rollett A, Humphreys FJ, Rohrer GS, Hatherly M. Recrystallization and related annealing phenomena, Elsevier Science, 2004.

[33]   Kocks UF. Relation between polycrystal deformation and single-crystal deformation, Metall.l Trans. 1 (1970) 1121-&.

[34]   Sachs G. On the derivation of a condition of flowing, Zeitschrift Des Vereines Deutscher Ingenieure 72 (1928) 734-736.

[35]   Taylor GI. Plastic strain in metals, J. of Inst. of Met. 62 (1938) 307-324.

[36]   Kroner E. On the plastic deformation of polycrystals, Acta Metallurgica 9 (1961) 155-161.

[37]   Lebensohn RA, Tome CN. A self-consistent anisotropic approach for the simulation of plastic-deformation and texture development of polycrystals - application to zirconium alloys, Acta Metallurgica Et Materialia 41 (1993) 2611-2624.

[38]   Dingley DJ. Diffraction from sub-micron areas using electron backscattering in a scanning electron-microscope, Scanning Electron Microsc. (1984) 569-575.

[39]   Schwartz AJ, Kumar M, Adams BL. Electron Backscatter Diffraction in Materials Science, Kluwer Academic, New York, 2000.

[40]   Poulsen HF, Nielsen SF, Lauridsen EM, Schmidt S, Suter RM, Lienert U, Margulies L, Lorentzen T, Juul Jensen D. Three-dimensional maps of grain boundaries and the stress state of individual grains in polycrystals and powders, J. of Appl. Crystallography 34 (2001) 751-756.

[41]   Nishikawa S, Kikuchi S. Diffraction of cathode rays by mica, Nature 121 (1928) 1019-1020.

[42]   Rice KP, Keller RR, Stoykovich MP. Specimen-thickness effects on transmission Kikuchi patterns in the scanning electron microscope, J.l of Microsc. 254 (2014) 129-136.

[43]   Schwartz AJ, Kumar M, Adams BL, Field DP. Electron Backscatter Diffraction in Materials Science, Springer US, 2010.

[44]   Keller RR, Geiss RH. Transmission EBSD from 10 nm domains in a scanning electron microscope, J.l of Microsc. 245 (2012) 245-251.

[45]   Trimby PW. Orientation mapping of nanostructured materials using transmission Kikuchi diffraction in the scanning electron microscope, Ultramicroscopy 120 (2012) 16-24.

[46]   Wright SI, Nowell MM, Field DP. A review of strain analysis using electron backscatter diffraction, Microsc Microanal 17 (2011) 316-329.

[47]   Sun S, Adams BL, King WE. Observations of lattice curvature near the interface of a deformed aluminium bicrystal, Philos. Mag. A 80 (2000) 9-25.

[48]   Wolf U, Ernst F, Muschik T, Finnis MW, Fischmeister HF. The influence of grain boundary inclination on the structure and energy of σ = 3 grain boundaries in copper, Philos. Mag. A 66 (1992) 991-1016.

[49]   Grimmer H, Bollmann W, Warrington DH. Coincidence-Site Lattices And Complete Pattern-Shift Lattices In Cubic-Crystals, Acta Crystallogr A A 30 (1974) 197-207.

[50]   Brandon DG. Structure of High-Angle Grain Boundaries, Acta Metallurgica 14 (1966) 1479-&.

[51]   Palumbo G, Aust KT, Lehockey EM, Erb U, Lin P. On a more restrictive geometric criterion for "special" CSL grain boundaries, Scripta Materialia 38 (1998) 1685-1690.

[52]   Cayron C. Quantification of multiple twinning in face centred cubic materials, Acta Materialia 59 (2011) 252-262.

[53]   Lind J, Li SF, Kumar M. Twin related domains in 3D microstructures of conventionally processed and grain boundary engineered materials, Acta Materialia 114 (2016) 43-53.

[54]   Olmsted DL, Holm EA, Foiles SM. Survey of computed grain boundary properties in face-centered cubic metals-II: Grain boundary mobility, Acta Materialia 57 (2009) 3704-3713.

[55]   Saylor DM, El Dasher BS, Rollett AD, Rohrer GS. Distribution of grain boundaries in aluminum as a function of five macroscopic parameters, Acta Materialia 52 (2004) 3649-3655.

[56]   Palumbo G, Aust KT. Structure-dependence of intergranular corrosion in high-purity nickel, Acta Metallurgica Et Materialia 38 (1990) 2343-2352.

[57]   Palumbo G, King PJ, Aust KT, Erb U, Lichtenberger PC. Grain-boundary design and control for intergranular stress-corrosion resistance, Scr. Metall. Materialia 25 (1991) 1775-1780.

[58]   Bulatov VV, Reed BW, Kumar M. Grain boundary energy function for fcc metals, Acta Materialia 65 (2014) 161-175.

[59]   Lu K, Lu L, Suresh S. Strengthening materials by engineering coherent internal boundaries at the nanoscale, Science 324 (2009) 349-352.

[60]   Form W, Gindraux G, Mlyncar V. Density of annealing twins, Metal Science 14 (1980) 16-20.

[61]   Carpenter HCH, Tamura S. The formation of twinned metallic crystals, Proc. of Royal Soc. of London Series A 113 (1926) 161-U131.

[62]   Gleiter H. Formation of annealing twins, Acta Metallurgica 17 (1969) 1421-&.

[63]   Mahajan S, Pande CS, Imam MA, Rath BB. Formation of annealing twins in f.c.c. crystals, Acta Materialia 45 (1997) 2633-2638.

[64]   Dash S, Brown N. An investigation of the origin and growth of annealing twins, Acta Metallurgica 11 (1963) 1067-1075.

[65]   Burgers WG, Meijs JC, Tiedema TJ. Frequency of Annealing Twins in Copper Crystals Grown By Recrystallization, Acta Metallurgica 1 (1953) 75-&.

[66]   Fullman RL, Fisher JC. Formation of annealing twins during grain growth, J. Appl. Phys. 22 (1951) 1350-1355.

[67]   Meyers MA, Murr LE. Model for formation of annealing twins in fcc metals and alloys, Acta Metallurgica 26 (1978) 951-962.

[68]   Goodhew P. Annealing twin formation by boundary dissociation, Metal Science (1979).

[69]   Warrington D, Boon M. Ordered structures in random grain boundaries; some geometrical probabilities, Acta Metallurgica 23 (1975) 599-607.

[70]   Nielsen JP. The origin of annealing twins, Acta Metallurgica 15 (1967) 1083-1085.

[71]   Christian JW, Mahajan S. Deformation twinning, Prog Mater Sci 39 (1995) 1-157.

[72]   Gottstein G. Annealing texture development by multiple twinning in fcc crystals, Acta Metallurgica 32 (1984) 1117-1138.

[73]   Miura H, Sakai T, Mogawa R, Gottstein G. Nucleation of dynamic recrystallization at grain boundaries in copper bicrystals, Scripta Materialia 51 (2004) 671-675.

[74]   Berger A, Wilbrandt PJ, Haasen P. Development of the recrystallization texture in tensile deformed aluminum single-crystals, Acta Metallurgica 31 (1983) 1433-1443.

[75]   Berger A, Wilbrandt PJ, Ernst F, Klement U, Haasen P. On the generation of new orientations during recrystallization - recent results on the recrystallization of tensile-deformed fcc single-crystals, Prog Mater Sci 32 (1988) 1-95.

[76]   Wilbrandt PJ. On the role of annealing twin formation in the recrystallization texture development, Scr. Metall. Materialia 27 (1992) 1485-1492.

[77]   Watanabe T, Fujii H, Oikawa H, Arai KI. Grain boundaries in rapidly solidified and annealed Fe-6.5 mass% Si polycrystalline ribbons with high ductility, Acta Metallurgica 37 (1989) 941-952.

[78]   Randle V. Sigma-boundary statistics by length and number, Interface Sci 10 (2002) 271-277.

[79]   Rohrer GS, Randle V, Kim CS, Hu Y. Changes in the five-parameter grain boundary character distribution in alpha-brass brought about by iterative thermomechanical processing, Acta Materialia 54 (2006) 4489-4502.

[80]   Randle V. 'Special' boundaries and grain boundary plane engineering, Scripta Materialia 54 (2006) 1011-1015.

[81]   Schuh CA, Kumar M, King WE. Analysis of grain boundary networks and their evolution during grain boundary engineering, Acta Materialia 51 (2003) 687-700.

[82]   Lim LC, Watanabe T. Fracture-Toughness And Brittle-Ductile Transition Controlled By Grain-Boundary Character Distribution (GBCD) In Polycrystals, Acta Metallurgica Et Materialia 38 (1990) 2507-2516.

[83]   Fullwood DT, Niezgoda SR, Adams BL, Kalidindi SR. Microstructure sensitive design for performance optimization, Prog Mater Sci 55 (2010) 477-562.

[84]   Wells DB, Stewart J, Herbert AW, Scott PM, Williams DE. The use of percolation theory to predict the probability of failure of sensitized, austenitic stainless-steels by intergranular stress-corrosion cracking, Corrosion 45 (1989) 649-660.

[85]   Gertsman VY, Janecek M, Tangri K. Grain boundary ensembles in polycrystals, Acta Materialia 44 (1996) 2869-2882.

[86]   Frary M, Schuh CA. Connectivity and percolation behaviour of grain boundary networks in three dimensions, Philos. Mag. 85 (2005) 1123-1143.

[87]   Frary M, Schuh CA. Grain boundary networks: Scaling laws, preferred cluster structure, and their implications for grain boundary engineering, Acta Materialia 53 (2005) 4323-4335.

[88]   Schuh CA, Frary M. Correlations beyond the nearest-neighbor level in grain boundary networks, Scripta Materialia 54 (2006) 1023-1028.

[89]   Kumar M, King WE, Schwartz AJ. Modifications to the microstructural topology in f.c.c. materials through thermomechanical processing, Acta Materialia 48 (2000) 2081-2091.

[90]   Nichols CS, Cook RF, Clarke DR, Smith DA. Alternative length scales for polycrystalline materials - II. Cluster morphology, Acta Metallurgica Et Materialia 39 (1991) 1667-1675.

[91]   Gertsman VY, Henager CH. Grain boundary junctions in microstructure generated by multiple twinning, Interface Sci 11 (2003) 403-415.

[92]   Reed BW, Kumar M. Mathematical methods for analyzing highly-twinned grain boundary networks, Scripta Materialia 54 (2006) 1029-1033.

[93]   Reed BW, Kumar M, Minich RW, Rudd RE. Fracture roughness scaling and its correlation with grain boundary network structure, Acta Materialia 56 (2008) 3278-3289.

[94]   Watanabe T. Grain boundary engineering: historical perspective and future prospects, J. of Mater. Sci, 46 (2011) 4095-4115.

[95]   Randle V. Grain boundary engineering: an overview after 25 years, Mater. Sci. Technol. 26 (2010) 253-261.

[96]   Randle V. Twinning-related grain boundary engineering, Acta Materialia 52 (2004) 4067-4081.

[97]   Randle V, Brown A. Development of grain misorientation texture, in terms of coincident site lattice structures, as a function of thermomechanical treatments, Philos. Mag. A 59 (1989) 1075-1089.

[98]   Lim LC, Raj R. On the distribution of sigma for grain-boundaries in polycrystalline nickel prepared by strain-annealing technique, Acta Metallurgica 32 (1984) 1177-1181.

[99]   Xia S, Zhou BX, Chen WJ. Grain cluster microstructure and grain boundary character distribution in alloy 690, Metall. Mater. Trans. A 40A (2009) 3016-3030.

[100]   Kumar M, Schwartz AJ, King WE. Microstructural evolution during grain boundary engineering of low to medium stacking fault energy fcc materials, Acta Materialia 50 (2002) 2599-2612.

[101]   Meyers MA, Mishra A, Benson DJ. Mechanical properties of nanocrystalline materials, Prog Mater Sci 51 (2006) 427-556.

[102]   Mishnaevsky L, Levashov E, Valiev RZ, Segurado J, Sabirov I, Enikeev N, Prokoshkin S, Solov'yov AV, Korotitskiy A, Gutmanas E, Gotman I, Rabkin E, Psakh'e S, Dluhos L, Seefeldt M, Smolin A. Nanostructured titanium-based materials for medical implants: Modeling and development, Mater. Sci. Eng. R-Rep. 81 (2014) 1-19.

[103]   Prado RA, Benfer J, Facchini D, Mahalanobis N, Gonzalez F. Electrodeposition of nanocrystalline cobalt-phosphorus coatings as a hard chromium alternative for use in DoD acquisition programs, Products Finishing (2012).

[104]   Cordero ZC, Huskins EL, Park M, Livers S, Frary M, Schuster BE, Schuh CA. Powder-Route synthesis and mechanical testing of ultrafine grain tungsten alloys, Metall. Mater. Trans. A 45A (2014) 3609-3618.

[105]   Bridgman PW. On torsion combined with compression, J. Appl. Phys. 14 (1943) 273-283.

[106]   Valiev RZ, Islamgaliev RK, Alexandrov IV. Bulk nanostructured materials from severe plastic deformation, Prog Mater Sci 45 (2000) 103-189.

[107]   Zhilyaev AP, Langdon TG. Using high-pressure torsion for metal processing: Fundamentals and applications, Prog Mater Sci 53 (2008) 893-979.

[108]   Zhang YB, Mishin OV, Kamikawa N, Godfrey A, Liu W, Liu Q. Microstructure and mechanical properties of nickel processed by accumulative roll bonding, Mater. Sci. Eng. A 576 (2013) 160-166.

[109]   Tjong SC, Chen H. Nanocrystalline materials and coatings, Mater. Sci. Eng. R 45 (2004) 1-88.

[110]   Erb U, El-Sherik AM, Palumbo G, Aust KT. Synthesis, structure and properties of electroplated nanocrystalline materials, Nanostructured Mater. 2 (1993) 383-390.

[111]   Robertson A, Erb U, Palumbo G. Practical applications for electrodeposited nanocrystalline materials, Nanostructured Mater. 12 (1999) 1035-1040.

[112]   Rupert TJ, Schuh CA. Sliding wear of nanocrystalline Ni–W: Structural evolution and the apparent breakdown of Archard scaling, Acta Materialia 58 (2010) 4137-4148.

[113]   Padilla HA, Boyce BL. A review of fatigue behavior in nanocrystalline metals, Exp Mech 50 (2010) 5-23.

[114]   Herzer G. Grain-Size dependence of coercivity and permeabilityiIn nanocrystalline ferromagnets, IEEE Trans. Magn. 26 (1990) 1397-1402.

[115]   Palumbo G, Lehockey EM, Lin P. Applications for grain boundary engineered materials, JOM 50 (1998) 40-43.

[116]   Schwartz AJ, King WE, Kumar M. Influence of processing method on the network of grain boundaries, Scripta Materialia 54 (2006) 963-968.

[117]   Valiev RZ, Sergueeva AV, Mukherjee AK. The effect of annealing on tensile deformation behavior of nanostructured SPD titanium, Scripta Materialia 49 (2003) 669-674.

[118]   Dao M, Lu L, Shen YF, Suresh S. Strength, strain-rate sensitivity and ductility of copper with nanoscale twins, Acta Materialia 54 (2006) 5421-5432.

[119]   Lu L, Shen YF, Chen XH, Qian LH, Lu K. Ultrahigh strength and high electrical conductivity in copper, Science 304 (2004) 422-426.

[120]   Barmak K, Darbal A, Ganesh KJ, Ferreira PJ, Rickman JM, Sun T, Yao B, Warren AP, Coffey KR. Surface and grain boundary scattering in nanometric Cu thin films: A quantitative analysis including twin boundaries, J. Vac. Sci. Technol. A 32 (2014) 7.

[121]   Fecht HJ, Hellstern E, Fu Z, Johnson WL. Nanocrystalline metals prepared by high-energy ball milling, Metall. Mater. Trans. A 21 (1990) 2333-2337.

[122]   Bay B, Hansen N, Hughes DA, Kuhlmann-Wilsdorf D. Overview No-96 - Evolution of Fcc deformation structures in polyslip, Acta Metallurgica Et Materialia 40 (1992) 205-219.

[123]   Hansen N, Jensen DJ. Development of microstructure in FCC metals during cold work, Philos. Trans. R 357 (1999) 1447-1469.

[124]   Hughes DA, Hansen N. High angle boundaries formed by grain subdivision mechanisms, Acta Materialia 45 (1997) 3871-3886.

[125]   Qu S, An XH, Yang HJ, Huang CX, Yang G, Zang QS, Wang ZG, Wu SD, Zhang ZF. Microstructural evolution and mechanical properties of Cu–Al alloys subjected to equal channel angular pressing, Acta Materialia 57 (2009) 1586-1601.

[126]   Fecht HJ. Nanostructure formation by mechanical attrition, Nanostructured Mater. 6 (1995) 33-42.

[127]   Eckert J, Holzer JC, Krill CE, Johnson WL. Structural and thermodynamic properties of nanocrystalline FCC metals prepared by mechanical attrition, J Mater Res 7 (1992) 1751-1761.

[128]   Witkin DB, Lavernia EJ. Synthesis and mechanical behavior of nanostructured materials via cryomilling, Prog Mater Sci 51 (2006) 1-60.

[129]   Hellstern E, Fecht HJ, Garland C, Johnson WL. Mechanism of achieving nanocrystalline AlRu by ball milling, Mat. Res. Soc. Symp. Proc. 132 (1989) 137-142.

[130]   Ruan S, Schuh CA. Kinetic Monte Carlo simulations of nanocrystalline film deposition, J. Appl. Phys. 107 (2010) -.

[131]   Mackenzie JK. 2nd Paper on Statistics Associated with the Random Disorientation of Cubes, Biometrika 45 (1958) 229-240.

[132]   Mason JK, Schuh CA. The generalized Mackenzie distribution: Disorientation angle distributions for arbitrary textures, Acta Materialia 57 (2009) 4186-4197.

[133]   Detor AJ, Schuh CA. Tailoring and patterning the grain size of nanocrystalline alloys, Acta Materialia 55 (2007) 371-379.

[134]   Roy I, Yang HW, Dinh L, Lund I, Earthman JC, Mohamed FA. Possible origin of superior corrosion resistance for elecrodeposited nanocrystalline Ni, Scripta Materialia 59 (2008) 305-308.

[135]   Mishin OV, Jensen DJ, Hansen N. Microstructures and boundary populations in materials produced by equal channel angular extrusion, Mater. Sci. Eng. A 342 (2003) 320-328.

[136]   Viladot D, Veron M, Gemmi M, Peiro F, Portillo J, Estrade S, Mendoza J, Llorca-Isern N, Nicolopoulos S. Orientation and phase mapping in the transmission electron microscope using precession-assisted diffraction spot recognition: state-of-the-art results, J.l of Microsc. 252 (2013) 23-34.

[137]   Nix WD, Gao HJ. Indentation size effects in crystalline materials: A law for strain gradient plasticity, J. Mech. Phys. Solids 46 (1998) 411-425.

[138]   Schuh CA, Kumar M, King WE. Universal features of grain boundary networks in FCC materials, J. of Mater. Sci, 40 (2005) 847-852.

[139]   Xun Y, Mohamed FA. Refining efficiency and capability of top-down synthesis of nanocrystalline materials, Mater. Sci. Eng. A 528 (2011) 5446-5452.

[140]   Zhilyaev AP, Kim BK, Nurislamova GV, Baro MD, Szpunar JA, Langdon TG. Orientation imaging microscopy of ultrafine-grained nickel, Scripta Materialia 46 (2002) 575-580.

[141]   Raju KS, Krishna MG, Padmanabhan KA, Muraleedharan K, Gurao NP, Wilde G. Grain size and grain boundary character distribution in ultra-fine grained (ECAP) nickel, Mater. Sci. Eng. A 491 (2008) 1-7.

[142]   Hughes DA, Hansen N. Graded nanostructures produced by sliding and exhibiting universal behavior, Phys. Rev. Lett. 87 (2001) 4.

[143]   Grewer M, Braun C, Lohmiller J, Gruber PA, Honkimäki V, Birringer R. Dislocation scarcity makes room for grain-boundary mediated deformation in nanocrystalline PdAu alloys, ArXiv (2014).

158

[144]   Xun YW, Lavernia EJ, Mohamed FA. Synthesis of nanocrystalline Zn-22 pct Al using cryomilling, Metall. Mater. Trans. A 35A (2004) 573-581.

[145]   Suryanarayana C. Mechanical alloying and milling, Prog Mater Sci 46 (2001) 1-184.

[146]   Rupert TJ, Trenkle JC, Schuh CA. Enhanced solid solution effects on the strength of nanocrystalline alloys, Acta Materialia 59 (2011) 1619-1631.

[147]   Knapp JA, Follstaedt DM. Hall-Petch relationship in pulsed-laser deposited nickel films, J Mater Res 19 (2004) 218-227.

[148]   Hughes GD, Smith SD, Pande CS, Johnson HR, Armstrong RW. Hall-petch strengthening for the microhardness of twelve nanometer grain diameter electrodeposited nickel, Scripta Metallurgica 20 (1986) 93-97.

[149]   El-Sherik AM, Erb U, Palumbo G, Aust KT. Deviations from hall-petch behaviour in as-prepared nanocrystalline nickel, Scr. Metall. Materialia 27 (1992) 1185-1188.

[150]   Abson DJ, Jonas JJ. The Hall–Petch relation and high-temperature subgrains, Metal Science 4 (1970) 24-28.

[151]   Kobayashi S, Yoshimura T, Tsurekawa S, Watanabe T, Cui JZ. Grain boundary microstructure-controlled superplasticity in Al-Li-Cu-Mg-Zr alloy, Mater. Trans. 44 (2003) 1469-1479.

[152]   Hasnaoui A, Van Swygenhoven H, Derlet PM. Dimples on nanocrystalline fracture surfaces as evidence for shear plane formation, Science 300 (2003) 1550-1552.

[153]   Zhou XW, Wadley HNG. Twin formation during the atomic deposition of copper, Acta Materialia 47 (1999) 1063-1078.

[154]   Zhang X, Anderoglu O, Hoagland RG, Misra A. Nanoscale growth twins in sputtered metal films, JOM 60 (2008) 75-78.

[155]   Siegel DJ. Generalized stacking fault energies, ductilities, and twinnabilities of Ni and selected Ni alloys, Appl. Phys. Lett. 87 (2005) 121901.

[156]   LaGrange T, Reed BW, Wall M, Mason J, Barbee T, Kumar M. Topological view of the thermal stability of nanotwinned copper, Appl. Phys. Lett. 102 (2013).

[157]   Horita Z, Smith DJ, Nemoto M, Valiev RZ, Langdon TG. Observations of grain boundary structure in submicrometer-grained Cu and Ni using high-resolution electron microscopy, J Mater Res 13 (1998) 446-450.

[158]   Pantleon K, Somers MAJ. Interpretation of microstructure evolution during self-annealing and thermal annealing of nanocrystalline electrodeposits—A comparative study, Mater. Sci. Eng. A 528 (2010) 65-71.

[159]   Liu X, Nuhfer NT, Warren AP, Coffey KR, Rohrer GS, Barmak K. Grain size dependence of the twin length fraction in nanocrystalline Cu thin films via transmission electron microscopy based orientation mapping, J Mater Res (2015) 1-10.

[160]   Schuh CA, Minich RW, Kumar M. Connectivity and percolation in simulated grain-boundary networks, Philos. Mag. 83 (2003) 711-726.

[161]   Kim SH, Aust KT, Gonzalez F, Palumbo G. The corrosion behavior of nanocrystalline electrodeposits, Plat. Surf. Finish. 91 (2004) 68-70.

[162]   Zhao Y, Cheng IC, Kassner ME, Hodge AM. The effect of nanotwins on the corrosion behavior of copper, Acta Materialia 67 (2014) 181-188.

[163]   Zhao H, Liu L, Zhu J, Tang Y, Hu W. Microstructure and corrosion behavior of electrodeposited nickel prepared from a sulphamate bath, Mater. Lett. 61 (2007) 1605-1608.

[164]   Vijayakumar J, Mohan S. Comparative study of microstructure and corrosion properties in 3.5% NaCl solution of electrodeposited nickel obtained from various baths, Surf. Eng. 27 (2011) 32-36.

[165]   Qin LY, Lian JS, Jiang Q. Effect of grain size on corrosion behavior of electrodeposited bulk nanocrystalline Ni, Trans. Nonferrous Met. Soc. China 20 (2010) 82-89.

[166]   Mishra R, Balasubramaniam R. Effect of nanocrystalline grain size on the electrochemical and corrosion behavior of nickel, Corrosion Sci. 46 (2004) 3019-3029.

[167]   Wen C, Wen G, Qian Y, Xinxin Q. Study on the corrosion properties of nanocrystalline nickel electrodepositied by reverse pulse current, Appl. Surf. Sci. 276 (2013) 604-608.

[168]   Janecek M, Hadzima B, Hellmig RJ, Estrin Y. The influence of microstructure on the corrosion properties of Cu polycrystals prepared by ECAP, Kov. Mater.-Met. Mater. 43 (2005) 258-271.

[169]   Hadzima B, Janecek M, Hellmig RJ, Kutnyakova Y, Estrin Y. Microstructure and corrosion behaviour of ultrafine-grained copper. in: Horita Z, (Ed.). Nanomaterials by Severe Plastic Deformation, vol. 503-504. Trans Tech Publications Ltd, Zurich-Uetikon, 2006. pp. 883-888.

[170]   Saremi M, Abouie M. Oxidation and corrosion resistance of nanocrystalline copper deposit produced by pulse electrodeposition. in: Hashmi MSJ, Mridha S, Naher S, (Eds.). Advances in Materials and Processing Technologies Ii, Pts 1 and 2, vol. 264-265. Trans Tech Publications Ltd, Stafa-Zurich, 2011. pp. 1519-1525.

[171]   Saremi M, Yeganeh M. Investigation of corrosion behaviour of nanostructured copper thin film produced by radio frequency sputtering, Micro Nano Lett. 5 (2010) 70-75.

[172]   Xu XX, Nie FL, Zhang JX, Zheng W, Zheng YF, Hu C, Yang G. Corrosion and ion release behavior of ultra-fine grained bulk pure copper fabricated by ECAP in Hanks solution as potential biomaterial for contraception, Mater. Lett. 64 (2010) 524-527.

[173]   Palumbo G, Erb U. Enhancing the operating life and performance of lead-acid batteries via grain-boundary engineering, MRS Bull. 24 (1999) 27-32.

[174]   Vinogradov A, Mimaki T, Hashimoto S, Valiev R. On the corrosion behaviour of ultra-fine grain copper, Scripta Materialia 41 (1999) 319-326.

[175]   Schuh CA, Anderson K, Orme C. Rapid assessment of anisotropic surface processes: experiments on the corrosion of Inconel 600, Surf. Sci. 544 (2003) 183-192.

[176]   Kollia C, Spyrellis N. Textural modifications in nickel electrodeposition under pulse reversed current, Surf. Coat. Technol. 57 (1993) 71-75.

[177]   Lü AQ, Zhang Y, Li Y, Liu G, Zang QH, Liu CM. Effect of nanocrystalline and twin boundaries on corrosion behavior Oo 316l stainless steel using SMAT, Acta Metallurgica Sinica 19 (2006) 183-189.

[178]   Watanabe T. An approach to grain-boundary design for strong and ductile polycrystals, Res Mechanica 11 (1984) 47-84.

[179]   Lin P, Palumbo G, Erb U, Aust KT. Influence of grain boundary character distribution on sensitization and intergranular corrosion of alloy 600, Scr. Metall. Materialia 33 (1995) 1387-1392.

[180]   Jin Y, Lin B, Rollett AD, Rohrer GS, Bernacki M, Bozzolo N. Thermo-mechanical factors influencing annealing twin development in nickel during recrystallization, J. of Mater. Sci, 50 (2015) 5191-5203.

[181]   Blobaum KJM, Stolken JS, Kumar M. Grain boundary engineering of copper shaped-charge. in: Schuh CA, Kumar M, Carter CB, Randle V, (Eds.). Interfacial Engineering for Optimized Properties Iii, vol. 819. Materials Research Society, Warrendale, 2004. pp. 51-56.

[182]   Bechtle S, Kumar M, Somerday BP, Launey ME, Ritchie RO. Grain-boundary engineering markedly reduces susceptibility to intergranular hydrogen embrittlement in metallic materials, Acta Materialia 57 (2009) 4148-4157.

[183]   Warrington DH, Boon M. Ordered structures in random grain boundaries - some geometrical probabilities, Acta Metallurgica 23 (1975) 599-607.

[184]   Cahoon JR, Li Q, Richards NL. Microstructural and processing factors influencing the formation of annealing twins, Mater. Sci. Eng. A 526 (2009) 56-61.

[185]   Eden M. A Two-dimensional Growth Process. Proc. Fourth Berkeley Symp. on Math. Stat. and Probab., vol. 4. Berkeley, Calif.: University of California Press, 1961. p.223-239.

[186]   Lereah Y, Zarudi I, Grunbaum E, Deutscher G, Buldyrev SV, Stanley HE. Morphology of Ge-Al thin-films - experiments and model, Phys. Rev. E 49 (1994) 649-656.

[187]   Basinger JA, Homer ER, Fullwood DT, Adams BL. Two-dimensional grain boundary percolation in alloy 304 stainless steel, Scripta Materialia 53 (2005) 959-963.

[188]   Lee SL, Richards NL. The effect of single-step low strain and annealing of nickel on grain boundary character, Mater. Sci. Eng. A 390 (2005) 81-87.

[189]   Guyot BM, Richards NL. A study on the effect of cold rolling and annealing on special grain boundary fractions in commercial-purity nickel, Mater. Sci. Eng. A 395 (2005) 87-97.

[190]   Shimada M, Kokawa H, Wang ZJ, Sato YS, Karibe I. Optimization of grain boundary character distribution for intergranular corrosion resistant 304 stainless steel by twin-induced grain boundary engineering, Acta Materialia 50 (2002) 2331-2341.

[191]   Thomson CB, Randle V. A study of twinning in nickel, Scripta Materialia 35 (1996) 385-390.

[192]   Thaveeprungsriporn V, Was GS. The role of coincidence-site-lattice boundaries in creep of Ni-16Cr-9Fe at 360 degrees C, Metall. Mater. Trans. A 28 (1997) 2101-2112.

[193]   Bertz SH. Branching in graphs and molecules, Discrete Appl. Math. 19 (1988) 65-83.

[194]   Simoes S, Calinas R, Vieira MT, Vieira MF, Ferreira PJ. In situ TEM study of grain growth in nanocrystalline copper thin films, Nanotechnology 21 (2010) 145701.

[195]   Panzarino JF, Ramos JJ, Rupert TJ. Quantitative tracking of grain structure evolution in a nanocrystalline metal during cyclic loading, Modelling Simul. Mater. Sci. Eng. 23 (2015) 025005.

[196]   Bober DB, Kumar M, Rupert TJ. Nanocrystalline grain boundary engineering: Increasing $\Sigma 3$ boundary fraction in pure Ni with thermomechanical treatments, Acta Materialia 86 (2015) 43-54.

[197]   Hall EO. The Deformation And Ageing Of Mild Steel, Proc. of Phys. Soc. London Section B 64 (1951) 747-753.

[198]   Li JCM. Petch relation and grain boundary sources, Trans. of Metall. Soc. of AIME 227 (1963) 239.

[199]   Kuhlmann-Wilsdorf D, Wilsdorf H. The surface structures of deformed aluminium, copper, silver, and alpha-brass, and their theoretical interpretation, Acta Metallurgica 1 (1953) 394.

[200]   Lim LC. Slip-twin interactions in nickel at 573K at large strains, Scripta Metallurgica 18 (1984) 1139-1142.

[201]   Kashihara K, Inoko F. Effect of piled-up dislocations on strain induced boundary migration (SIBM) in deformed aluminum bicrystals with originally Sigma 3 twin boundary, Acta Materialia 49 (2001) 3051-3061.

[202]   Lim LC, Raj R. Slip-Twin Interactions In Bicrystals Of Nickel At 573K At Large Strain, Scripta Metallurgica 20 (1986) 539-544.

[203]   Miura S, Saeki Y. Plastic-Deformation Of Copper-Crystals Containing A Twin Band, Trans. of Japan Inst. of Met. 17 (1976) 253-260.

[204]   Mahajan S, Chin GY. Twin-Slip, twin-twin and slip-twin interactions in Co-8 wt percent Fe alloy single-crystals, Acta Metallurgica 21 (1973) 173-179.

[205]   Shen Z, Wagoner RH, Clark WAT. Dislocation and grain-boundary interactions in metals, Acta Metallurgica 36 (1988) 3231-3242.

[206]   Pang JWL, Liu W, Budai JD, Ice GE. Inhomogeneous deformation behavior in intercrystalline regions in polycrystalline Ni, Acta Materialia 65 (2014) 393-399.

[207]   Babyak WJ, Rhines FN. The relationshipbBetween the boundary area and hardness of recrystallized cartridge brass, Trans. of American Inst. of Mining Metall.l Eng. 218 (1960) 21-23.

[208]   Kral MV, Drabble DJF, Gardiner BR, Tait PC. Implications of EBSD-based Grain Size Measurement on Structure-Property Correlations, Prakt. Metallogr.-Pract. Metallogr. 46 (2009) 469-482.

[209]   Gu P, Dao M, Asaro RJ, Suresh S. A unified mechanistic model for size-dependent deformation in nanocrystalline and nanotwinned metals, Acta Materialia 59 (2011) 6861-6868.

[210]   Pande CS, Rath BB, Imam MA. Effect of annealing twins on Hall–Petch relation in polycrystalline materials, Mater. Sci. Eng. A 367 (2004) 171-175.

[211]   Lee TC, Robertson IM, Birnbaum HK. Prediction of slip transfer mechanisms across grain-boundaries, Scripta Metallurgica 23 (1989) 799-803.

[212]   Evans JT. Heterogeneous shear of a twin boundary in alpha-brass, Scripta Metallurgica 8 (1974) 1099-1103.

[213]   Suzuki H, Nakanishi K. Theory of grain-size dependence of yield stress in face-centered cubic alloys, Trans. of Japan Inst. of Met. 16 (1975) 17-27.

[214]   Konopka K, Mizera J, Wyrzykowski JW. The generation of dislocations from twin boundaries and its effect upon the flow stresses in FCC metals, J. Mater. Process. Technol. 99 (2000) 255-259.

[215]   Coleman M, Randle V. Changes in interface parameters and tensile properties in copper as a consequence of iterative processing, Metall. Mater. Trans. A 39A (2008) 2175-2183.

[216]   Miura S, Ono N, Nishimura Y. Hall-Petch Relation and Twin Boundaries in Pure Copper and Cu-Al Alloys, J. Soc. Mater. Sci. Jpn. 58 (2009) 865-872.

[217]   Bober DB, Lind J, Mulay RP, Rupert TJ, Kumar M. The Formation and Characterization of Large Twin Related Domains, Submitted (2016).

[218]   Miyazaki S, Shibata K, Fujita H. Effect of specimen thickness on mechanical-properties of polycrystalline aggregates with various grain sizes, Acta Metallurgica 27 (1979) 855-862.

[219]   Kocks UF, Mecking H. Physics and phenomenology of strain hardening: the FCC case, Prog Mater Sci 48 (2003) 171-273.

[220]   Hansen N. Hall–Petch relation and boundary strengthening, Scripta Materialia 51 (2004) 801-806.

[221]   Morey RD, Rouder JN. BayesFactor: computation of Bayes factors for common designs. 2015.

[222]   R_Core_Team. R: a language and environment for statistical computing. 2016.

[223]   Jeffreys H. The Theory of Probability, Oxford University Press, 1961.

[224]   Kurzydlowski KJ, Bucki JJ. Flow-stress dependence on the distribution of grain-size in polycrystals, Acta Metallurgica Et Materialia 41 (1993) 3141-3146.

[225]   Dunstan DJ, Bushby AJ. Grain size dependence of the strength of metals: The Hall-Petch effect does not scale as the inverse square root of grain size, Int. J. Plast. 53 (2014) 56-65.

[226]   Hirth JP. The influence of grain boundaries on mechanical properties, Metall.l Trans. 3 (1972) 3047-3067.

[227]   de Koning M, Miller R, Bulatov VV, Abraham FF. Modelling grain-boundary resistance in intergranular dislocation slip transmission, Philos. Mag. A 82 (2002) 2511-2527.

[228]   Murr LE, Hecker SS. Quantitative evidence for dislocation emission from grain-boundaries, Scripta Metallurgica 13 (1979) 167-171.

[229]   Kumar KS, Van Swygenhoven H, Suresh S. Mechanical behavior of nanocrystalline metals and alloys, Acta Materialia 51 (2003) 5743-5774.

[230]   Jeong DH, Gonzalez F, Palumbo G, Aust KT, Erb U. The effect of grain size on the wear properties of electrodeposited nanocrystalline nickel coatings, Scripta Materialia 44 (2001) 493-499.

[231]   Rupert TJ, Schuh CA. Mechanically driven grain boundary relaxation: a mechanism for cyclic hardening in nanocrystalline Ni, Philos. Mag. Lett. 92 (2012) 20-28.

[232]   Rupert TJ. Strain localization in a nanocrystalline metal: Atomic mechanisms and the effect of testing conditions, J. Appl. Phys. 114 (2013).

[233]   Rupert TJ, Trelewicz JR, Schuh CA. Grain boundary relaxation strengthening of nanocrystalline Ni-W alloys, J Mater Res 27 (2012) 1285-1294.

[234]   Khalajhedayati A, Rupert TJ. Emergence of localized plasticity and failure through shear banding during microcompression of a nanocrystalline alloy, Acta Materialia 65 (2014) 326-337.

[235]   Thomson CB, Randle V. "Fine tuning" at Sigma 3(n) boundaries in nickel, Acta Materialia 45 (1997) 4909-4916.

[236]   King WE, Schwartz AJ. Toward optimization of the grain boundary character distribution in OFE copper, Scripta Materialia 38 (1998) 449-455.

[237]   Palumbo G. U. S. Patent No. 5702543 (1997) and 5817193 (1998).

[238]   Legros M, Elliott BR, Rittner MN, Weertman JR, Hemker KJ. Microsample tensile testing of nanocrystalline metals, Philos. Mag. A 80 (2000) 1017-1026.

[239]   Bitzek E, Derlet PM, Anderson PM, Van Swygenhoven H. The stress-strain response of nanocrystalline metals: A statistical analysis of atomistic simulations, Acta Materialia 56 (2008) 4846-4857.

[240]   Li L, Anderson PM, Lee MG, Bitzek E, Derlet P, Van Swygenhoven H. The stress-strain response of nanocrystalline metals: A quantized crystal plasticity approach, Acta Materialia 57 (2009) 812-822.

[241]   Ke M, Hackney SA, Milligan WW, Aifantis EC. Observation and Measurement of Grain Rotation and Plastic Strain in Nanostructured Metal Thin-Films, Nanostructured Mater. 5 (1995) 689-697.

[242]   Kobler A, Kashiwar A, Hahn H, Kubel C. Combination of in situ straining and ACOM TEM: A novel method for analysis of plastic deformation of nanocrystalline metals, Ultramicroscopy 128 (2013) 68-81.

[243]   Velasco M, Van Swygenhoven H, Brandl C. Coupled grain boundary motion in a nanocrystalline grain boundary network, Scripta Materialia 65 (2011) 151-154.

[244]   Lund AC, Nieh TG, Schuh CA. Tension/compression strength asymmetry in a simulated nanocrystalline metal, Phys. Rev. B 69 (2004).

[245]   Zhang K, Weertman JR, Eastman JA. Rapid stress-driven grain coarsening in nanocrystalline Cu at ambient and cryogenic temperatures, Appl. Phys. Lett. 87 (2005).

[246]   Rupert TJ, Gianola DS, Gan Y, Hemker KJ. Experimental observations of stress-driven grain boundary migration, Science 326 (2009) 1686-1690.

[247]   Vlassak JJ, Nix WD. A new bulge test technique for the determination of young modulus and poisson ratio of thin-films, J Mater Res 7 (1992) 3242-3249.

[248]   Beams JW, Walker WE, Morton HS. Mechanical properties of thin films of silver, Phys Rev 87 (1952) 524-525.

[249]   Kalkman AJ, Verbruggen AH, Janssen GCAM. High-temperature bulge-test setup for mechanical testing of free-standing thin films, Rev Sci Instrum 74 (2003) 1383-1385.

[250]   Xiang Y, Chen X, Vlassak JJ. Plane-strain bulge test for thin films, J Mater Res 20 (2005) 2360-2370.

[251]   Small MK, Nix WD. Analysis of the accuracy of the bulge test in determining the mechanical-properties of thin-films, J Mater Res 7 (1992) 1553-1563.

[252]   Trimby PW, Cao Y, Chen ZB, Han S, Hemker KJ, Lian JS, Liao XZ, Rottmann P, Samudrala S, Sun JL, Wang JT, Wheeler J, Cairney JM. Characterizing deformed ultrafine-grained and nanocrystalline materials using transmission Kikuchi diffraction in a scanning electron microscope, Acta Materialia 62 (2014) 69-80.

[253]   Randle V. Microtexture determination and its applications. 2nd ed., Maney for the Institute of Materials, Minerals and Mining, London, 2003.

[254]   ASTM E2627 Standard Practice for Determining Average Grain Size Using Electron Backscatter Diffraction (EBSD) in Fully Recrystallized Polycrystalline Materials. West Conshohocken, PA: ASTM International, 2013.

[255]   Vo NQ, Averback RS, Bellon P, Odunuga S, Caro A. Quantitative description of plastic deformation in nanocrystalline Cu: Dislocation glide versus grain boundary sliding, Phys. Rev. B 77 (2008).

[256]   Gianola DS, Farkas D, Gamarra M, He MR. The role of confinement on stress-driven grain boundary motion in nanocrystalline aluminum thin films, J. Appl. Phys. 112 (2012).

[257]   Mitra R, Hoffman RA, Madan A, Weertman JR. Effect of process variables on the structure, residual stress, and hardness of sputtered nanocrystalline nickel films, J Mater Res 16 (2001) 1010-1027.

[258]   Priyadarshini BG, Aich S, Chakraborty M. Structural and morphological investigations on DC-magnetron-sputtered nickel films deposited on Si (100), J. of Mater. Sci, 46 (2011) 2860-2873.

[259]   Tan L, Allen TR, Busby JT. Grain boundary engineering for structure materials of nuclear reactors, J Nucl Mater 441 (2013) 661-666.

[260]   Hanlon T, Chokshi AH, Manoharan M, Suresh S. Effects of grain refinement and strength on friction and damage evolution under repeated sliding contact in nanostructured metals, Int J Fatigue 27 (2005) 1159-1163.

[261]   Liao XZ, Kilmametov AR, Valiev RZ, Gao HS, Li XD, Mukherjee AK, Bingert JF, Zhu YT. High-pressure torsion-induced grain growth in electrodeposited nanocrystalline Ni, Appl. Phys. Lett. 88 (2006).

[262]   Schwaiger R. Deformation of nanostructured materials: insights from experimental observations, Int. Soc. for Optics and Photonics Newsroom (2006) 1-2.

[263]   Pan D, Nieh TG, Chen MW. Strengthening and softening of nanocrystalline nickel during multistep nanoindentation, Appl. Phys. Lett. 88 (2006).

[264]   Brandstetter S, Zhang K, Escuadro A, Weertman JR, Van Swygenhoven H. Grain coarsening during compression of bulk nanocrystalline nickel and copper, Scripta Materialia 58 (2008) 61-64.

[265]   Wang YB, Li BQ, Sui ML, Mao SX. Deformation-induced grain rotation and growth in nanocrystalline Ni, Appl. Phys. Lett. 92 (2008).

[266]   Kulovits A, Mao SX, Wiezorek JMK. Microstructural changes of nanocrystalline nickel during cold rolling, Acta Materialia 56 (2008) 4836-4845.

[267]   Gurao NP, Suwas S. Deformation mechanisms during large strain deformation of nanocrystalline nickel, Appl. Phys. Lett. 94 (2009).

[268]   Cahn JW, Mishin Y, Suzuki A. Coupling grain boundary motion to shear deformation, Acta Materialia 54 (2006) 4953-4975.

[269]   Moldovan D, Wolf D, Phillpot SR. Theory of diffusion-accommodated grain rotation in columnar polycrystalline microstructures, Acta Materialia 49 (2001) 3521-3532.

[270]   Raj R, Ashby MF. Grain boundary sliding and diffusional creep, Metall.l Trans. 2 (1971) 1113-&.

[271]   Harris KE, Singh VV, King AH. Grain rotation in thin films of gold, Acta Materialia 46 (1998) 2623-2633.

[272]   Ashby MF, Verrall RA. Diffusion-Accommodated flow and superplasticity, Acta Metallurgica 21 (1973) 149-163.

[273]   Wang B, Alam MT, Haque MA. Grain growth in nanocrystalline nickel films at low temperature and stress, Scripta Materialia 71 (2014) 1-4.

[274]   Prasad MJNV, Chokshi AH. Deformation-induced thermally activated grain growth in nanocrystalline nickel, Scripta Materialia 67 (2012) 133-136.

[275]   Hibbard GD, Radmilovic V, Aust KT, Erb U. Grain boundary migration during abnormal grain growth in nanocrystalline Ni, Mater. Sci. Eng. A 494 (2008) 232-238.

[276]   Klement U, Erb U, ElSherik AM, Aust KT. Thermal stability of nanocrystalline Ni, Mater. Sci. Eng. A 203 (1995) 177-186.

[277]   Legros M, Gianola DS, Hemker KJ. In situ TEM observations of fast grain-boundary motion in stressed nanocrystalline aluminum films, Acta Materialia 56 (2008) 3380-3393.

[278]   Haslam AJ, Phillpot SR, Wolf H, Moldovan D, Gleiter H. Mechanisms of grain growth in nanocrystalline fcc metals by molecular-dynamics simulation, Mater. Sci. Eng. A 318 (2001) 293-312.

[279]   Brons JG, Thompson GB. A comparison of grain boundary evolution during grain growth in fcc metals, Acta Materialia 61 (2013) 3936-3944.

[280]   Kobler A, Lohmiller J, Schafer J, Kerber M, Castrup A, Kashiwar A, Gruber PA, Albe K, Hahn H, Kubel C. Deformation-induced grain growth and twinning in nanocrystalline palladium thin films, Beilstein J. of Nanotechnol. 4 (2013) 554-566.

[281]   Liao XZ, Zhou F, Lavernia EJ, He DW, Zhu YT. Deformation twins in nanocrystalline Al, Appl. Phys. Lett. 83 (2003) 5062-5064.

[282]   Li BQ, Sui ML, Li B, Ma E, Mao SX. Reversible twinning in pure aluminum, Phys. Rev. Lett. 102 (2009).

[283]   Luo XM, Zhu XF, Zhang GP. Nanotwin-assisted grain growth in nanocrystalline gold films under cyclic loading, Nat Commun 5 (2014).

[284]   Randle V. The role of the coincident site lattice in grain boundary engineering, The Institute of Materials, London, 1996.

[285]   Saylor DM, El-Dasher BS, Adams BL, Rohrer GS. Measuring the five-parameter grain-boundary distribution from observations of planar sections, Metall. Mater. Trans. A 35A (2004) 1981-1989.

163

[286]	Liu HH, Schmidt S, Poulsen HF, Godfrey A, Liu ZQ, Sharon JA, Huang X. Three-dimensional orientation mapping in the transmission electron microscope, Science 332 (2011) 833-834.

[287]	Goto M, Kamil K, Han SZ, Euh K, Kim SS, Lee J. Fatigue-induced grain coarsening and crack growth behavior in ultrafine-grained copper under different loading histories, Int J Fatigue 51 (2013) 57-67.

[288]	Choi IC, Kim YJ, Seok MY, Yoo BG, Kim JY, Wang YM, Jang JI. Nanoscale room temperature creep of nanocrystalline nickel pillars at low stresses, Int. J. Plast. 41 (2013) 53-64.

[289]	Van Swygenhoven H, Derlet PM, Froseth AG. Nucleation and propagation of dislocations in nanocrystalline fcc metals, Acta Materialia 54 (2006) 1975-1983.

[290]	Watanabe T, Tsurekawa S. Toughening of brittle materials by grain boundary engineering, Mater. Sci. Eng. A 387–389 (2004) 447-455.

[291]	Kobayashi S, Tsurekawa S, Watanabe T. A new approach to grain boundary engineering for nanocrystalline materials, Beilstein J. of Nanotechnol. 7 (2016) 1829-1849.

[292]	Ma H, La Mattina F, Shorubalko I, Spolenak R, Seita M. Engineering the grain boundary network of thin films via ion-irradiation: Towards improved electromigration resistance, Acta Materialia 123 (2017) 272-284.

[293]	Shute CJ, Myers BD, Xie S, Li SY, Barbee TW, Hodge AM, Weertman JR. Detwinning, damage and crack initiation during cyclic loading of Cu samples containing aligned nanotwins, Acta Materialia 59 (2011) 4569-4577.

[294]	Lu N, Wang X, Suo Z, Vlassak J. Metal films on polymer substrates stretched beyond 50%, Appl. Phys. Lett. 91 (2007) 221909.

[295]	Li T, Huang ZY, Xi ZC, Lacour SP, Wagner S, Suo Z. Delocalizing strain in a thin metal film on a polymer substrate, Mech. of Mater. 37 (2005) 261-273.

[296]	Lin B. Investigating annealing twin formation mechanisms in face-centered cubic nickel. Carnegie Mellon University, 2015.

[297]	An XH, Lin QY, Wu SD, Zhang ZF. Mechanically driven annealing twinning induced by cyclic deformation in nanocrystalline Cu, Scripta Materialia 68 (2013) 988-991.

[298]	Winning M, Gottstein G, Shvindlerman LS. Stress induced grain boundary motion, Acta Materialia 49 (2001) 211-219.

[299]	Gorkaya T, Molodov DA, Gottstein G. Stress-driven migration of symmetrical < 1 0 0 > tilt grain boundaries in Al bicrystals, Acta Materialia 57 (2009) 5396-5405.

[300]	Furnish TA, Mehta A, Van Campen D, Bufford DC, Hattar K, Boyce BL. The onset and evolution of fatigue-induced abnormal grain growth in nanocrystalline Ni-Fe, J. of Mater. Sci, 52 (2017) 46-59.

[301]	Bitzek E, Derlet PM, Anderson PM, Van Swygenhoven H. The stress–strain response of nanocrystalline metals: a statistical analysis of atomistic simulations, Acta Materialia 56 (2008) 4846-4857.

[302]	Frøseth AG, Van Swygenhoven H, Derlet PM. Developing realistic grain boundary networks for use in molecular dynamics simulations, Acta Materialia 53 (2005) 4847-4856.

[303]	Gindraux G, Form W. New concepts of annealing-twin formation in face-centered cubic metals, J. of Inst. of Met. 101 (1973) 85-93.

[304]	Derlet PM, Van Swygenhoven† H, Hasnaoui A. Atomistic simulation of dislocation emission in nanosized grain boundaries, Philos. Mag. 83 (2003) 3569-3575.

[305]	Liao X, Zhao Y, Srinivasan S, Zhu Y, Valiev R, Gunderov D. Deformation twinning in nanocrystalline copper at room temperature and low strain rate, Appl. Phys. Lett. 84 (2004) 592-594.

[306]	Chen M, Ma E, Hemker KJ, Sheng H, Wang Y, Cheng X. Deformation twinning in nanocrystalline aluminum, Science 300 (2003) 1275-1277.

[307]	Frøseth AG, Derlet PM, Van Swygenhoven H. Twinning in nanocrystalline FCC metals, Adv. Eng. Mater. 7 (2005) 16-20.

[308]	Zhu YT, Wu XL, Liao XZ, Narayan J, Mathaudhu SN, Kecskés LJ. Twinning partial multiplication at grain boundary in nanocrystalline fcc metals, Appl. Phys. Lett. 95 (2009) 031909.

[309]	Zhu YT, Liao XZ, Wu XL. Deformation twinning in nanocrystalline materials, Prog Mater Sci 57 (2012) 1-62.

[310]	Moldovan D, Wolf D, Phillpot S, Haslam A. Role of grain rotation during grain growth in a columnar microstructure by mesoscale simulation, Acta Materialia 50 (2002) 3397-3414.

[311]	Hasnaoui A, Van Swygenhoven H, Derlet P. Cooperative processes during plastic deformation in nanocrystalline fcc metals: A molecular dynamics simulation, Phys. Rev. B 66 (2002) 184112.

[312]	Wang L, Teng J, Liu P, Hirata A, Ma E, Zhang Z, Chen M, Han X. Grain rotation mediated by grain boundary dislocations in nanocrystalline platinum, Nat Commun 5 (2014).

[313]	Kobler A, Kashiwar A, Hahn H, Kübel C. Combination of in situ straining and ACOM TEM: A novel method for analysis of plastic deformation of nanocrystalline metals, Ultramicroscopy 128 (2013) 68-81.

[314]   Panzarino JF, Pan Z, Rupert TJ. Plasticity-induced restructuring of a nanocrystalline grain boundary network, Acta Materialia 120 (2016) 1-13.